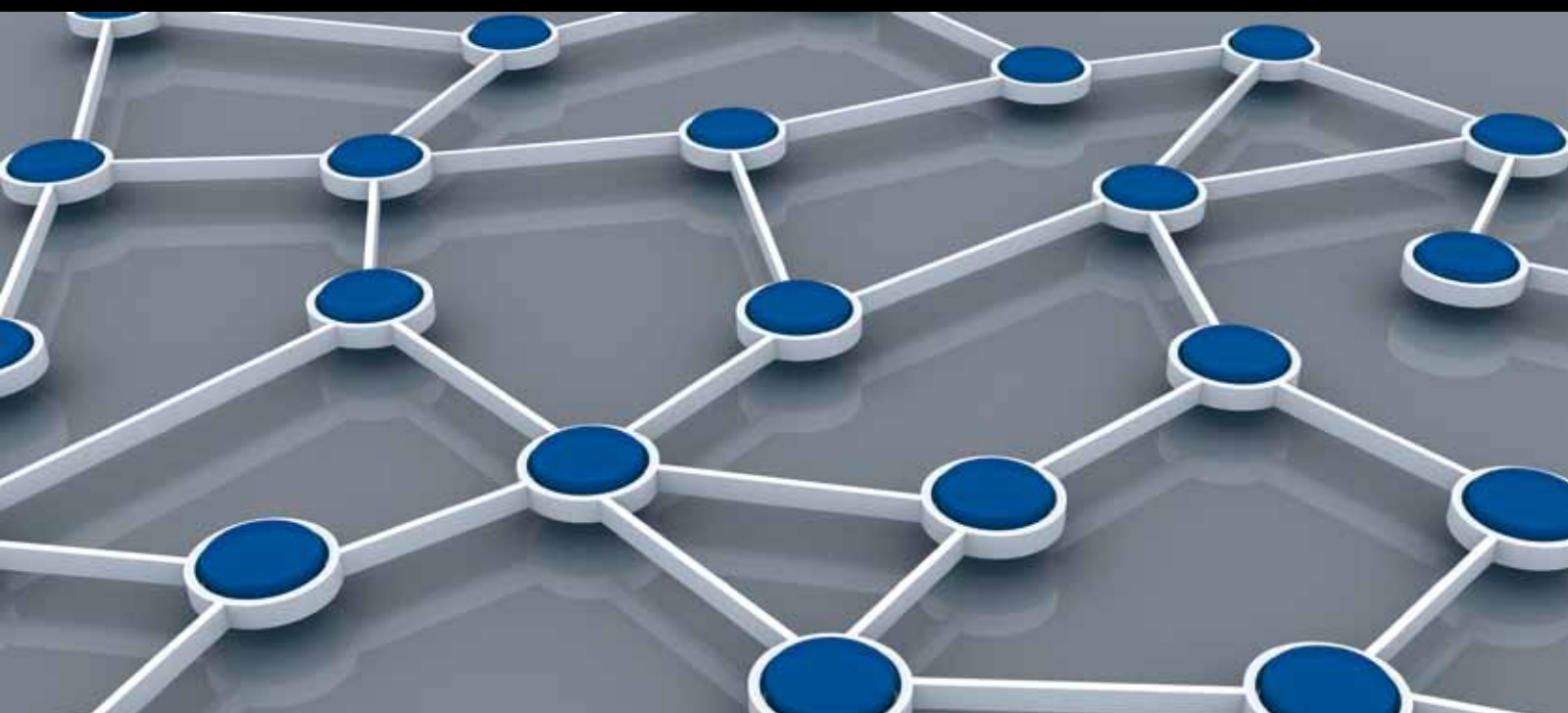


SMART AND RECONFIGURABLE ANTENNA Applications in WIRELESS SENSOR NETWORKS

GUEST EDITORS: KORKUT YEGİN, ADNAN KAVAK, ERDAL CAYIRCI, AND KAPIL DANDEKAR





Smart and Reconfigurable Antenna Applications in Wireless Sensor Networks

Smart and Reconfigurable Antenna Applications in Wireless Sensor Networks

Guest Editors: Korkut Yegin, Adnan Kavak, Erdal Cayirci,
and Kapil Dandekar



Copyright © 2014 Hindawi Publishing Corporation. All rights reserved.

This is a special issue published in “International Journal of Distributed Sensor Networks.” All articles are open access articles distributed under the Creative Commons Attribution License, which permits unrestricted use, distribution, and reproduction in any medium, provided the original work is properly cited.

Editorial Board

Miguel Acevedo, USA
Sanghyun Ahn, Korea
Mohammad Ali, USA
Jamal N. Al-Karaki, Jordan
Habib M. Ammari, USA
Javier Bajo, Spain
Prabir Barooah, USA
Alessandro Bogliolo, Italy
Richard R. Brooks, USA
James Brusey, UK
Erik Buchmann, Germany
Jian-Nong Cao, Hong Kong
João Paulo Carmo, Portugal
Jesús Carretero, Spain
Luca Catarinucci, Italy
Henry Chan, Hong Kong
Chih-Yung Chang, Taiwan
Periklis Chatzimisios, Greece
Ai Chen, China
Peng Cheng, China
Jinsung Cho, Korea
Kim-Kwang Choo, Australia
Chi-Yin Chow, Hong Kong
W.-Y. Chung, Republic of Korea
Mauro Conti, Italy
Dinesh Datla, USA
Amitava Datta, Australia
Danilo De Donno, Italy
Ilker Demirkol, Spain
Chyi-Ren Dow, Taiwan
George P. Efthymoglou, Greece
Frank Ehlers, Italy
Melike Erol-Kantarci, Canada
Giancarlo Fortino, Italy
David Galindo, France
Weihua Gao, USA
Deyun Gao, China
Athanasios Gkelias, UK
Iqbal Gondal, Australia
Jayavardhana Gubbi, Australia
Cagri Gungor, Turkey
Song Guo, Japan
Andrei Gurtov, Finland
Qi Han, USA
Zdenek Hanzalek, Czech Republic

Tian He, USA
Junyoung Heo, Korea
Zujun Hou, Singapore
Jiun-Long Huang, Taiwan
Yung-Fa Huang, Taiwan
Baoqi Huang, China
Chin-Tser Huang, USA
Xinming Huang, USA
Wei Huangfu, China
Mohamed Ibnkahla, Canada
Tan Jindong, USA
Ibrahim Kamel, UAE
Li-Wei Kang, Taiwan
Rajgopal Kannan, USA
Sherif Khattab, Egypt
Lisimachos Kondi, Greece
Marwan Krunz, USA
Kun-Chan Lan, Taiwan
Yee W. Law, Australia
Young-Koo Lee, Republic of Korea
Kyung-Chang Lee, Korea
Yong Lee, USA
JongHyup Lee, Korea
Sungyoung Lee, Republic of Korea
Seokcheon Lee, USA
Joo-Ho Lee, Japan
Shijian Li, China
Minglu Li, China
Shuai Li, USA
Shancang Li, UK
Zhen Li, China
Ye Li, China
Jing Liang, China
Weifa Liang, Australia
Wen-Hwa Liao, Taiwan
Alvin S. Lim, USA
Kai Lin, China
Zhong Liu, China
Ming Liu, China
Donggang Liu, USA
Yonghe Liu, USA
Chuan-Ming Liu, Taiwan
Zhigang Liu, China
Leonardo Lizzi, France
Giuseppe Lo Re, Italy

Seng Loke, Australia
Jonathan Loo, UK
Juan A. L. Riquelme, Spain
Pascal Lorenz, France
KingShan Lui, Hong Kong
Jun Luo, Singapore
Jose Ramiro Martinez-de Dios, Spain
Nirvana Meratnia, The Netherlands
Shabbir N. Merchant, India
Mihael Mohorcic, Slovenia
José Molina, Spain
Vallipuram Muthukkumarasamy, Australia
Eduardo Freire Nakamura, Brazil
Kamesh Namuduri, USA
George Nikolakopoulos, Sweden
Marimuthu Palaniswami, Australia
Ai-Chun Pang, Taiwan
Seung-Jong J. Park, USA
Soo-Hyun Park, Korea
Miguel A. Patricio, Spain
Wen-Chih Peng, Taiwan
Janez Perš, Slovenia
Dirk Pesch, Ireland
Shashi Phoha, USA
Antonio Puliafito, Italy
Hairong Qi, USA
Nageswara Rao, USA
Md. Abdur Razzaque, Bangladesh
Pedro Pereira Rodrigues, Portugal
Joel J. P. C. Rodrigues, Portugal
Jorge Sa Silva, Portugal
Mohamed Saad, UAE
Sanat Sarangi, India
Stefano Savazzi, Italy
Arunabha Sen, USA
Xiao-Jing Shen, China
Weihua Sheng, USA
Louis Shue, Singapore
Antonino Staiano, Italy
Tan-Hsu Tan, Taiwan
Guozhen Tan, China
Shaojie Tang, USA
Bulent Tavli, Turkey
Anthony Tzes, Greece
Agustinus B. Waluyo, Australia



Yu Wang, USA
Ran Wolff, Israel
Jianshe Wu, China
Wenjong Wu, Taiwan
Chase Qishi Wu, USA
Bin Xiao, Hong Kong
Qin Xin, Faroe Islands
Jianliang Xu, Hong Kong

Yuan Xue, USA
Ting Yang, China
Hong-Hsu Yen, Taiwan
Li-Hsing Yen, Taiwan
Seong-eun Yoo, Korea
Ning Yu, China
Changyuan Yu, Singapore
Tianle Zhang, China

Yanmin Zhu, China
T. L. Zhu, USA
Yi-hua Zhu, China
Qingxin Zhu, China
Li Zhuo, China
Shihong Zou, China

Contents

Smart and Reconfigurable Antenna Applications in Wireless Sensor Networks, Korkut Yegin, Adnan Kavak, Erdal Cayirci, and Kapil Dandekar
Volume 2014, Article ID 658792, 2 pages

Fast 3D Node Localization in Multipath for UWB Wireless Sensor Networks Using Modified Propagator Method, Hong Jiang, Chang Liu, Yu Zhang, and Haijing Cui
Volume 2014, Article ID 312535, 8 pages

Polarization Reconfigurable Patch Antenna for Wireless Sensor Network Applications, Mustafa Murat Bilgiç and Korkut Yeğin
Volume 2013, Article ID 967329, 5 pages

Footstep and Vehicle Detection Using Seismic Sensors in Wireless Sensor Network: Field Tests, Gökhan Koç and Korkut Yegin
Volume 2013, Article ID 120386, 8 pages

Footstep and Vehicle Detection Using Slow and Quick Adaptive Thresholds Algorithm, Gökhan Koç and Korkut Yegin
Volume 2013, Article ID 783604, 9 pages

Reconfigurable Antenna Assisted Intrusion Detection in Wireless Networks, Prathaban Mookiah, John M. Walsh, Rachel Greenstadt, and Kapil R. Dandekar
Volume 2013, Article ID 564503, 12 pages

Hardware Design of Seismic Sensors in Wireless Sensor Network, Gokhan Koc and Korkut Yegin
Volume 2013, Article ID 640692, 8 pages

Circular Collaborative Beamforming for Improved Radiation Beampattern in WSN, N. N. Nik Abd Malik, M. Esa, S. K. Syed Yusof, S. A. Hamzah, and M. K. H. Ismail
Volume 2013, Article ID 125423, 9 pages

On the Efficiency of Capacitively Loaded Frequency Reconfigurable Antennas, Samantha Caporal Del Barrio and Gert F. Pedersen
Volume 2013, Article ID 232909, 8 pages

Editorial

Smart and Reconfigurable Antenna Applications in Wireless Sensor Networks

Korkut Yegin,¹ Adnan Kavak,² Erdal Cayirci,³ and Kapil Dandekar⁴

¹ *Department of Electrical and Electronics Engineering, RF Electronics and Antennas Research Lab, Yeditepe University, 34755 Istanbul, Turkey*

² *Department of Computer Engineering, Wireless Communications and Information Systems Research Unit, Kocaeli University, İzmit, 41380 Kocaeli, Turkey*

³ *Electrical Engineering and Computer Science Department, University of Stavanger, 4036 Stavanger, Norway*

⁴ *Drexel Wireless System Laboratory, Department of Electrical and Computer Engineering, Drexel University, Philadelphia, PA 19104, USA*

Correspondence should be addressed to Adnan Kavak; akavak@kocaeli.edu.tr

Received 11 January 2014; Accepted 11 January 2014; Published 27 February 2014

Copyright © 2014 Korkut Yegin et al. This is an open access article distributed under the Creative Commons Attribution License, which permits unrestricted use, distribution, and reproduction in any medium, provided the original work is properly cited.

Wireless Sensor Networks (WSNs) are a prominent technology with diverse applications. Considerable amount of research effort has been devoted to energy minimization of limited power resources and reliable communication between the nodes and the gateway. Most of these studies rely on the software/algorithm improvement of WSNs, but there is definitely lack of hardware devoted research and its implementation on the network. This special issue aims to bridge this gap by exploiting application of proven technologies to WSNs to overcome the disadvantages of WSNs.

The smart antenna system (SAS) is one of the critical technologies where traditional communication systems such as cellular, personal communication systems have experienced great benefits. For the application of SAS in WSNs, adaptive and/or reconfigurable antenna structures play a key role in the radiation pattern and polarization of the node antenna. One paper addresses a novel node antenna where the polarization of the antenna can be reconfigured among all principal polarizations (LP, VP, RHCP, and LHCP) by means of control switches whose states can be controlled by a microcontroller. Such adaptive antenna systems are crucial in multipath fading environments.

Another paper studies the field performance of seismic sensors for intruder detection. Seismic sensors were integrated into a WSN where the critical data such as alarm conditions were transferred to the wireless network. Field

performance of such applications is important for recognizing the shortcomings of the WSN in a real operating environment.

One of the papers addresses a memory efficient algorithm for intruder detection application of WSNs. Because the system operated in real time, the efficiency, accuracy, and reliability of the detection and classification algorithm played a vital role and the capabilities of the proposed algorithm were tested to full extent.

There is a paper that addresses the capabilities of reconfigurable antennas that can be used to devise an intrusion detection scheme which operates at the physical layer. The performance of the proposed scheme was quantified through field measurements taken in an indoor environment at the 802.11 frequency band.

One paper discusses the hardware issues such as noise, matched filtering, and amplification of small signals that were obtained through seismic sensors. Such sensors are abundantly used for outdoor intruder detection but there is little information in open literature about the design and realization of practical sensors in a limited power application of WSNs.

Another paper presents a novel collaborative beamforming (CB) method for WSNs by organizing sensor node location in a circular arrangement. The nodes were modeled in circular array location to consider it as a circular antenna

array. This newly proposed circular collaborative beamforming was further investigated to solve two different objectives: sidelobe level suppression and first null beamwidth improvement.

One of the papers discusses the design of a reconfigurable antenna that can be fine-tuned to address future communication systems. The design consisted of a capacitively loaded patch antenna for smartphone platforms. It was shown that a narrowband antenna could be fine-tuned over the range of 700 MHz–960 MHz. Distribution of the tuning capacitance was also investigated and improvement in the antenna radiation efficiency was observed.

Acknowledgment

We also would like to thank the reviewers for maintaining high quality and timely reviews for this special issue.

*Korkut Yegin
Adnan Kavak
Erdal Cayirci
Kapil Dandekar*

Research Article

Fast 3D Node Localization in Multipath for UWB Wireless Sensor Networks Using Modified Propagator Method

Hong Jiang,¹ Chang Liu,² Yu Zhang,¹ and Haijing Cui¹

¹ College of Communication Engineering, Jilin University, Changchun 130012, China

² Department of Electrical and Computer Engineering, Kansas State University, Manhattan, KS 66502, USA

Correspondence should be addressed to Hong Jiang; jiangh@jlu.edu.cn

Received 25 May 2013; Revised 13 November 2013; Accepted 3 December 2013; Published 9 February 2014

Academic Editor: Kapil Dandekar

Copyright © 2014 Hong Jiang et al. This is an open access article distributed under the Creative Commons Attribution License, which permits unrestricted use, distribution, and reproduction in any medium, provided the original work is properly cited.

A fast three-dimensional (3D) node localization algorithm in multipath for ultra-wideband (UWB) wireless sensor networks is developed. The algorithm employs a modified propagator method (MPM) for time delay estimation and then uses a marriage algorithm of 3D Chan and Taylor for range-based multilateral localization and node position computation. In the proposed algorithm, the traditional propagator method (PM) for direction-of-arrival (DOA) estimation is extended to frequency-domain time-of-arrival (TOA) estimation in multipath, which can effectively measure the distance between an unknown sensor node and an anchor node. MPM algorithm requires neither spectral searching nor covariance matrix estimation and its eigenvalue decomposition, which reduces the computational complexity. The marriage location algorithm enhances the robustness and accuracy of node localization. The simulations validate the effectiveness of the proposed algorithm in locating multiple unknown nodes of UWB wireless sensor networks in 3D space.

1. Introduction

Ranging and localization of unknown sensor nodes in wireless sensor networks (WSNs) [1] have drawn considerable attention in many aspects such as environmental monitoring, health tracking, smart home, machine-to-machine (M2M), and body area networks (BAN). In actual environment, the sensor nodes are commonly placed in three-dimensional (3D) terrains, such as workshops, forests, and oceans. Recently, several range-based and range-free 3D node localization algorithms in WSNs have been proposed [2–6]. However, some problems should be investigated in node design and implementation, such as large computational amount, slow executing, and inaccurate localization in multipath and noise. Since the energy and power carried by node equipment are limited, effective methods with low complexity, low power consumption, and good robustness for 3D node positioning are of great significance.

This paper investigates fast 3D node localization problem based on time delay measurement in multipath in ultra-wideband (UWB) wireless sensor networks. As we know, time delay estimation problem has been studied with a variety of

super-resolution subspace techniques [7–11], such as multiple signal classification (MUSIC), total least square-estimation of signal parameters via rotational invariance technique (TLS-ESPRIT), and matrix pencil (MP). Compared with the correlator-based methods, subspace-based algorithms can increase time resolution even if the time delay is smaller than a pulse width. Unfortunately, these techniques increase the complexity of WSN implementation. Specifically, in MUSIC algorithm, spectral searching is needed through all the space, which increases its computational time. ESPRIT-like algorithms require the covariance matrix estimation of the observed data using a large number of snapshots and then performing eigenvalue decomposition (EVD) or singular value decomposition (SVD) of it. In [12], we developed a unitary matrix pencil (UMP) based delay estimation algorithm for 3D localization in UWB wireless sensor networks, which can reduce the complexity load. However, its estimation accuracy is lower than many subspace-based methods.

The propagator method (PM), developed in [13], is a traditional subspace method previously used in the direction-of-arrival (DOA) estimation. In [14], we extend it to the time-of-arrival (TOA) estimation. PM algorithm only requires linear

operations, and thus it avoids covariance matrix estimation and its EVD or SVD which are the main computational burden in subspace methods. However, similar to MUSIC algorithm, a spectral peak searching through all the space is needed in traditional PM algorithm.

In this paper, we develop a fast range-based 3D node localization algorithm in multipath for UWB wireless sensor networks. The algorithm employs a modified propagator method (MPM) for frequency-domain time delay estimation and then uses a marriage algorithm of 3D Chan and Taylor for range-based multilateral localization and node position computation. The MPM algorithm requires neither spectral searching nor covariance matrix estimation and its eigenvalue decomposition, which can reduce the computational load. Furthermore, the marriage localization algorithm can enhance the robustness and accuracy of node localization in comparison with the previous algorithm in [15]. The simulations validate the effectiveness of the proposed algorithm in locating multiple unknown nodes of UWB wireless sensor networks in 3D space.

This paper is organized as follows. In Section 2, the UWB received signal model for multipath time delay estimation is given. MPM-based multipath delay estimation algorithm is proposed in Section 3. Based on it, the multilateral localization and node position computation using a marriage of 3D Chan and Taylor algorithms are presented in Section 4. In Section 5, the simulation results are given to verify the performance of the proposed method. Finally, a conclusion is drawn in Section 6.

2. Signal Model

Assume that an ultra-wideband pulse is transmitted from an unknown node to an anchor node through L paths. During the q th snapshot, $q = 1, \dots, Q$, the received signal can be expressed as

$$y^{(q)}(t) = \sum_{l=1}^L \beta_l^{(q)} p(t - \tau_{\text{TOA}} - \Delta\tau_l) + w^{(q)}(t), \quad (1)$$

where $p(t)$ denotes a UWB signal having basic Gaussian pulse waveform $p(t) = A_p e^{-2\pi t^2/T_p^2}$, with A_p and T_p being the amplitude and pulse width of the UWB signal, respectively. $w^{(q)}(t)$ denotes the complex additive Gaussian white noise. τ_{TOA} denotes the TOA of the unknown node, and $\Delta\tau_l$ and $\beta_l^{(q)}$ represent the relative delay and time-varying complex fading amplitude of the l th path, respectively: $\Delta\tau_1 = 0$. Denote $\tau_l = \tau_{\text{TOA}} + \Delta\tau_l$ as the total propagation time delay of the l th path. Then, the received signal in (1) can be rewritten as

$$y^{(q)}(t) = \sum_{l=1}^L \beta_l^{(q)} p(t - \tau_l) + w^{(q)}(t). \quad (2)$$

The channel impulse response of UWB signal in multipath is a sum of L components shifted from the corresponding time delays. Upon discrete Fourier transform and matched filtering based on (2), the frequency-domain

representation of the identified channel signal can be written as

$$\begin{aligned} H^{(q)}(k) &= \sum_{l=1}^L \beta_l^{(q)} e^{-j(2\pi k\tau_l/KT)} + V^{(q)}(k) \\ &= \sum_{l=1}^L \beta_l^{(q)} z_l^k + V^{(q)}(k), \end{aligned} \quad (3)$$

$k = 0, 1, \dots, K-1$, with K denoting the number of discrete Fourier transforms and T being the sampling period. $V^{(q)}(k)$ denotes the frequency-domain noise, τ_l is the estimated delay parameter, and $z_l = e^{-j(2\pi\tau_l/KT)}$.

Collecting the data of all the Q snapshots from (3) yields an observed data matrix:

$$\mathbf{H} = \mathbf{Z}(\tau) \mathbf{B} + \mathbf{V}, \quad (4)$$

where $\mathbf{H} \in \mathbb{C}^{K \times Q}$ and $\mathbf{V} \in \mathbb{C}^{K \times Q}$ denote the observed matrix and noise matrix, respectively. $\mathbf{Z}(\tau)$ denotes the time delay matrix:

$$\mathbf{Z}(\tau) = \begin{bmatrix} 1 & \cdots & 1 \\ z_1 & \cdots & z_L \\ \vdots & \ddots & \vdots \\ z_1^{K-1} & \cdots & z_L^{K-1} \end{bmatrix}_{K \times L}, \quad (5)$$

and $\mathbf{B} \in \mathbb{C}^{L \times Q}$ denotes the fading amplitude matrix:

$$\mathbf{B} = \begin{bmatrix} \beta_1^{(1)} & \cdots & \beta_1^{(Q)} \\ \vdots & \cdots & \vdots \\ \beta_L^{(1)} & \cdots & \beta_L^{(Q)} \end{bmatrix}. \quad (6)$$

The problem interest is to estimate the parameter τ_l based on the observed matrix in (4), $l = 1, \dots, L$.

3. Multipath Delay Estimation Using Modified Propagator Method

3.1. Review of Traditional Propagator Method. Let us first review the traditional propagator method. The propagator method is previously presented in DOA estimation [13]. We introduce its application in TOA estimation [14].

From (5), it is noted that $\mathbf{Z}(\tau)$, as a Vandermonde matrix, is of full column rank with L linearly independent rows. The other $K-L$ rows can be expressed as a linear combination of these L rows. Therefore, $\mathbf{Z}(\tau)$ can be partitioned into

$$\mathbf{Z}(\tau) = \left[\begin{array}{c} \mathbf{Z}_1(\tau) \\ \mathbf{Z}_2(\tau) \end{array} \right] \begin{array}{l} \} L \\ \} K-L, \end{array} \quad (7)$$

where $\mathbf{Z}_1(\tau) \in \mathbb{C}^{L \times L}$ and $\mathbf{Z}_2(\tau) \in \mathbb{C}^{(K-L) \times L}$. The propagator is the unique linear operator \mathbf{P} of \mathbb{C}^{K-L} into \mathbb{C}^L such that

$$\mathbf{P}^H \mathbf{Z}_1(\tau) = \mathbf{Z}_2(\tau) \quad (8)$$

or

$$\left[\mathbf{P}^H, -\mathbf{I}_{K-L} \right] \mathbf{Z}(\tau) = \mathbf{Q}^H \mathbf{Z}(\tau) = \mathbf{0}, \quad (9)$$

where H denotes the Hermitian transpose. $\mathbf{I}_{K-L} \in \mathbb{R}^{(K-L) \times (K-L)}$ and $\mathbf{0} \in \mathbb{R}^{(K-L) \times L}$ denote the identity matrix and null matrix, respectively, and the matrix \mathbf{Q} is given by

$$\mathbf{Q} \triangleq \begin{bmatrix} \mathbf{P} \\ -\mathbf{I}_{K-L} \end{bmatrix}. \quad (10)$$

Equation (9) reveals that $\mathbf{Z}(\tau)$ is orthogonal to the columns of \mathbf{Q} . Therefore, the following TOA estimator can find the peaks of the spectrum:

$$F_{\text{PM}}(\tau) = \frac{1}{\mathbf{Z}^H(\tau) \mathbf{Q} \mathbf{Q}^H \mathbf{Z}(\tau)}. \quad (11)$$

In (11), \mathbf{Q} can be effectively estimated from the linear operations of the observed data. We similarly partition the observed matrix \mathbf{H} in (4) into

$$\mathbf{H} = \begin{bmatrix} \mathbf{H}_1 \\ \mathbf{H}_2 \end{bmatrix} \begin{matrix} \} L \\ \} K-L, \end{matrix} \quad (12)$$

where $\mathbf{H}_1 \in \mathbb{C}^{L \times Q}$ and $\mathbf{H}_2 \in \mathbb{C}^{(K-L) \times Q}$. In the noise-free case, from (4), (8), and (12), it yields

$$\mathbf{H}_2 = \mathbf{P}^H \mathbf{H}_1. \quad (13)$$

In the presence of noise, a least squares (LS) estimate of the propagator operator \mathbf{P} is

$$\hat{\mathbf{P}} = (\mathbf{H}_2 \mathbf{H}_1^+)^H, \quad (14)$$

where \mathbf{H}_1^+ is the Moore-Penrose pseudo inverse of \mathbf{H}_1 , $\mathbf{H}_1^+ = (\mathbf{H}_1^H \mathbf{H}_1)^{-1} \mathbf{H}_1^H$. Thus the estimate of \mathbf{Q} can be calculated from (10).

3.2. The Modified Propagator Method. The traditional propagator method can reduce computational load compared with the common subspace techniques such as MUSIC and ESPRIT since it uses linear operations on the observed data, avoiding the EVD or SVD of covariance matrix. However, it reveals from (11) that long time is needed for spectral peak searching through all the scope of time delays. To avoid it, we combine the idea of shift invariance with propagator method in the paper, presenting a modified propagator method (MPM) for multipath delay estimation.

Let \mathbf{H}_1 and \mathbf{H}_2 be two $(K-1) \times Q$ submatrices of the matrix \mathbf{H} consisting of the first and last $K-1$ rows of \mathbf{H} ; then,

$$\mathbf{H}_1 = \mathbf{Z}_1(\tau) \mathbf{B} + \mathbf{V}_1, \quad \mathbf{H}_2 = \mathbf{Z}_2(\tau) \mathbf{B} + \mathbf{V}_2, \quad (15)$$

where $\mathbf{Z}_1(\tau)$ and $\mathbf{Z}_2(\tau)$ are the first and last $K-1$ rows of the matrix $\mathbf{Z}(\tau)$, respectively. Thus, we have

$$\mathbf{Z}_2(\tau) = \mathbf{Z}_1(\tau) \Phi, \quad (16)$$

where $\Phi = \text{diag}\{e^{-j(2\pi\tau_1/KT)}, \dots, e^{-j(2\pi\tau_L/KT)}\}$ is a diagonal matrix, which contains the estimated time delay parameters τ_1, \dots, τ_L .

Compose the two matrices \mathbf{H}_1 and \mathbf{H}_2 to form a $2(K-1) \times Q$ matrix:

$$\mathbf{X} = \begin{bmatrix} \mathbf{H}_1 \\ \mathbf{H}_2 \end{bmatrix} = \begin{bmatrix} \mathbf{Z}_1(\tau) \\ \mathbf{Z}_1(\tau) \Phi \end{bmatrix} \mathbf{B} + \begin{bmatrix} \mathbf{V}_1 \\ \mathbf{V}_2 \end{bmatrix} = \mathbf{D}(\tau) \mathbf{B} + \mathbf{N}, \quad (17)$$

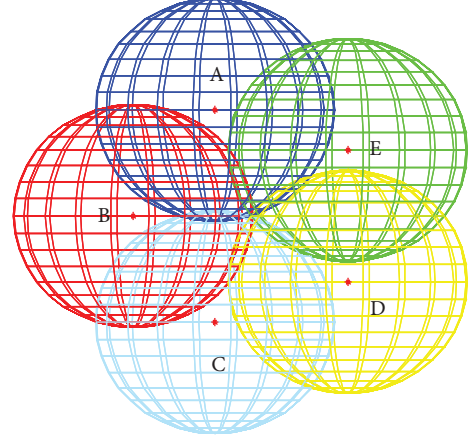


FIGURE 1: The geometric relationship of 3D multilateral localization with five anchor nodes.

where $\mathbf{D}(\tau)$ is a $2(K-1) \times L$ delay matrix and \mathbf{N} is the noise matrix upon composition.

From the idea of propagator method, if $\mathbf{D}(\tau)$ is partitioned into

$$\mathbf{D}(\tau) = \begin{bmatrix} \mathbf{D}_1(\tau) \\ \mathbf{D}_2(\tau) \end{bmatrix} \begin{matrix} \} L \\ \} 2(K-L)-L, \end{matrix} \quad (18)$$

then there exists a unique propagator operator \mathbf{P} satisfying

$$\mathbf{P}^H \mathbf{D}_1(\tau) = \mathbf{D}_2(\tau). \quad (19)$$

Similarly, the matrix \mathbf{X} can be partitioned into two matrices \mathbf{X}_1 and \mathbf{X}_2 in the same way as $\mathbf{D}(\tau)$. If the noise matrix \mathbf{N} is ignored, then

$$\mathbf{X}_1 = \mathbf{D}_1(\tau) \mathbf{B}, \quad \mathbf{X}_2 = \mathbf{D}_2(\tau) \mathbf{B}. \quad (20)$$

Premultiply \mathbf{P}^H in \mathbf{X}_1 yielding

$$\mathbf{P}^H \mathbf{X}_1 = \mathbf{P}^H \mathbf{D}_1(\tau) \mathbf{B} = \mathbf{D}_2(\tau) \mathbf{B} = \mathbf{X}_2. \quad (21)$$

In the noisy environment, \mathbf{P} can be achieved by the LS solution; that is,

$$\mathbf{P} = (\mathbf{X}_2 \mathbf{X}_1^H (\mathbf{X}_1 \mathbf{X}_1^H)^{-1})^H. \quad (22)$$

Let $\tilde{\mathbf{P}} = \begin{bmatrix} \mathbf{I}_L \\ \mathbf{P}^H \end{bmatrix}$, where \mathbf{I}_L is a $L \times L$ identity matrix; then

$$\tilde{\mathbf{P}} \mathbf{D}_1(\tau) = \begin{bmatrix} \mathbf{I}_L \\ \mathbf{P}^H \end{bmatrix} \mathbf{D}_1(\tau) = \begin{bmatrix} \mathbf{D}_1(\tau) \\ \mathbf{D}_2(\tau) \end{bmatrix} = \mathbf{D}(\tau). \quad (23)$$

From (23), we observe that $\tilde{\mathbf{P}}$ spans signal subspace. Evenly dividing $\tilde{\mathbf{P}}$ into two $(K-1) \times L$ matrices $\tilde{\mathbf{P}}_1$ and $\tilde{\mathbf{P}}_2$ and based on (17), we have

$$\begin{bmatrix} \tilde{\mathbf{P}}_1 \\ \tilde{\mathbf{P}}_2 \end{bmatrix} \mathbf{D}_1(\tau) = \begin{bmatrix} \mathbf{Z}_1(\tau) \\ \mathbf{Z}_1(\tau) \Phi \end{bmatrix}. \quad (24)$$

Therefore,

$$\mathbf{Z}_1(\tau) \Phi = \Psi \mathbf{Z}_1(\tau), \quad (25)$$

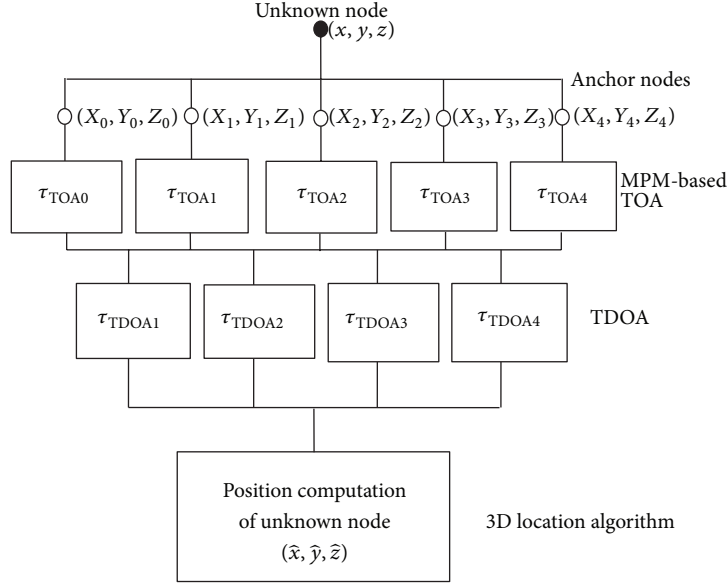


FIGURE 2: Procedure of locating an unknown node with five anchor nodes.

where $\Psi = \tilde{\mathbf{P}}_2(\tilde{\mathbf{P}}_1^H \tilde{\mathbf{P}}_1)^{-1} \tilde{\mathbf{P}}_1^H$. It is shown from (25) that Φ is the eigenvalue matrix of Ψ . Therefore, the time delays of L paths can be calculated from L main diagonal elements of Φ ; that is,

$$\hat{\tau}_l = \frac{KT}{2\pi} \text{angle}(\lambda_l), \quad (26)$$

where λ_l is the l th eigenvalue of Φ , for $l = 1, \dots, L$.

The procedure of MPM-based time delay estimation algorithm can be summarized as follows.

- (i) Divide the observed matrix \mathbf{H} into \mathbf{H}_1 and \mathbf{H}_2 consisting of the first and last $K-1$ rows of \mathbf{H} , respectively.
- (ii) Compose \mathbf{H}_1 and \mathbf{H}_2 to form a $2(K-1) \times Q$ matrix \mathbf{X} . Partition \mathbf{X} into $\mathbf{X} = [\mathbf{X}_1^T, \mathbf{X}_2^T]^T$ such that $\mathbf{X}_1 \in \mathbb{C}^{L \times Q}$ and $\mathbf{X}_2 \in \mathbb{C}^{(2(K-1)-L) \times Q}$.
- (iii) Obtain the propagator $\mathbf{P} = (\mathbf{X}_2 \mathbf{X}_1^H (\mathbf{X}_1 \mathbf{X}_1^H)^{-1})^H$. Let $\tilde{\mathbf{P}} = \begin{bmatrix} \mathbf{I}_L \\ \mathbf{p}^H \end{bmatrix}$, and evenly divide $\tilde{\mathbf{P}}$ into two $(K-1) \times L$ matrices $\tilde{\mathbf{P}}_1$ and $\tilde{\mathbf{P}}_2$.
- (iv) Calculate the eigenvalue matrix Φ of the matrix $\Psi = \tilde{\mathbf{P}}_2(\tilde{\mathbf{P}}_1^H \tilde{\mathbf{P}}_1)^{-1} \tilde{\mathbf{P}}_1^H$. Then, $\hat{\tau}_l$ can be obtained from the diagonal elements of Φ .

4. Node Position Computation Algorithm

4.1. Multilateral Localization. From the results of MPM-based multipath delay estimation given in (26), the τ_{TOA} and distance r from an unknown node to anchor nodes can be determined. In the following procedure of 3D node position computation, we consider multilateral localization other than trilateral localization to improve the accuracy. The number of anchor nodes is no less than five in our algorithm. A geometry relationship of the cross point of spheres with five anchor nodes (A, B, C, D, E) is shown in Figure 1.

Assume that (x, y, z) denotes the coordinate of an unknown node. (X_0, Y_0, Z_0) represents the coordinate of a main anchor node, and (X_i, Y_i, Z_i) represents the coordinate of the other anchor nodes, $i = 1, 2, \dots, M-1$, with M denoting the number of anchor nodes. Let t be the time of the transmitted UWB signal by the unknown node and let t_i be the time of the received first-path signal by the i th anchor node. Then, the distance between the unknown node and the i th anchor node is $r_i = c(t_i - t) = c\tau_{\text{TOA}i}$. The equation of 3D node position computation can be written by

$$\begin{aligned} r_0^2 &= (x - X_0)^2 + (y - Y_0)^2 + (z - Z_0)^2, \\ r_i^2 &= (x - X_i)^2 + (y - Y_i)^2 + (z - Z_i)^2, \\ \Delta r_i &= r_i - r_0 = c\tau_{\text{TDOA}i}, \end{aligned} \quad (27)$$

where c denotes the velocity of wave, Δr_i and $\tau_{\text{TDOA}i}$ denote the distance difference and time-difference-of-arrival (TDOA) from the unknown node to the i th anchor node and to the main anchor node, and $\tau_{\text{TDOA}i} = \tau_{\text{TOA}i} - \tau_{\text{TOA}0}$, $i = 1, 2, \dots, M-1$.

Chan algorithm [16] and Taylor algorithm [17] are two traditional methods to solve nonlinear positioning equations for radio location in a 2D space. Chan algorithm has low computational complexity and high accuracy in high signal-noise-ratio (SNR) and Gaussian noise environment. However, with the increase of TOA measurement error, the performance of Chan algorithm in low SNR environment will degrade. Taylor algorithm has higher accuracy and good robustness in noise. However, the performance of Taylor algorithm is highly dependent on the initial estimate of iterative computation. An improper initial estimate will lead to non convergence.

In the paper, we present a marriage algorithm of 3D Chan and Taylor location to calculate the 3D position of unknown

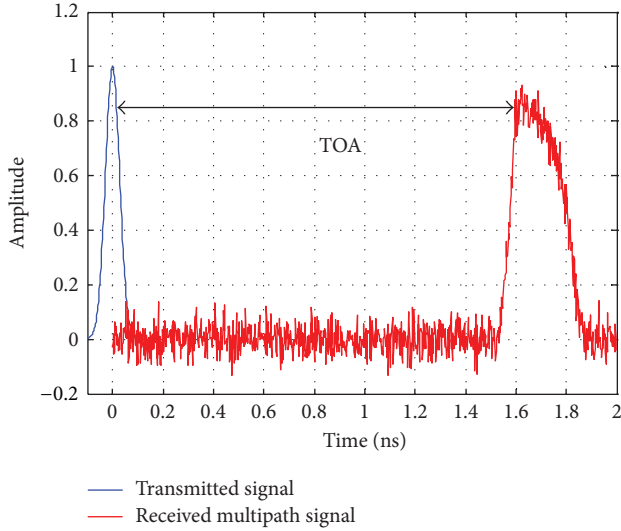


FIGURE 3: The transmitted UWB signal and the received multipath superposition signal.

TABLE 1: MPM-based delay estimation results when SNR = 0 dB.

Path delays	True (ns)	Estimate (ns)
Path 1	1.60	1.594
Path 2	1.65	1.643
Path 3	1.70	1.695
Path 4	1.75	1.752
Path 5	1.80	1.797

node. Figure 2 shows the procedure of locating an unknown node with $M = 5$ anchor nodes.

4.2. 3D Chan Algorithm. The traditional Chan algorithm can be extended from 2D space to 3D space. From the positioning equation in (27), we have

$$(X_0 - X_i)x + (Y_0 - Y_i)y + (Z_0 - Z_i)z = k_i + r_0\Delta r_i, \quad (28)$$

where $k_i = (1/2)[\Delta r_i^2 - (X_i^2 + Y_i^2 + Z_i^2) + (X_0^2 + Y_0^2 + Z_0^2)]$ for $i = 1, 2, \dots, M-1$. The coordinate (x, y, z) of unknown node can be obtained using the weighted LS (WLS) solution [18] for in (28), and thus,

$$\begin{bmatrix} x \\ y \\ z \end{bmatrix} = - \begin{bmatrix} X_{1,0} & Y_{1,0} & Z_{1,0} \\ X_{2,0} & Y_{2,0} & Z_{2,0} \\ \vdots & \vdots & \vdots \\ X_{M-1,0} & Y_{M-1,0} & Z_{M-1,0} \end{bmatrix}^+ \times \left\{ \frac{1}{2} \begin{bmatrix} \Delta r_1^2 - K_1 + K_0 \\ \Delta r_2^2 - K_2 + K_0 \\ \vdots \\ \Delta r_{M-1}^2 - K_{M-1} + K_0 \end{bmatrix} + \begin{bmatrix} \Delta r_1 \\ \Delta r_2 \\ \vdots \\ \Delta r_{M-1} \end{bmatrix} r_0 \right\}, \quad (29)$$

where $X_{i,0} = X_i - X_0$, $Y_{i,0} = Y_i - Y_0$, $Z_{i,0} = Z_i - Z_0$, $K_i = X_i^2 + Y_i^2 + Z_i^2$, $K_0 = X_0^2 + Y_0^2 + Z_0^2$, and “+” denotes pseudoinverse of a matrix.

In (29), since r_0 contains unknown coordinate (x, y, z) , substituting (29) into (27) yields a second-order equation with respect to r_0 . Obtaining the WLS solution of r_0 and substituting its positive root into (29), we can attain an accurate position estimate $(\hat{x}, \hat{y}, \hat{z})$ of unknown node.

4.3. 3D Taylor Algorithm. Similarly, Taylor algorithm can also be extended to 3D space. Starting with an initial estimate $(x^{(0)}, y^{(0)}, z^{(0)})$, the 3D Taylor algorithm iteratively calculates the position error Δ using WLS:

$$\Delta = \begin{bmatrix} \Delta x \\ \Delta y \\ \Delta z \end{bmatrix} = (\mathbf{G}^T \mathbf{Q}^{-1} \mathbf{G})^{-1} \mathbf{G}^T \mathbf{Q}^{-1} \mathbf{h}, \quad (30)$$

where \mathbf{Q} is the covariance matrix of TDOA measurement. Consider the following:

$$\mathbf{G} = \begin{bmatrix} \frac{(X_0 - x)}{r_0} - \frac{(X_1 - x)}{r_1} & \frac{(Y_0 - y)}{r_0} - \frac{(Y_1 - y)}{r_1} & \frac{(Z_0 - z)}{r_0} - \frac{(Z_1 - z)}{r_1} \\ \frac{(X_0 - x)}{r_0} - \frac{(X_2 - x)}{r_2} & \frac{(Y_0 - y)}{r_0} - \frac{(Y_2 - y)}{r_2} & \frac{(Z_0 - z)}{r_0} - \frac{(Z_2 - z)}{r_2} \\ \vdots & \vdots & \vdots \\ \frac{(X_0 - x)}{r_0} - \frac{(X_{M-1} - x)}{r_{M-1}} & \frac{(Y_0 - y)}{r_0} - \frac{(Y_{M-1} - y)}{r_{M-1}} & \frac{(Z_0 - z)}{r_0} - \frac{(Z_{M-1} - z)}{r_{M-1}} \end{bmatrix}, \quad (31)$$

$$\mathbf{h} = \begin{bmatrix} \Delta r_1 - (r_1 - r_0) \\ \Delta r_2 - (r_2 - r_0) \\ \vdots \\ \Delta r_{M-1} - (r_{M-1} - r_0) \end{bmatrix}.$$

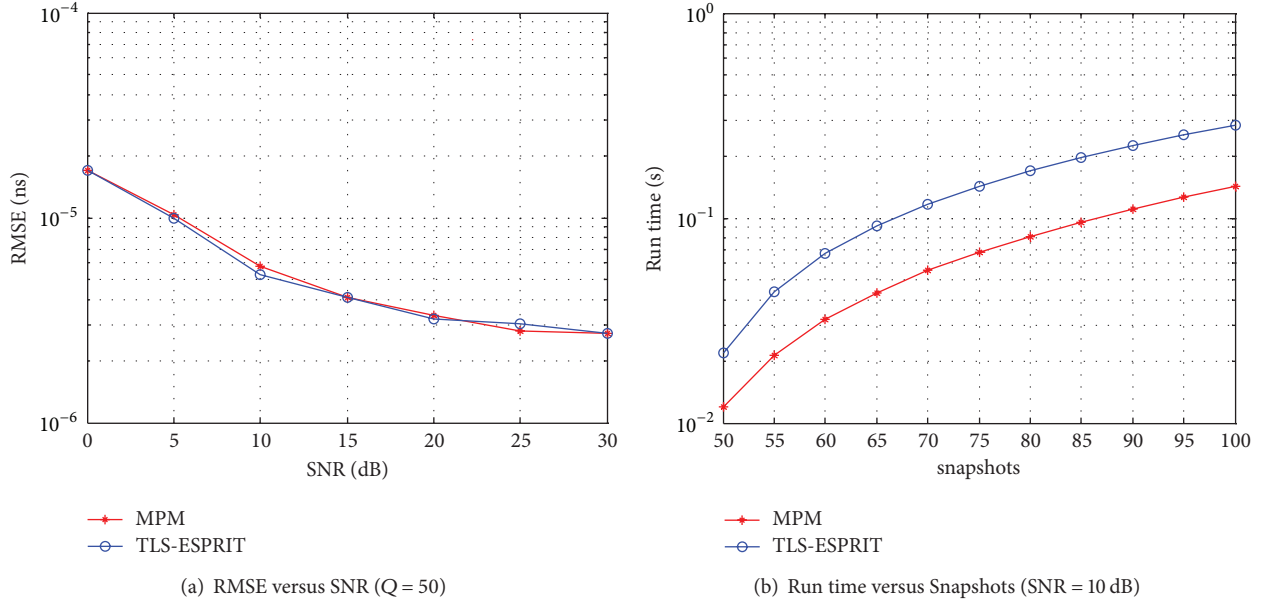


FIGURE 4: Performance comparison between MPM and TLS-ESPRIT.

4.4. Marriage of 3D Chan/Taylor Location. Based on the two algorithms mentioned above, a marriage algorithm of 3D Chan and Taylor location is presented to calculate the 3D position of the unknown node. The procedure is as follows. In the first step, 3D Chan algorithm is employed to calculate the estimated coordinate of an unknown node based on (29), denoted by $(\tilde{x}, \tilde{y}, \tilde{z})$. In the following step, taking the result of 3D Chan algorithm as an initial value of Taylor series expansion, 3D Taylor algorithm is used to iteratively calculate the location error Δ in (30). The iterative procedure has ended until Δ is smaller than a threshold. Then, an accurate estimate of the node position can be calculated by

$$\begin{bmatrix} \hat{x} \\ \hat{y} \\ \hat{z} \end{bmatrix} = \begin{bmatrix} \tilde{x} \\ \tilde{y} \\ \tilde{z} \end{bmatrix}_{\text{Chan}} + \begin{bmatrix} \Delta x \\ \Delta y \\ \Delta z \end{bmatrix}_{\text{Taylor}}. \quad (32)$$

Therefore, the 3D location method inherits the advantages of Chan and Taylor algorithms, having small computational complexity, high accuracy, and good robustness in noise.

5. Simulations

In the simulations, the performance improvement achieved by the MPM is presented. Then, node localization accuracy using MPM-based multipath delay estimation and the marriage of 3D Chan/Taylor location is verified.

5.1. MPM-Based Multipath Delay Estimation Results. The transmitted UWB signal ($T_p = 0.1$ ns, $A_p = 1$) and the received five-path superposition signal are shown in Figure 3.

Table 1 illustrates the results of time delay estimation using the proposed MPM algorithm. SNR = 0 dB. $L = 5$. $Q =$

100. $K = 100$. $T = 0.04$ ns. The simulations confirm high-resolution performance of the proposed MPM-based delay estimation algorithm in multipath environment, even at lower SNRs.

Figure 4 presents the comparison of root mean square error (RMSE) and run time between the MPM algorithm and TLS-ESPRIT algorithm [10]. There are $L = 3$ paths with time delays 1.6 ns, 1.7 ns, and 1.8 ns. $K = 40$. $T = 0.1$ ns, with 100 Monte Carlo trials. In Figure 4(b), we evaluate the computational complexity using TIC and TOC instructions in MATLAB. Figure 4 demonstrates that MPM algorithm and TLS-ESPRIT algorithm have similar RMSE performance under medium and high SNR. However, MPM algorithm has less computational complexity compared with TLS-ESPRIT algorithm. The computation load of TLS-ESPRIT mainly relies on estimating the covariance matrix $\mathbf{R}_{\text{XX}} \in \mathbb{C}^{2(K-1) \times 2(K-1)}$ and performing eigenvalue decomposition for three times, while MPM algorithm avoids the covariance matrix estimation, whose computation load mainly relies on the calculation of propagator \mathbf{P} and an eigenvalue decomposition.

5.2. 3D Position Computation Results. In Figure 5, we assume that $M = 7$ anchor nodes are arranged in a $2 \text{ m} \times 2 \text{ m} \times 2 \text{ m}$ space. Among them, a main anchor node is in the center of the cube, the coordinate of which is (0, 0, 0). The coordinates of the other six anchor nodes are (-1, 0, 0), (0, 1, 0), (0, 0, 1), (-1, 0, 0), (0, -1, 0), and (0, 0, -1), respectively. Multiple unknown nodes are randomly generated within the space. Assume that UWB signal is sent from an unknown node to an anchor node through $L = 2$ paths. SNR = 0 dB. At first, we can obtain $\tau_{\text{TOA}0} \sim \tau_{\text{TOA}6}$ using MPM-based estimation algorithm, in which $Q = 100$. $K = 20$. $T = 1$ ns. Then, the

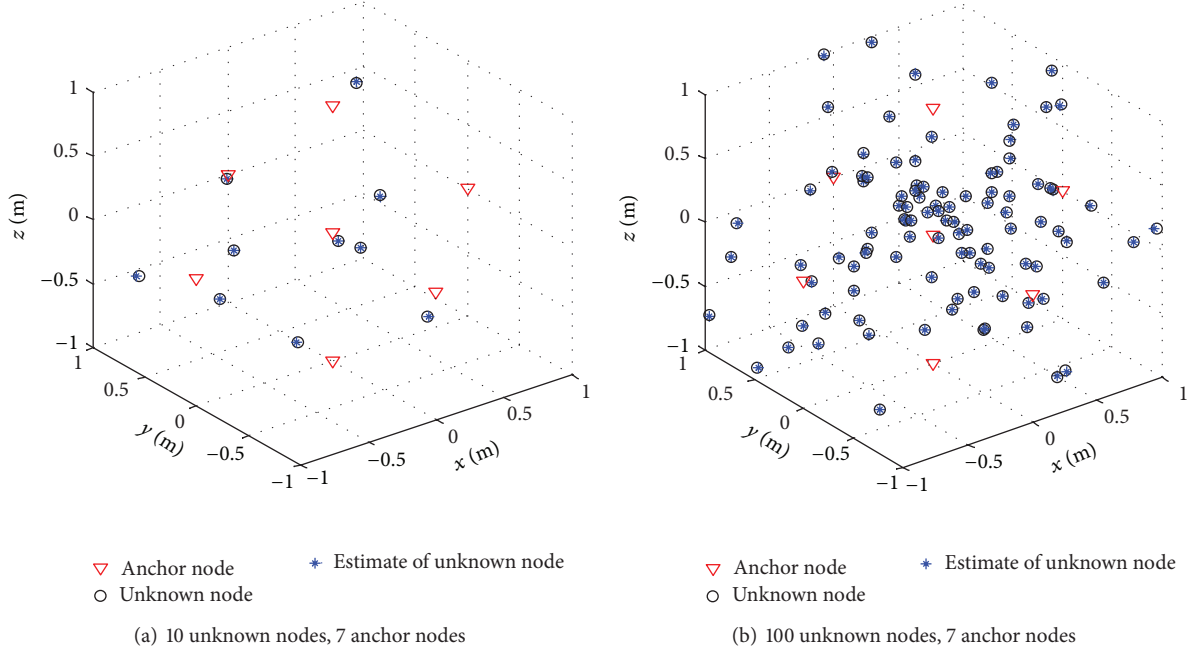


FIGURE 5: Node position computation result.

positions of multiple unknown nodes can be calculated using the marriage algorithm of 3D Chan/Taylor location.

The results of 3D position computation of 10 or 100 unknown nodes are demonstrated in Figures 5(a) and 5(b), respectively. The results show that the coordinates of multiple unknown nodes can be effectively estimated with high accuracy, even with low density of anchor nodes.

5.3. Accuracy of the Proposed Algorithm. We investigate the localization accuracy and robustness of the proposed algorithm by simulation. The node position error can be calculated by

Position Error

$$= \sqrt{\frac{1}{3N} \sum_{n=1}^N ((\hat{x}_n - x)^2 + (\hat{y}_n - y)^2 + (\hat{z}_n - z)^2)}, \quad (33)$$

where N is the number of unknown nodes and $(\hat{x}_n, \hat{y}_n, \hat{z}_n)$ is the coordinate estimate of (x_n, y_n, z_n) for the n th unknown node. 10 unknown nodes are randomly generated in the space. When SNR = 0 dB, the performance of node position error versus the number of anchor nodes is shown in Figure 6, in which the number of anchor nodes varies from 5 to 8. The simulation result from Figure 6 indicates that the accuracy is promoted with the increase of the number of anchor nodes.

Furthermore, the performance of the proposed algorithm is compared with the matrix pencil based localization algorithm in [12] and the previously proposed localization algorithm in [15], as shown in Figure 7. The simulation results reveal that the performance of the proposed algorithm

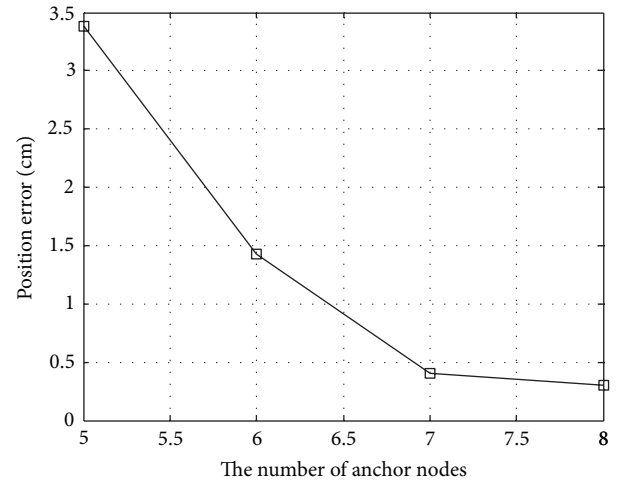


FIGURE 6: Position error versus the number of anchor nodes (SNR = 0 dB).

outperforms the other algorithms. By employing the MPM-based time delay estimation algorithm, the TOA measurement accuracy of our method can be greatly improved compared with matrix pencil based TOA measurement algorithm in [12]. In addition, by the use of the marriage of 3D Chan/Taylor location, the proposed method has better robustness in low SNR compared with the previous algorithm in [15].

6. Conclusion

In this paper, we propose a fast 3D node localization algorithm in multipath for UWB wireless sensor networks. It

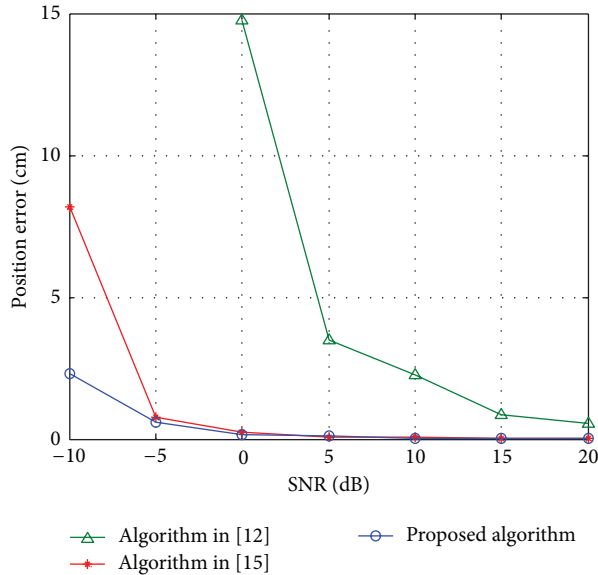


FIGURE 7: The comparison of localization accuracy (7 anchor nodes).

utilizes MPM-based multipath time delay estimation and the marriage of 3D Chan/Taylor location. Compared with the traditional range-based methods, our method has greatly reduced the computational complexity and enhanced the robustness and localization accuracy in multipath and noise environment. The proposed algorithm has key superiorities in fast executing, high accuracy in multipath, and low SNR, which is applicable for node localization in 3D space.

Conflict of Interests

The authors declare that there is no conflict of interests regarding the publication of this paper.

Acknowledgments

The research is supported by the National Natural Science Foundations of China (61071140 and 61371158) and the Jilin Province Natural Science Foundations (201215014).

References

- [1] L. Cheng, C. Wu, Y. Zhang, H. Wu, M. Li, and C. Maple, "A survey of localization in wireless sensor network," *International Journal of Distributed Sensor Networks*, vol. 2012, Article ID 962523, 12 pages, 2012.
- [2] H. Qu, G. Hou, Y. Guo, N. Wang, and Z. Guo, "Localization with single stationary anchor for mobile node in wireless sensor networks," *International Journal of Distributed Sensor Networks*, vol. 2013, Article ID 212806, 11 pages, 2013.
- [3] S.-H. Hong, B.-K. Kim, and D.-S. Eom, "Localization algorithm in wireless sensor networks with network mobility," *IEEE Transactions on Consumer Electronics*, vol. 55, no. 4, pp. 1921–1928, 2009.
- [4] Y.-Y. Cheng and Y.-Y. Lin, "A new received signal strength based location estimation scheme for wireless sensor network," *IEEE Transactions on Consumer Electronics*, vol. 55, no. 3, pp. 1295–1299, 2009.
- [5] E. Kim, S. Lee, C. Kim, and K. Kim, "Mobile beacon-based 3D-localization with multidimensional scaling in large sensor networks," *IEEE Communications Letters*, vol. 14, no. 7, pp. 647–649, 2010.
- [6] M. T. Isik and O. B. Akan, "A three dimensional localization algorithm for underwater acoustic sensor networks," *IEEE Transactions on Wireless Communications*, vol. 8, no. 9, pp. 4457–4463, 2009.
- [7] C.-D. Wann and S.-H. Hsu, "Estimation and analysis of signal arrival time for UWB systems," in *Proceedings of the IEEE 60th Vehicular Technology Conference*, vol. 5, pp. 3560–3564, September 2004.
- [8] M.-A. Pallas and G. Jourdain, "Active high resolution time delay estimation for large BT signals," *IEEE Transactions on Signal Processing*, vol. 39, no. 4, pp. 781–788, 1991.
- [9] L. Dumont, M. Fattouche, and G. Morrison, "Super-resolution of multipath channels in a spread spectrum location system," *Electronics Letters*, vol. 30, no. 19, pp. 1583–1586, 1994.
- [10] H. Saarnisaari, "TLS-ESPRIT in a time delay estimation," in *Proceedings of the 47th IEEE Vehicular Technology Conference*, vol. 3, pp. 1619–1623, May 1997.
- [11] N. Dharamdial, R. S. Adve, and R. Farha, "Multipath Delay Estimation using Matrix Pencil," in *Proceedings of the IEEE Wireless Communications and Networking Conference*, vol. 1, pp. 632–635, 2003.
- [12] C. Liu, H. Jiang, and D. L. Zeng, "Unitary matrix pencil algorithm for range-based 3d localization of wireless sensor network nodes," *Journal of Networks*, vol. 7, no. 9, pp. 1384–1390, 2012.
- [13] S. Marcos, A. Marsal, and M. Benidir, "The propagator method for source bearing estimation," *Signal Processing*, vol. 42, no. 2, pp. 121–138, 1995.
- [14] H. Jiang, F. Cao, and R. Ding, "Propagator method-based TOA estimation for UWB indoor environment in the presence of correlated fading amplitudes," in *Proceedings of the 4th IEEE International Conference on Circuits and Systems for Communications (ICCSC '08)*, pp. 535–538, May 2008.
- [15] H. Jiang, Y. Zhang, H. Cui, and C. Liu, "Fast three-dimensional node localization in UWB wireless sensor network using propagator method (digest of technical papers)," in *Proceedings of the IEEE International Conference on Consumer Electronics (ICCE '13)*, pp. 629–630, January 2013.
- [16] Y. T. Chan and K. C. Ho, "Simple and efficient estimator for hyperbolic location," *IEEE Transactions on Signal Processing*, vol. 42, no. 8, pp. 1905–1915, 1994.
- [17] W. H. Foy, "Position-location solutions by Taylor-series estimation," *IEEE Transactions on Aerospace and Electronic Systems*, vol. 12, no. 2, pp. 187–194, 1976.
- [18] Z. Jian-Wu, Y. Cheng-Lei, T. Bin, and J. Ying-Ying, "Chan location algorithm application in 3-dimension space location," in *Proceedings of the ISECS International Colloquium on Computing, Communication, Control, and Management (CCCM '08)*, pp. 622–625, August 2008.

Research Article

Polarization Reconfigurable Patch Antenna for Wireless Sensor Network Applications

Mustafa Murat Bilgiç and Korkut Yeğın

Department of Electrical and Electronics Engineering, Yeditepe University, 34755 Istanbul, Turkey

Correspondence should be addressed to Mustafa Murat Bilgiç; mustafamuratbilgic@gmail.com

Received 3 June 2013; Accepted 9 October 2013

Academic Editor: Erdal Cayirci

Copyright © 2013 M. M. Bilgiç and K. Yeğın. This is an open access article distributed under the Creative Commons Attribution License, which permits unrestricted use, distribution, and reproduction in any medium, provided the original work is properly cited.

Polarization reconfigurable microstrip patch antenna is presented for 2.4–2.5 GHz wireless sensor network and WLAN applications. Dual feed degenerate mode patch is used as the starting point for circular polarization and L-shaped islands which can be connected or disconnected to the main patch via RF switches are placed around the patch. When L-shape structure is connected, the patch radiates in linear polarization modes with either vertical or horizontal polarization depending on the feed being used. When RF switches are not biased, the antenna is in circular polarization mode. Full wave simulations and measurements were carried out to validate the design.

1. Introduction

Polarization reconfigurable antennas are becoming increasingly popular due to ever increasing wireless applications, especially at 2.4 GHz ISM band. Different polarizations on the same antenna offer key advantages in multipath fading environments and provide means for multiple-input multiple-output (MIMO) systems. Although polarization agile antenna concept has been around for quite some time [1], switching complexities and symmetry in radiation patterns still present challenges in the design.

The simplest method to achieve multipolarization is to switch perturbation segments of the antenna in an effort to change the antenna's electrical characteristics [2–16]. Usually, PIN diodes or RF MEMS was utilized as switch. Changing circular polarization states of a circularly polarized microstrip antenna can be achieved by employing two separate feeds (one for each polarization) and by simply switching the feeds. However, linear polarization states, in that configuration, would require a hybrid coupler and another set of RF switches, which was not practical. Another drawback of this configuration is to use multiple switches on the feed line which increases the noise figure of the system by at least the insertion loss of the switches used. Among slot coupled or slot reconfigurable shaped antennas, U-shaped slot antenna was

studied for multiple polarizations [17–19]. However, symmetry in beam and electrical characteristics was relatively poor. Another extensively studied reconfigurable antenna shape was E-shaped antenna [3]. These antennas were proposed as wideband polarization agile structures. However, the size of the antenna was much larger than their resonant mode counterparts, and achieving four polarizations was problematic. For instance, in [3], linear polarization in only one state was achieved, and the frequency band was divided into two segments to cover the entire ISM band which makes the antenna impractical for many wireless applications. Varactor diodes loaded antennas were also proposed for frequency agile antennas [20–23]. Limited bandwidth and complex voltage biasing circuitry are prominent limitations of these antennas.

In our study, we took a well-known degenerate mode microstrip patch antenna for circular polarization states and loaded this structure with L-shape parasitic units which could be connected to the degenerate mode by RF switches. When parasitic unit is connected to the main patch, the antenna operates in linear polarization mode. Depending on which feed point is selected, either one of the linear polarization states can be invoked. We also employed chip inductors as RF choke instead of quarter-wave match sections which inevitably distort radiation pattern. Simulation and

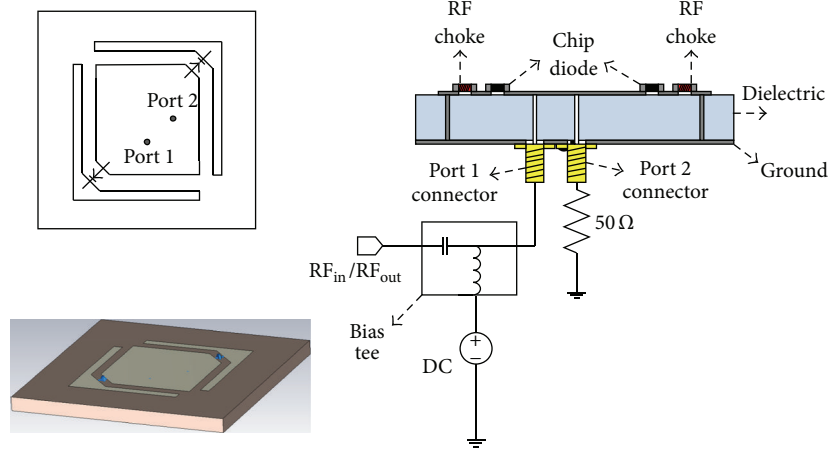
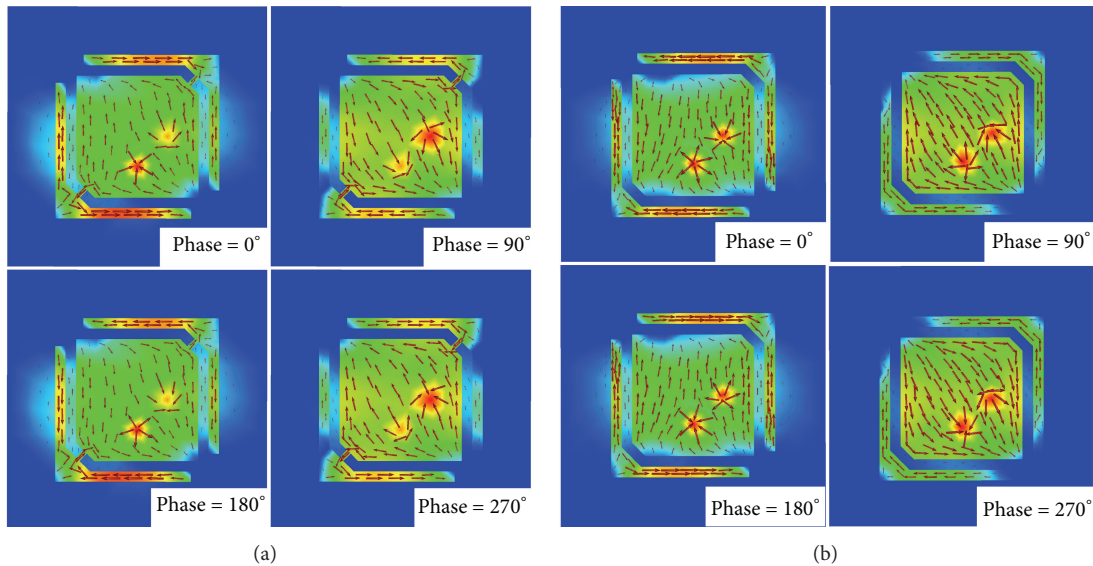


FIGURE 1: Reconfigurable antenna structure.

FIGURE 2: Current distribution on the patch (port 1 is fed, and port 2 is loaded with 50Ω), (a) when diodes are ON and the (b) when diodes are OFF.

measurements indicate all four polarizations using only two RF switches.

2. Reconfigurable Microstrip Antenna

The antenna structure is shown in Figure 1. It is composed of degenerate mode square patch with corners cut and L-shape parasitic elements around the cut corners. RF switches are placed on cut corners of the center of L-shape element. When diodes are OFF, L-shape structure acts parasitic to the main antenna, and when diodes are ON, it is strongly coupled to the main patch. The distance between the parasitic element and the degenerate patch is critical to obtain proper circular and linear polarizations. Feed points determine the sense of polarization, that is, right hand or left hand circular, when diodes are OFF. Likewise, when diodes are ON, vertical or horizontal polarization can be obtained from the feed port.

TABLE 1: Switch states and polarizations.

	Port 1	Port 2
S1 and S2 OFF	LHCP	RHCP
S1 and S2 ON	Linear vertical	Linear horizontal

Polarization states for the switch positions and feed ports are summarized in Table 1.

Layout of the biasing circuitry is very important and often the cause for asymmetry in radiation patterns. Quarter wavelength chokes have been implemented in past designs, but we observed that it distorted (even slightly tilt) the main radiation pattern. Hence, we used RF chip inductors as RF chokes. The ground return for the RF choke is implemented via small DC cable around the patch as opposed to via, although it's been simulated with via. In that sense, our

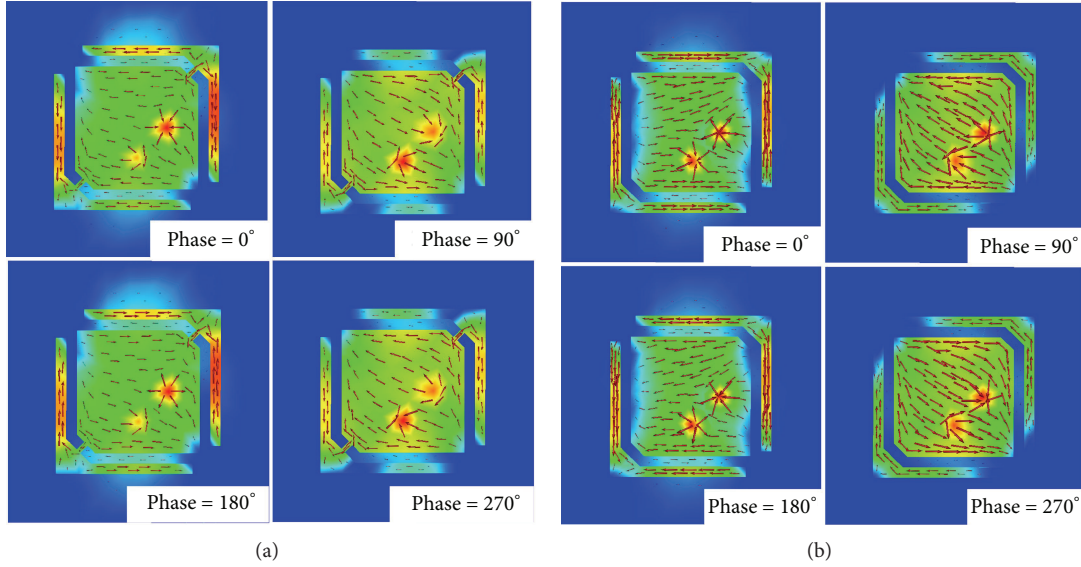


FIGURE 3: Current Distribution on the patch (port 2 is fed, and port 1 is loaded with $50\ \Omega$), (a) when diodes are ON and (b) when diodes are OFF.

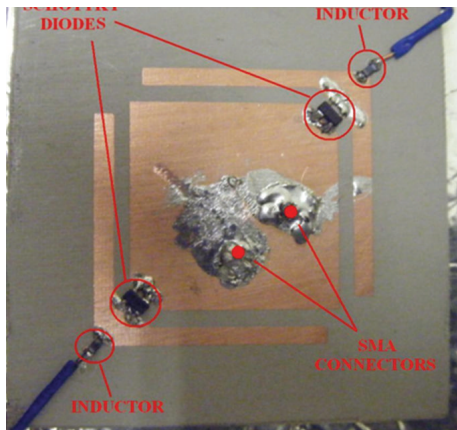


FIGURE 4: Prototype of the reconfigurable antenna.

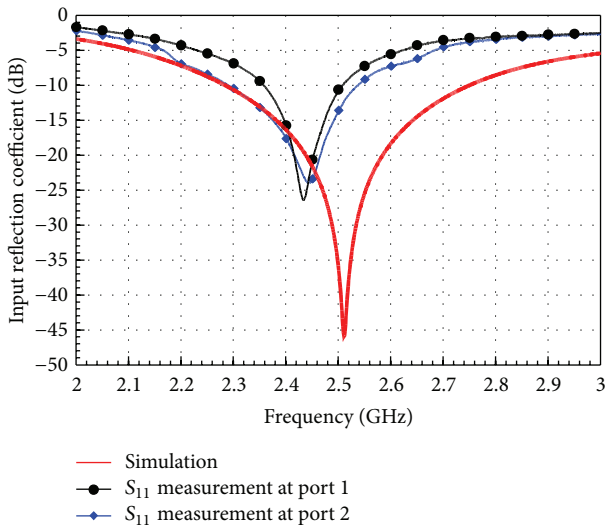


FIGURE 5: Measured and simulated input reflection coefficients when diodes are OFF.

design is different than earlier reconfigurable designs. The DC current through the diode is limited from DC supply with a series resistor.

Current distributions on the patch antenna when it is fed from port 1 or port 2 are shown in Figures 2 and 3, respectively. The symmetry in current distributions is mainly due to preserved symmetry in the antenna design. When diodes are ON, the current distribution on L-shape is stronger and enforces the current distribution on the main patch for linear polarization; that is, 90° phase shift between the alternate corners is not observed.

3. Simulations and Measurements of the Reconfigurable Antenna

Simulations of the antenna are carried out in FEKO, 3D electromagnetics solver. For realization, we used a substrate from Taconic RF65 ($\epsilon_r = 6.5$, $\tan \delta = 0.002$). Substrate thickness is 3.17 mm. We used BAR64 PIN diodes from Infineon Technologies and 0603 SMD components for RF choke inductors from Coilcraft. The prototype is shown in Figure 4. Simulation and measurements of the antenna when diodes are OFF and ON are shown in Figures 5 and 6, respectively.

Although measurements exhibit slight shift in frequency, the match is under -10 dB throughout 2.4–2.5 GHz.

The reconfigurable antenna gains are shown in Figures 7 and 8. They well match with those of standalone patch antenna modes. Cross-polarization levels could be further improved with slight modifications in the L-shape island geometry.

Radiation patterns of the reconfigurable antenna fed from port 1 are illustrated in Figure 9. There is no beam asymmetry or tilt in the patterns due to symmetry in feed structure.

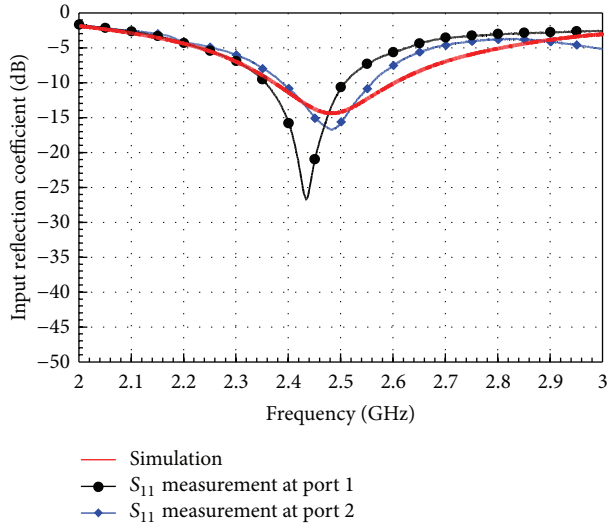


FIGURE 6: Measured and simulated input reflection coefficient when diodes are ON.

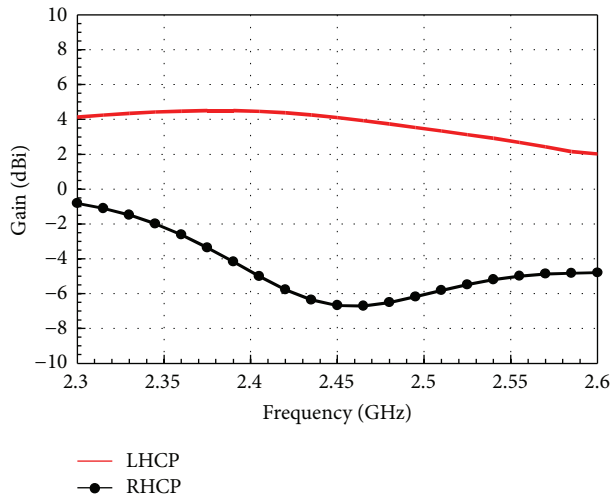


FIGURE 7: Antenna gain when diodes are OFF.

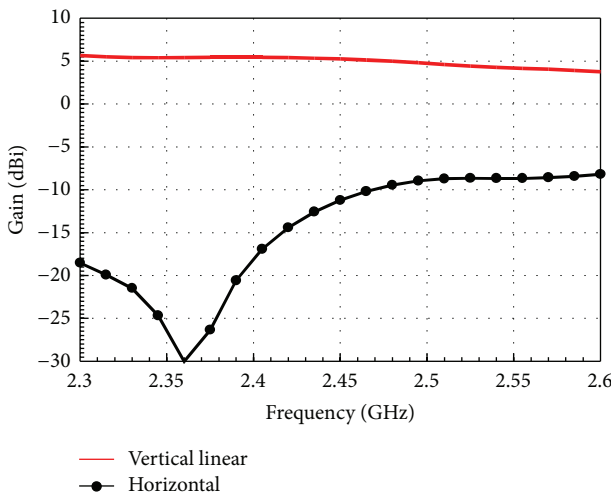


FIGURE 8: Antenna gain when diodes are ON.

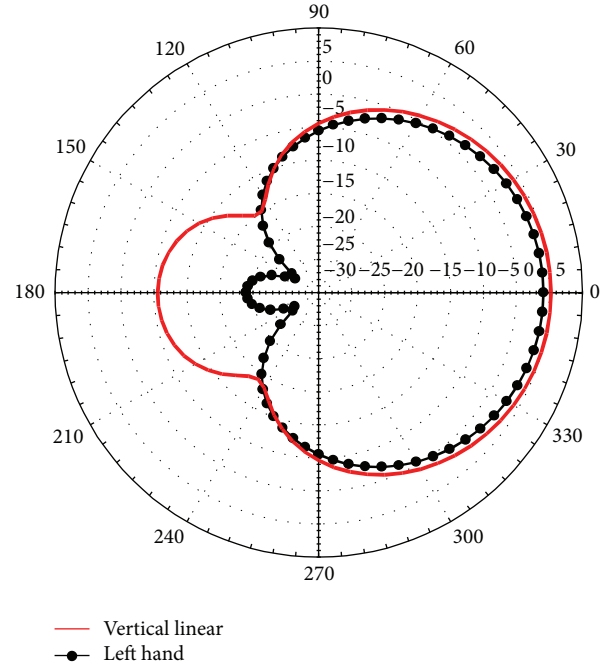


FIGURE 9: Gain patterns of the antenna at 2.45 GHz.

4. Conclusions

A reconfigurable microstrip patch antenna design for WSN applications has been presented. The biasing of the diodes and isolation of RF from DC path are achieved using discrete SMD components. The structure preserves its symmetry for circular and linear polarization modes. All the four polarizations can be achieved by simply switching the feeds and the diodes on the top metallic part. Antenna gain of the reconfigurable antenna is very comparable to its standalone degenerate mode patch for circular polarization and single mode for linear polarization counterparts. The proposed configuration is simple and easy to implement for polarization diversity antennas.

Acknowledgment

The authors thank EMSS FEKO, GmbH, Germany, for providing extended software license.

References

- [1] S. Gao, A. Sambell, and S. S. Zhong, "Polarization-agile antennas," *IEEE Antennas and Propagation Magazine*, vol. 48, no. 3, pp. 28–37, 2006.
- [2] S. X. Cao, X. X. Yang, B. Gong, and B. C. Shao, "A reconfigurable microstrip antenna with agile polarization using diode switches," in *Proceedings of the IEEE International Symposium on Antennas and Propagation (APSURSI '11)*, pp. 1566–1569, July 2011.
- [3] A. Khidre, K. Lee, F. Yang, and A. Z. Elsherbeni, "Circular polarization reconfigurable wideband E-shaped patch antenna for wireless applications," *IEEE Transactions on Antennas and Propagation*, vol. 61, no. 2, pp. 960–964, 2013.

- [4] X. X. Yang, B. C. Shao, F. Yang, A. Z. Elsherbeni, and B. Gong, "A polarization reconfigurable patch antenna with loop slots on the ground plane," *IEEE Antennas and Wireless Propagation Letters*, vol. 11, pp. 69–72, 2012.
- [5] D. H. Schaubert, F. G. Farrar, A. Sindoris, and S. T. Hayes, "Microstrip antennas with frequency agility and polarization diversity," *IEEE Transactions on Antennas and Propagation*, vol. 29, no. 1, pp. 118–123, 1981.
- [6] S. S. L. Yang and K. M. Luk, "A wideband circularly polarized reconfigurable patch antenna excited by L-shaped probes," in *Proceedings of the Asia-Pacific Microwave Conference (APMC '06)*, pp. 81–84, December 2006.
- [7] B. Z. Wang, S. Xiao, and J. Wang, "Reconfigurable patch-antenna design for wideband wireless communication systems," *IET Microwaves, Antennas and Propagation*, vol. 1, no. 2, pp. 414–419, 2007.
- [8] Y. J. Sung, "Reconfigurable patch antenna for polarization diversity," *IEEE Transactions on Antennas and Propagation*, vol. 56, no. 9, pp. 3053–3054, 2008.
- [9] F. Yang and Y. Rahmat-Samii, "A reconfigurable patch antenna using switchable slots for circular polarization diversity," *IEEE Microwave and Wireless Components Letters*, vol. 12, no. 3, pp. 96–98, 2002.
- [10] Z. Faiza, M. T. Ali, S. Subahir, and A. L. Yusof, "Design of reconfigurable dual-band E-shaped microstrip patch antenna," in *Proceedings of the International Conference on Computer and Communication Engineering*, pp. 113–117, July 2012.
- [11] J. S. Row and M. C. Chan, "Reconfigurable circularly-polarized patch antenna with conical beam," *IEEE Transactions on Antennas and Propagation*, vol. 58, no. 8, pp. 2753–2757, 2010.
- [12] P. Tilanthe and P. C. Sharma, "A pattern reconfigurable patch antenna with square ring shaped parasite radiator," in *Proceedings of the Applied Electromagnetics Conference (AEMC '09)*, pp. 1–4, December 2009.
- [13] R. H. Chen and J. S. Row, "Single-fed microstrip patch antenna with switchable polarization," *IEEE Transactions on Antennas and Propagation*, vol. 56, no. 4, pp. 922–926, 2008.
- [14] S. L. S. Yang and K. M. Luk, "A wideband L-probes fed circularly-polarized reconfigurable microstrip patch antenna," *IEEE Transactions on Antennas and Propagation*, vol. 56, no. 2, pp. 581–584, 2008.
- [15] S. Methfessel and L. P. Schmidt, "Design and measurement of a wideband aperture-coupled and polarization-agile stacked-patch antenna-array for monopulse radar applications," in *Proceedings of the 3rd European Conference on Antennas and Propagation (EuCAP '09)*, pp. 1350–1353, March 2009.
- [16] S. Raman and G. M. Rebeiz, "Single- and dual-polarized millimeter-wave slot-ring antennas," *IEEE Transactions on Antennas and Propagation*, vol. 44, no. 11, pp. 1438–1444, 1996.
- [17] S. L. S. Yang, A. A. Kishk, and K. F. Lee, "Frequency reconfigurable U-slot microstrip patch antenna," *IEEE Antennas and Wireless Propagation Letters*, vol. 7, pp. 127–129, 2008.
- [18] S. J. Ha and C. W. Jung, "Reconfigurable beam steering using a microstrip patch antenna with a U-slot for wearable fabric applications," *IEEE Antennas and Wireless Propagation Letters*, vol. 10, pp. 1228–1231, 2011.
- [19] P. Y. Qin, A. R. Weily, Y. J. Guo, and C. H. Liang, "Polarization reconfigurable U-slot patch antenna," *IEEE Transactions on Antennas and Propagation*, vol. 58, no. 10, pp. 3383–3388, 2010.
- [20] F. Ferrero, C. Luxey, R. Staraj, G. Jacquemod, M. Yedlin, and V. Fusco, "A novel quad-polarization agile patch antenna," *IEEE Transactions on Antennas and Propagation*, vol. 57, no. 5, pp. 1562–1566, 2009.
- [21] G. León, S. ver Hoeye, M. Fernández, C. V. Vázquez, L. F. Herrán, and F. Las Heras, "Novel polarization agile microstrip antenna," in *Proceedings of the IEEE Antennas and Propagation Society International Symposium*, pp. 1–4, July 2008.
- [22] P. M. Haskins and J. S. Dahele, "Varactor-diode loaded passive polarisation-agile patch antenna," *Electronics Letters*, vol. 30, no. 13, pp. 1074–1075, 1994.
- [23] P. M. Haskins and J. S. Dahele, "Four-element varactor diode loaded polarisation-agile microstrip antenna array," *Electronics Letters*, vol. 33, no. 14, pp. 1186–1187, 1997.

Research Article

Footstep and Vehicle Detection Using Seismic Sensors in Wireless Sensor Network: Field Tests

Gökhan Koç^{1,2} and Korkut Yegin^{1,2}

¹ KoçSistem Information Communication Services Inc., Istanbul 34700, Turkey

² Department of Electrical and Electronics Engineering, Yeditepe University, Istanbul 34755, Turkey

Correspondence should be addressed to Gökhan Koç; gokhan.koc@kocsistem.com.tr

Received 15 May 2013; Accepted 4 September 2013

Academic Editor: Adnan Kavak

Copyright © 2013 G. Koç and K. Yegin. This is an open access article distributed under the Creative Commons Attribution License, which permits unrestricted use, distribution, and reproduction in any medium, provided the original work is properly cited.

Extensive field tests were carried out to assess the performance of adaptive thresholds algorithm for footstep and vehicle detection using seismic sensors. Each seismic sensor unit is equipped with wireless sensor node to communicate critical data to sensor gateway. Results from 92 different test configurations were analyzed in terms of detection and classification. Hit and false alarm rates of classification algorithm were formed, and detection ranges were determined based on these results. Amplification values of low-intensity seismic data were also taken into account in the analysis. Algorithm-dependent constants such as adaptive thresholds sample sizes were examined for performance. Detection and classification of seismic signals due to footstep, rain, or vehicle were successfully performed.

1. Introduction

Seismic sensors are invaluable parts of security systems that focus on perimeter or compound security. Footstep detection is the foremost application of these sensors [1–7]. Fusion of different sensors has also been considered for the same task [8, 9]. Many detection algorithms have been proposed in the past, but some of them place too much burden on computational resources and some of them are simply too complex to be implemented on a wireless sensor network, and yet some of them lack field tests. Field tests compromise of footsteps and vehicles at different ranges of the sensors.

Another critical aspect of footstep detection is the amount of analog signal gain that is applied to seismic data. Low-intensity seismic data require large amounts of amplification before being digitized. On one hand, high amplification is desired for increased range at the expense of increased noise level. On the other hand, low amplification is ideal for suppressing and identifying noise but has limited application range [10, 11]. Any signal processing algorithm must pay attention to amplification level as well as algorithm-dependent variables. In this study, we also study the impact of signal amplification on detection performance by analyzing data with

different amplification values. Seismic data after being processed at the node, has been transferred to other wireless nodes or directly to the gateway to signal alarm conditions. Wireless sensor network nodes, illustrated in Figure 1, were specifically developed for this purpose, utilizing Texas Instruments transceiver and microcontroller family.

2. Test Setup

Field tests were performed at Yeditepe University, and test conditions are summarized in Table 1. Test site is shown in Figure 2. Two students with different body weights were chosen for footstep detection. Footstep, vehicle, and combined footstep-vehicle tests were used to test the detection algorithm under various signal amplification conditions.

3. Detection Probability and Classification Performance

The detection algorithm was explained previously in [10]. Flowchart of the algorithm is given in Figure 2. The algorithm utilizes slow adaptive threshold (SAT) to identify ambient dynamic noise and quick adaptive threshold (QAT) to detect

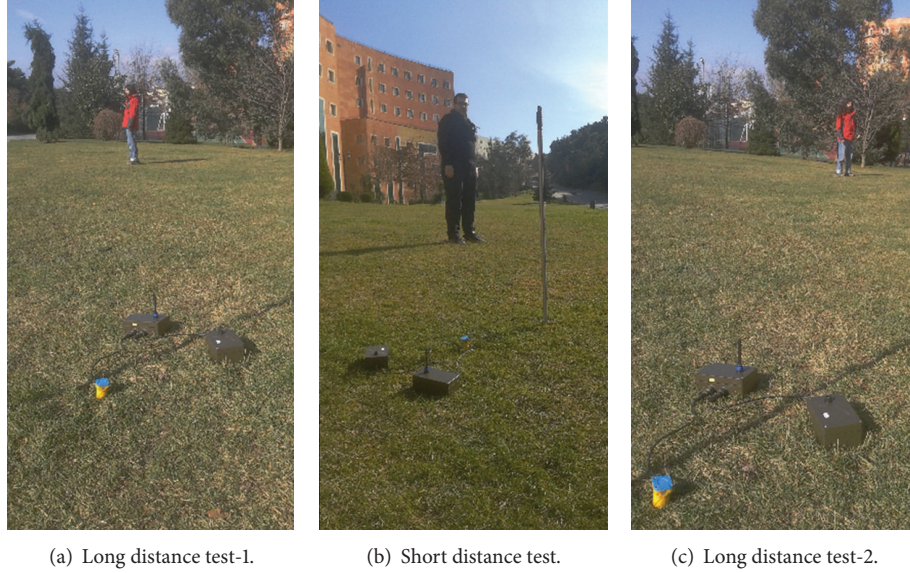


FIGURE 1: Pictures of test setup.

TABLE 1: Field test conditions.

Test conditions	
Test location	Yeditepe University Kayışdağı campus
Weather condition	Dry
Air temperature	9°C
Soil moisture status	Wet
Sampling frequency	250 sample/second
Amplification gain	Different in each Test
Vehicle	Kia Rio GSL EX 1.4
Person A weight	60 kg
Person B weight	120 kg

TABLE 2: Chart for detection performance.

	Detection present	Detection absent
Signal present	True detection (hit)	Missed detection (missed)
Signal absent	False detection (false alarm)	Correct rejection in detection

any disturbance in sensor readings. For field tests, first, noise-only data were collected with different gain values. Signal processing algorithm is expected not to produce any alarm to these noise-only data. Then, a large number of footstep tests were executed to assess the performance of the algorithm. Afterwards, vehicle tests were evaluated, and lastly, vehicle and footstep combined condition were assessed.

First, we define “True Detection”, “False Detection”, “Missed Detection”, and “Correct Rejection” according to Table 2. “true detection” means that the signal type is detected correctly. “Missed detection” refers to the condition that the present signal is not detected. “False detection” refers to incorrect detection; that is, if a vehicle signal is detected in

TABLE 3: Chart for classification performance.

	Classification present	Classification absent
Signal present	True classification (hit)	Missed classification (missed)
Signal absent	False classification (false alarm)	Correct rejection in classification

TABLE 4: Noise-only data (no disturbance).

Gain	Vibration type detection			Classification		
	Footstep	Rain	Vehicle	Footstep	Rain	Vehicle
1000	0	0	0	—	—	—
2500	0	0	0	—	—	—
3500	0	0	0	—	—	—
5000	0	0	0	—	—	—
6500	0	0	0	—	—	—
7500	0	0	0	—	—	—

footstep test, this detection is called “false detection.” “Correct rejection” condition occurs only if there is no signal and no detection.

Since detection is different than alarm, a similar table is formed for alarm conditions in Table 3.

“True Classification” means intruder type is classified correctly. “Missed classification” means intruder type is not classified. “False classification” means signal type is classified incorrectly; for example, if a vehicle signal was classified in footstep test, this classification is called “false classification.” “Correct Rejection in Classification” condition occurs only if there is neither intruder nor any alarm.

Specifying hits and false alarms is sufficient as the others (miss and correct rejection) can be easily extracted; that is, $probability(\text{Hit})$ equals to $probability(\text{Miss})$.

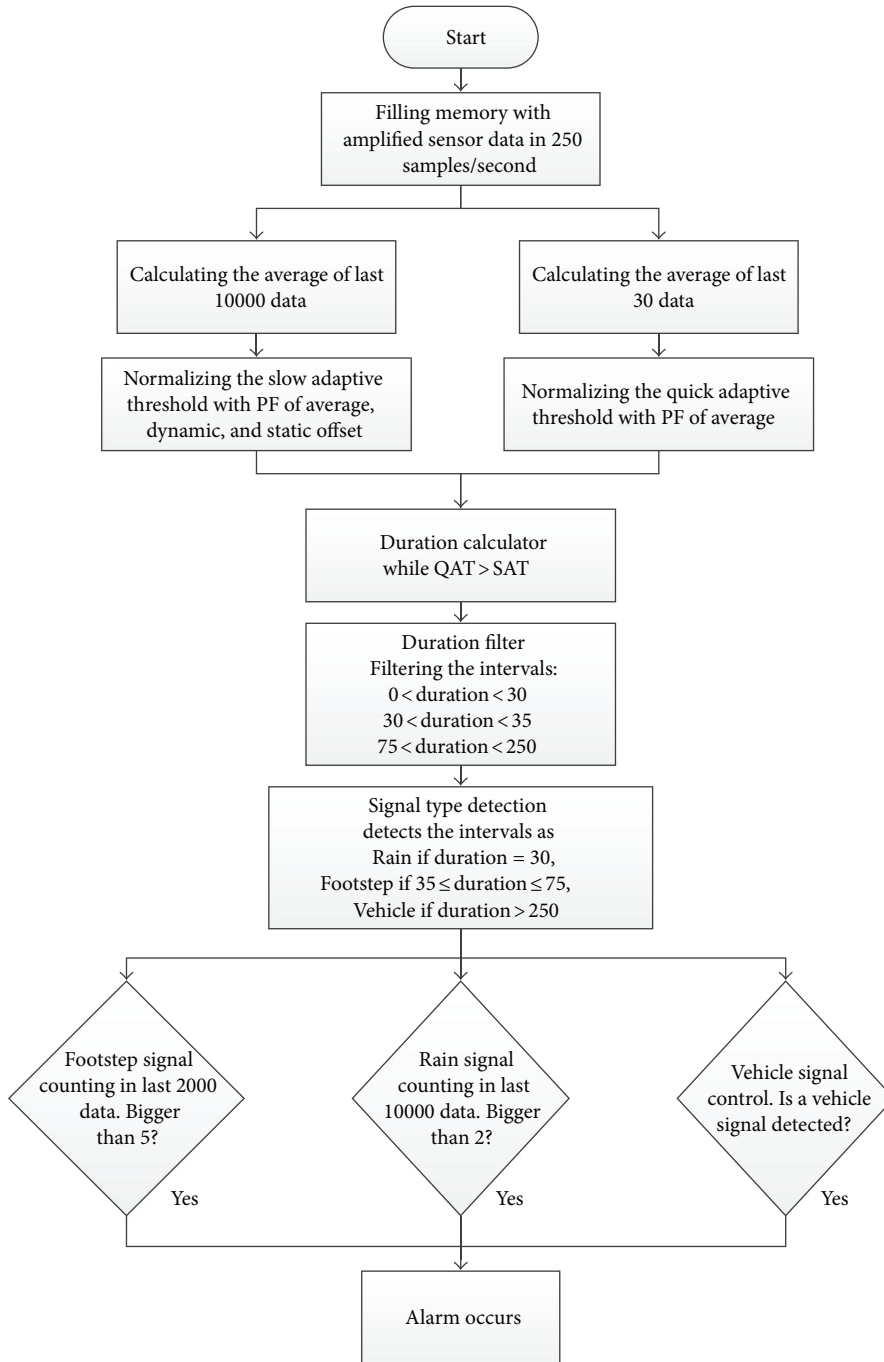


FIGURE 2: The flowchart of the detection and alarm algorithm.

3.1. *Noise-Only Tests.* In noise-only tests, ambient environment is recorded and processed with 20 different gain values in the absence of any movement. Detection and classification results are presented in Table 4. A large range of gain values were tested. Gain values greater than 7.5 K were not tested as noise levels reach full ADC swing.

As it is seen in the Table 4, the signal processing algorithm did not produce any alarm or any vibration detection in noise-only condition at all amplification values.

3.2. *Footstep Tests.* Nine circles concentric to the seismic sensor were traversed by two different persons. The test setup is illustrated in Figure 3. In each test, 60 footsteps were taken (for larger radius circles, only some portion of the circle is traversed.). A total of 72 tests were formed according to Table 5 where combinations of different persons with different amplification values on test circles were evaluated.

The classification result was “true” when only footstep alarm was generated, “false” if rain or vehicle alarm were

TABLE 5: Footstep test configurations.

Distance	Person A				Person B			
	Gain 1k	Gain 2.5k	Gain 5k	Gain 7.5k	Gain 1k	Gain 2.5k	Gain 5k	Gain 7.5k
4 m	A-1k-4 m	A-2.5k-4 m	A-5k-4 m	A-7.5k-4 m	B-1k-4 m	B-2.5k-4 m	B-5k-4 m	B-7.5k-4 m
6 m	A-1k-6 m	A-2.5k-6 m	A-5k-6 m	A-7.5k-6 m	B-1k-6 m	B-2.5k-6 m	B-5k-6 m	B-7.5k-6 m
8 m	A-1k-8 m	A-2.5k-8 m	A-5k-8 m	A-7.5k-8 m	B-1k-8 m	B-2.5k-8 m	B-5k-8 m	B-7.5k-8 m
10 m	A-1k-10 m	A-2.5k-10 m	A-5k-10 m	A-7.5k-10 m	B-1k-10 m	B-2.5k-10 m	B-5k-10 m	B-7.5k-10 m
12 m	A-1k-12 m	A-2.5k-12 m	A-5k-12 m	A-7.5k-12 m	B-1k-12 m	B-2.5k-12 m	B-5k-12 m	B-7.5k-12 m
14 m	A-1k-14 m	A-2.5k-14 m	A-5k-14 m	A-7.5k-14 m	B-1k-14 m	B-2.5k-14 m	B-5k-14 m	B-7.5k-14 m
16 m	A-1k-16 m	A-2.5k-16 m	A-5k-16 m	A-7.5k-16 m	B-1k-16 m	B-2.5k-16 m	B-5k-16 m	B-7.5k-16 m
18 m	A-1k-18 m	A-2.5k-18 m	A-5k-18 m	A-7.5k-18 m	B-1k-18 m	B-2.5k-18 m	B-5k-18 m	B-7.5k-18 m
20 m	A-1k-20 m	A-2.5k-20 m	A-5k-20 m	A-7.5k-20 m	B-1k-20 m	B-2.5k-20 m	B-5k-20 m	B-7.5k-20 m

TABLE 6: Footstep classification with 5 K gain.

Distance (m)	Footstep classification results with 5 K gain							
	Person A				Person B			
	Footstep	Rain	Vehicle	Result	Footstep	Rain	Vehicle	Result
4	+	-	-	True	+	-	+	False
6	+	-	-	True	+	-	-	True
8	+	-	-	True	+	-	-	True
10	+	-	-	True	+	-	-	True
12	-	-	-	Missed	+	-	-	True
14	-	-	-	Missed	+	-	-	True
16	-	-	-	Missed	+	-	-	True
18	-	-	-	Missed	+	-	+	False
20	-	-	-	Missed	+	+	-	False

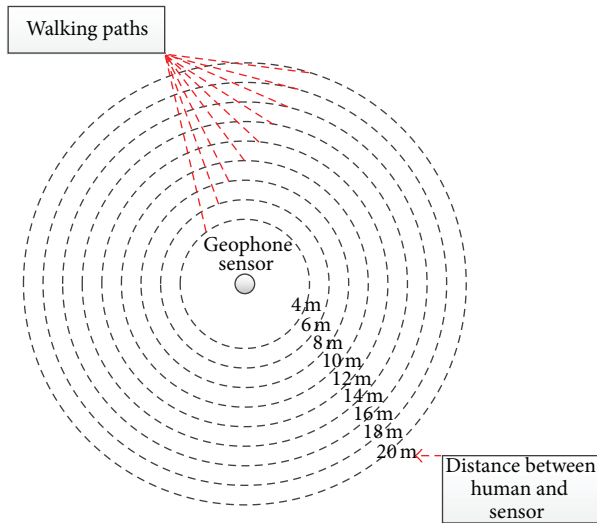


FIGURE 3: Footstep test setup.

triggered, and “miss” if no alarm occurred. The probability of each classification results according to different conditions was evaluated by using data from both persons. The results are presented in Figures 4 and 5 and Tables 6 and 7.

Classification performance can vary depending on gain and range. For >90% true classification rate and less than 10%

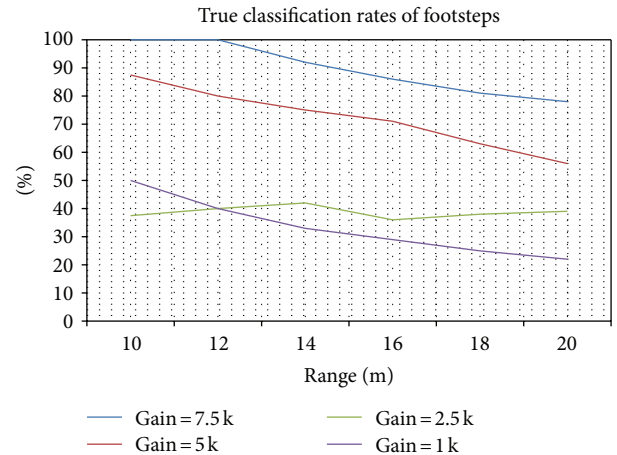


FIGURE 4: True classification rates of footsteps with different gain and range values.

false classification, 7.5 K amplification at 14 m provides best results. However, 7.5 K is still too large for vehicle tests, and if target detection range is lowered to less than 10 m, 5 K gain is as good as 7.5 K gain.

3.3. *Vehicle Tests.* Test setup for vehicle tests is shown in Figure 6. Vehicle tests were executed on a straight line with

TABLE 7: Footstep classification with 7.5 K gain.

Distance (m)	Footstep classification results with 7.5 K gain							
	Person A				Person B			
	Footstep	Rain	Vehicle	Result	Footstep	Rain	Vehicle	Result
4	+	-	-	True	+	-	-	True
6	+	-	-	True	+	-	-	True
8	+	-	-	True	+	-	-	True
10	+	-	-	True	+	-	-	True
12	+	-	-	True	+	-	-	True
14	+	+	-	False	+	-	-	True
16	+	-	-	True	+	+	-	False
18	-	-	-	Missed	+	-	-	True
20	-	-	-	Missed	+	-	-	True

TABLE 8: Vehicle tests configurations.

Distance (m)	Gain = 1 K		Gain = 5 K	
	Speed = 20 km/h	Speed = 40 km/h	Speed = 20 km/h	Speed = 40 km/h
10	G1000S20D10	G1000S40D10	G5000S20D10	G5000S40D10
20	G1000S20D20	G1000S40D20	G5000S20D20	G5000S40D20
30	G1000S20D30	G1000S40D30	G5000S20D30	G5000S40D30

TABLE 9: Vehicle classification with different test parameters.

Test ID	Vibration type detection			Classification
	Footstep	Rain	Vehicle	
G1000S20D10	3	1	1	True
G1000S20D20	0	0	0	Missed
G1000S20D30	0	0	0	Missed
G1000S40D10	1	2	1	True
G1000S40D20	3	0	0	Missed
G1000S40D30	1	0	0	Missed
G5000S20D10	8	0	1	True
G5000S20D20	9	0	1	True
G5000S20D30	0	0	0	Missed
G5000S40D10	3	2	1	True
G5000S40D20	4	2	1	True
G5000S40D30	1	1	0	Missed

varying distances from the geophone sensor, 10 meters, 20 meters, and 30 meters. All lines are passed with two different vehicle speeds, 20 km/hr and 40 km/hr. Test IDs were formed as GXXXXSYDZZ, where XXXX represents gain amount, YY represents speed, and ZZ represents distance to sensor. Tests were performed with 1 K and 5 K gains. Although 7.5 K gain produced very good results, we did not use that in vehicle tests due to increased noise levels, which in turn degraded the sensitivity of the system. Particular tests, with corresponding test IDs were given in Table 8, were performed.

Summary of the tests are given in Table 9. There were false vibration type detections. However, these false detections were filtered in the classification processes. Only 1 false classification was observed in 12 tests.

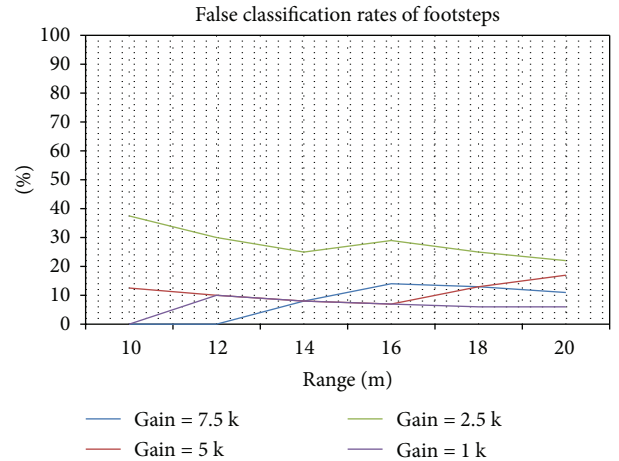


FIGURE 5: False classification rates of footsteps with different gain and range values.

3.4. *Vehicle and Footstep Combined Tests.* The test setup is illustrated in Figure 7. Vehicle with footstep tests were executed on two different lines at the same time. Walking path distance to geophone sensor was 5 meters, and vehicle path distance to sensor is 10 meters. On vehicle path, two different vehicle speeds (20 km/hr and 40 km/hr) were used; all tests were repeated twice.

As before, test ID's were assigned with GXXXXSYTZ where XXXX, YY, and Z represent gain, vehicle speed, and test number, respectively. The tests, all configurations were given in Tables 10 and 8, were performed.

Here, false Alarm was defined as "Rain" alarm, and missed classification was defined as missing any one of

TABLE 10: Vehicle and footstep combined tests.

Test repeat	Gain = 1 K		Gain = 5 K	
	Speed = 20 km/h	Speed = 40 km/h	Speed = 20 km/h	Speed = 40 km/h
First test	G1000S20T1	G1000S40T1	G5000S20T1	G5000S40T1
Second test	G1000S20T2	G1000S40T2	G5000S20T2	G5000S40T2

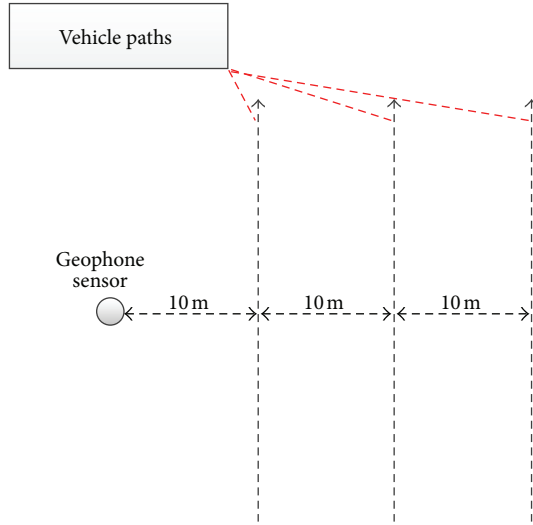


FIGURE 6: Vehicle test paths.

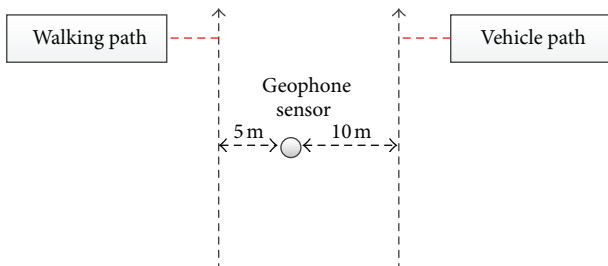


FIGURE 7: Vehicle and footstep combined test configuration.

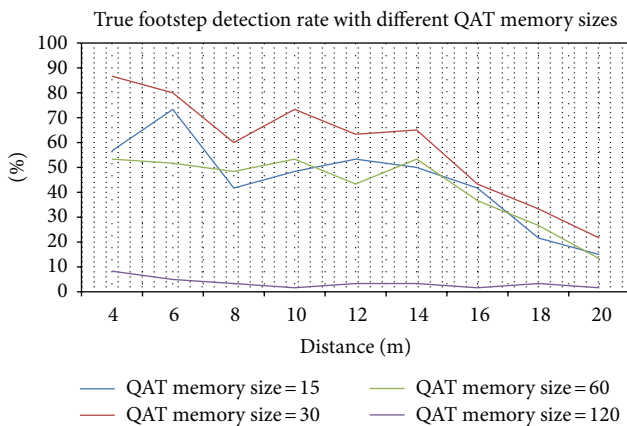


FIGURE 8: True footstep detection rate with different QAT memory sizes.

TABLE 11: Vehicle and footstep classification results.

Test ID	Vibration type detection			Classification
	Footstep	Rain	Vehicle	
G1000S20T1	10	1	1	TRUE
G1000S20T2	8	0	1	TRUE
G1000S40T1	7	0	1	TRUE
G1000S40T2	14	1	1	TRUE
G5000S20T1	9	1	1	TRUE
G5000S20T2	7	1	1	FALSE
G5000S40T1	19	0	1	TRUE
G5000S40T2	11	2	1	TRUE

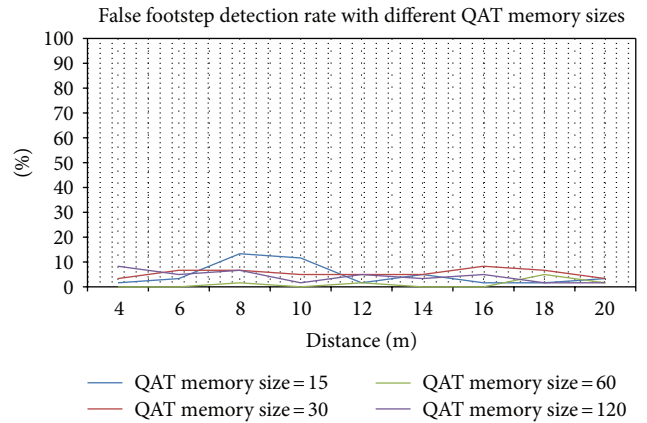


FIGURE 9: False footstep detection rate with different QAT memory sizes.

the two alarms, either vehicle or footstep. Test results were summarized in Table 11.

There were false vibration type detections, but these false detections were filtered in the classification. Only one false classification was observed in eight tests.

4. Algorithm-Dependent Parameters

Detection algorithm heavily relies on QAT and SAT memory sizes, that is, number of samples where moving average is calculated. Thus, we studied detection performance by varying these critical memory sizes. Amplification was set to 5 K for all tests. True, false, and missed detection for various QAT memory sizes as a function of range are shown in Figures 8, 9, and 10. Same analysis was performed for SAT memory sizes and the results are presented in Figures 11, 12, and 13.

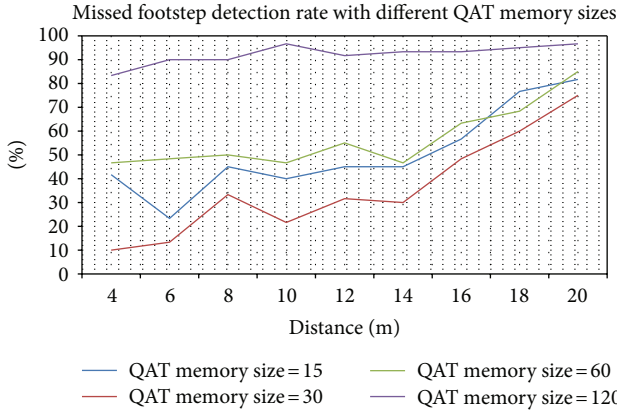


FIGURE 10: Missed footstep detection rate with different QAT memory sizes.

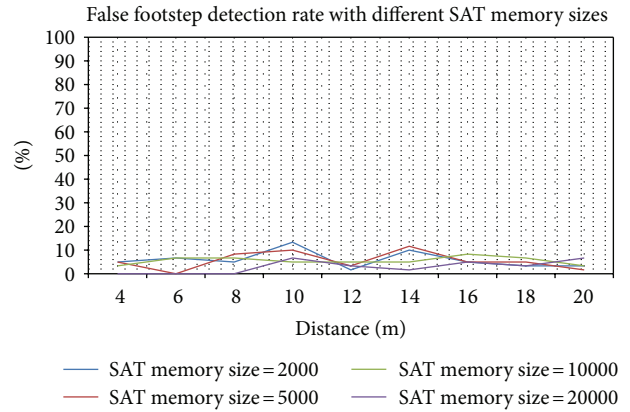


FIGURE 12: False footstep detection rate with different SAT memory sizes.

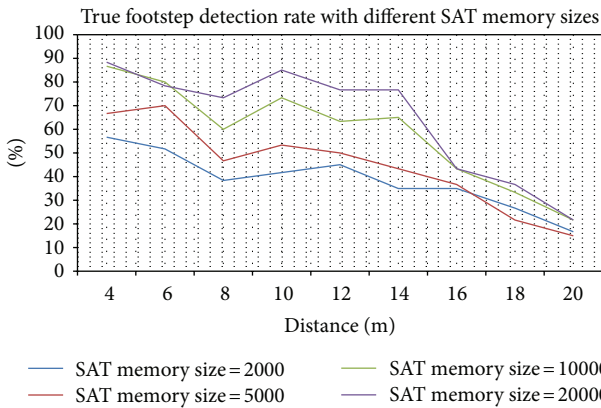


FIGURE 11: True footstep detection rate with different SAT memory sizes.

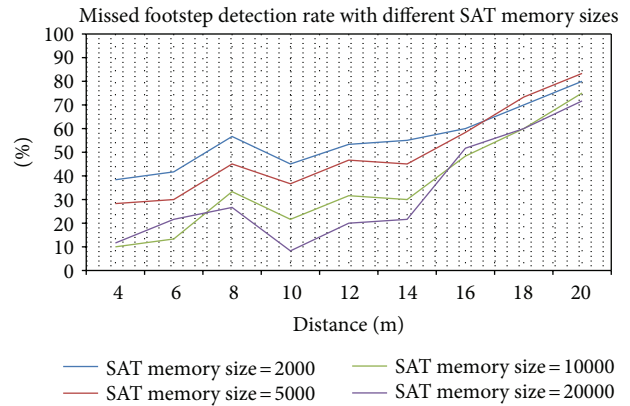


FIGURE 13: Missed footstep detection rate with different SAT memory sizes.

Best performance for true footstep detection was achieved when QAT memory size was 30 samples and SAT memory size was 20000 samples. Lower or higher than 30 samples QAT memory size prevents detection of footsteps due to oscillations in the footstep vibrations. Larger SAT memory sizes provide stability at the intruder movement moments. However, due to memory limitations of WSN, SAT memory size cannot be increased indefinitely.

5. Conclusion

Extensive field tests were performed to assess the performance of adaptive thresholds detection algorithm. Over 92 different test scenarios were performed, and results were evaluated in terms of detection performance. Performance tests also included the amplification amount of seismic sensor signals operating in a wireless sensor network. As higher amplification values lead to better detection range, they also increase noise level which, in turn, increases false alarm classification. For detection range under 10 m, 100% footstep classification with less than 5% false alarm rate was observed with 5 K gain. For detection range less than 15 m, 7.5 K gain produced about 95% hit rate and less than 10% false

classification rate. Although the number of experiments with vehicle tests were limited, 5 K gain was also successful (nearly 68% true detection and no false detection). Algorithm-dependent constants such as QAT and SAT sample sizes were analyzed for best performance, and these values were used in detection and classification.

References

- [1] R. Vera-Rodriguez, J. S. D. Mason, J. Fierrez, and J. Ortega-Garcia, "Analysis of time domain information for footstep recognition," in *Advances in Visual Computing*, vol. 6453 of *Lecture Notes in Computer Science*, pp. 489–498, Springer, New York, NY, USA, 2010.
- [2] L. Peck, J. Gagnon, and J. Lacombe, "Seismic detection of personnel: field trials with REMBASS-II and qual-tron sensors," ERDC/CRREL TR-06-4, 2006.
- [3] M. S. Richman, D. S. Deadrick, R. J. Nation, and S. L. Whitney, "Personnel tracking using seismic sensors," *The International Society for Optics and Photonics*, vol. 4393, pp. 14–21, 2001.
- [4] J. Lacombe, L. Peck, T. Anderson, and D. Fisk, "Seismic detection algorithm and sensor deployment recommendations for perimeter security," *The International Society for Optics and Photonics*, vol. 6231, pp. 1–10, 2006.

- [5] A. Pakhomov and T. Goldburt, "Seismic systems for unconventional target detection and identification," *The International Society for Optics and Photonics*, vol. 6201, pp. 1–12, 2006.
- [6] W. E. Audette, D. B. Kynor, J. C. Wilbur, J. R. Gagne, and L. Peck, "Improved intruder detection using seismic sensors and adaptive noise cancellation," in *Proceedings of the Human, Light Vehicle, and Tunnel Detection Workshop*, pp. 1–14, Hanover, Germany, June 2009.
- [7] L. Peck, J. Lacombe, and T. Anderson, *Seismic Detection of Personnel: Field Trials and Signatures Database*, Army Engineer Research and Development Center, Hanover, Germany, 2007.
- [8] X. Jin, S. Gupta, A. Ray, and T. Damarla, "Multimodal sensor fusion for personnel detection," in *Proceedings of the 14th International Conference on Information Fusion*, Chicago, Ill, USA, July 2011.
- [9] P. K. Varshney, "Personnel detection via fusion of heterogeneous sensor data," OMB No. 0704-0188, 2009.
- [10] D. Li, K. D. Wong, Y. H. Hu, and A. M. Sayeed, "Detection, classification, and tracking of targets," *IEEE Signal Processing Magazine*, vol. 19, no. 2, pp. 17–29, 2002.
- [11] A. Pakhomov and T. Goldburt, "Seismic signals and noise assessment for footstep detection range," *The International Society for Optics and Photonics*, vol. 5417, pp. 87–98, 2004.

Research Article

Footstep and Vehicle Detection Using Slow and Quick Adaptive Thresholds Algorithm

Gökhan Koç^{1,2} and Korkut Yegin^{1,2}

¹ KoçSistem Information Communication Services Inc., 34700 Istanbul, Turkey

² Department of Electrical and Electronics Engineering, Yeditepe University, 34755 Istanbul, Turkey

Correspondence should be addressed to Gökhan Koç; gokhan.koc@kocsistem.com.tr

Received 15 May 2013; Accepted 4 September 2013

Academic Editor: Adnan Kavak

Copyright © 2013 G. Koç and K. Yegin. This is an open access article distributed under the Creative Commons Attribution License, which permits unrestricted use, distribution, and reproduction in any medium, provided the original work is properly cited.

An algorithm is developed for footstep, vehicle, and rain detection using seismic sensors operating in a wireless sensor network. Each standalone seismic sensor is coupled with a wireless node, and alarm conditions were evaluated at the sensor rather than at the gateway. The algorithm utilizes slow and quick adaptive thresholds to eliminate static and dynamic noise to check for any disturbance. Duration calculation and filters were used to identify the correct alarm condition. The algorithm was performed on preliminary field tests, and detection performance was verified. Footstep alarm condition up to 8 meters and vehicle presence alarm condition up to 50 meters were observed. Presence of rain did not create any alarm condition. Detection based on kurtosis was also performed and shortcomings of kurtosis especially for vehicle detection were discussed, proposed algorithm has minimal load on the sensor board and its data processing unit; thus, it is energy efficient and suitable for wireless sensor alarm networks.

1. Introduction

Unauthorized human detection is an important and, mostly, an integral part of any security system. In building and perimeter of the building are two essential components of these security systems. In building or immediate vicinity of the structure can be monitored with cameras or security personnel, but perimeter of the building, especially wide open area security systems, requires sensors for intruder detection. Those sensors can be of many different forms ranging from passive and/or active infrared, thermal, seismic, ultrasound, and microphones to electromechanical film. Visually obscured sensors are definitely desired, which makes seismic or acoustic sensors preferable over other sensors. In this study, we used seismic sensors to detect vibrations in the ground to identify and classify human, rain, and vehicle in the prescribed range of the sensor.

Detection methods are usually based on either time or frequency domain. High frequency vibrations decay faster than low frequency vibrations so that the frequency components of a signal can be difficult to differentiate depending on measurement distance. In addition, vibration transmission

characteristics are dependent on the soil type and weather conditions. Thus, frequency components of vehicle and footsteps can easily overlap due to vibration transmission characteristics of the soil. Nevertheless, two types of spectrum analyses methods exist for the intruder detection: narrow band and wide band spectrum analyses. Wide band spectrum analyses methods focus on single footstep and vehicle vibration. However, vehicle and footstep vibrations may have frequency components at the same frequency [1, 2]. On the other hand, narrow band spectrum analyses methods focus on several footsteps and vehicle components [3–5]. However, narrow and wide band spectrum analyses require FFT algorithms. Because of the limited memory and power, FFT use is not preferred in wireless sensor network devices. Although FFT may provide promising traffic detection, an alternate analog signal processing may be necessary due to demanding power requirements of FFT evaluation using digital circuits.

Another widely accepted detection method is “kurtosis”, which measures extreme deviations from mean signal [6]. However, detecting intruder movements with kurtosis does not produce clear successful results because vibration of

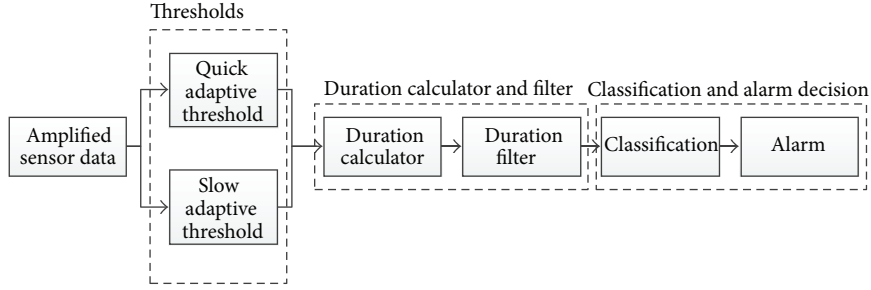


FIGURE 1: Blocks of signal processing algorithm.

certain types of noise can easily generate deviations similar to human steps. Another popular intruder detection method is based on “Copula” theory [7, 8]. Copula is in essence full measure of statistical dependence among random variables [7]. However, understanding and quantifying dependence is a challenging task in multivariate statistical modeling. Markov Models are also used in detection of footsteps [9]. Multimodal fusion of sensor data for detection was also proposed in a recent study [10].

The proposed system utilizes wireless communication among sensors that are standalone units and each unit has its own power supply (battery) to operate. All sensor boards are equipped with a wireless unit operating at 2.4 GHz to enable two-way (half duplex) communication between other sensors and the gateway. Geophone sensor SM-24 is used as the seismic sensor and electronic circuit that includes proper filtering and amplification is designed to process analog signal. Filtered and amplified sensor signal is digitized with 12-bit analog-to-digital-converter and processed for alarm conditions. Alarm conditions are communicated to a wireless sensor network (WSN) at 2.4 GHz. WSN board is designed using Texas Instruments transceiver (CC2420) and microcontroller family (MSP430F1611).

Detection also requires signal processing algorithm where human and vehicle classification can be done. Signal processing algorithm is utilized on the sensor board, and only alarm conditions are broadcasted to the network. The algorithm is designed to eliminate the effects of soil type, environment changes, and ambient noise. Design details of the algorithm are explained in Section 2. Typical scenarios for all types of threats are analyzed for performance evaluation in Section 3. Kurtosis based detection is discussed in Section 4.

2. Detection Algorithm

Detection algorithm works in real time and analyses durations of signals above two adaptive thresholds. The main reasoning behind defining adaptive thresholds is that there are time-dependent noise sources such as elevators, cranes, high power generators, and wind. These types of continuous noise sources generate noise at the same frequency of footsteps and vehicle movement. However, rain is not a continuous noise source, and, because of this, it is defined as a classification object.

Main parts of the algorithms are thresholds, duration calculator, duration filter, classification, and alarm decision as shown in Figure 1.

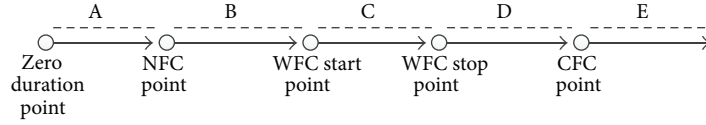
Two different thresholds are used to determine the durations of the signals: slow adaptive threshold (SAT) and quick adaptive threshold (QAT). SAT is following the noise level with a static and dynamic offset. SAT is designed to eliminate continuous noise effects from the classification by taking the average of the last incoming M number of sensor data and adding necessary offset values. To determine offset values, a power factor of average (PFA) is defined. PFA is simply a scalar, number and it empirically reflects maximum level of present noise to average noise. For instance, we used a PFA value of 3 in our algorithm to state that maximum noise level is most likely 3 times larger than the average, which is calculated for the last M data points (10K in our algorithm). Another scale factor called dynamic offset is also defined to account for soil and weather induced noise effects. Static offset is hardware dependent and is based on ambient noise level received by the sensor for the target detection range. SAT is calculated at every data point as follows:

$$\begin{aligned} \text{SAT}(i) = & \text{StaticOffset} \\ & + \text{DynamicOffset} * \text{PFA} * \sum_{k=i-M}^i \frac{\text{Data}(k)}{M}, \end{aligned} \quad (1)$$

where $\text{Data}(k)$ represents the seismic data. In a single vibration signal, the signal is fluctuating between ground and local maximum. To calculate above-noise durations, QAT is defined. Multiplying the predetermined PFA with the average of the last P (P is a fixed memory size in the matlab code) sensor data is equal to the QAT value. With QAT function, amplified signals get smoother and energy of these signals help to execute better classification, especially in the rain conditions:

$$\text{QAT}(i) = \text{PFA} * \sum_{k=i-P}^i \frac{\text{Data}(k)}{P}. \quad (2)$$

Duration calculator (DR) counts the number of samples where QAT is higher than SAT. With that, duration of



NFC: specific duration value for rain signal classification (NFC = 30 in matlab code)
WFC start: minimum footstep signal duration (WFC start = 35 in relative matlab code)
WFC stop: maximum footstep signal duration (WFC stop = 75 in relative matlab code)
CFC: minimum vehicle signal duration (CFC = 250 in relative matlab code)

FIGURE 2: Definitions of signal durations.

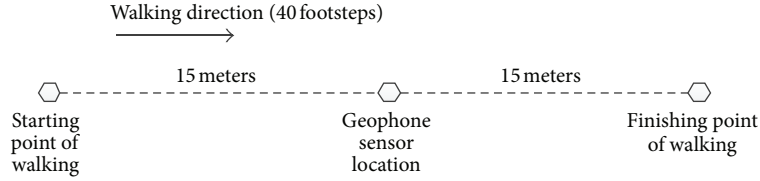


FIGURE 3: Test setup for footstep detection.

the intruder vibration signals is determined, and noise is removed from the calculations. DR is calculated as follows:

$$\text{if } (x) = \begin{cases} 1, & x \text{ is true,} \\ 0, & x \text{ is false,} \end{cases} \quad (3)$$

$$\text{DR}(i) = (\text{DR}(i-1) + 1) * \text{if}(\text{QAT}(i) > \text{SAT}(i)).$$

After calculating the durations, duration filter (DRF) is used to aid classification. DRF parameters are shown in Figure 2. DRF function removes durations in the intervals A, B, and D, but it does not remove several specific durations as stated in Figure 2. It can be expressed as follows:

$$\begin{aligned} \text{DRF}(i) &= \text{DR}(i) * \text{if}(\text{DR}(i) \geq \text{DR}(i+1)) \\ &\quad * \text{if}(\text{DRF}(i) = \text{NFC}), \\ \text{DRF}(i) &= \text{DR}(i) * \text{if}(\text{DR}(i) \geq \text{DR}(i+1)) \\ &\quad * \text{if}(\text{DRF}(i) = \text{NFC}). \end{aligned} \quad (4)$$

Next step is the classification from filtered duration sizes. Again, intervals and the duration marks in Figure 2 are used. For example, if the filtered duration value is in interval C, then that signal is named as a single footstep. Single alarm (SA) chooses only one signal type which is termed as either “RV” (rain vibration constant) or “FV” (footstep vibration constant) or “CV” (vehicle vibration constant). Hence, SA can be expressed as:

$$\begin{aligned} \text{SA}(i) &= \text{if}(\text{DRF}(i) * \text{RV}) \\ &\quad + \text{if}(\text{WFCStart} < \text{DRF}(i) < \text{WFCStop}) \\ &\quad * \text{FV} + \text{if}(\text{DRF}(i) > \text{CFC}) * \text{CV}. \end{aligned} \quad (5)$$

To reduce false alarm rate, repetition of similar type signals is examined by allocating virtual memory slots called “RM” (rain memory), “FM” (footstep memory), and “CM” (vehicle

memory) where SA function outcome is constantly monitored and signals are stored in their respective virtual memory slots. At the decision stage, “A” (alarm) function checks these memory slots and counts the signal numbers. If the number of signals in the memories exceeds a threshold value, footstep alarm, rain alarm, or vehicle alarm is generated. Virtual memory slots and alarm are defined as follows:

$$\text{RM}(i) = \sum_{k=i-\text{RMS}}^i \text{SA}(k) * \text{if}(\text{DRF}(i) = \text{NFC}),$$

$$\begin{aligned} \text{FM}(i) &= \sum_{k=i-\text{FMS}}^i \text{SA}(k) \\ &\quad * \text{if}(\text{WFCStart} < \text{DRF}(i) < \text{WFCStop}), \end{aligned}$$

$$\text{CM}(i) = \text{SA}(i) * \text{if}(\text{DRF}(i) > \text{CFC}),$$

$$\begin{aligned} \text{A}(i) &= \text{RM}(i) * \text{if}(\text{RM}(i) > 2) + \text{FM}(i) * \text{if}(\text{FM}(i) > 10) \\ &\quad + (\text{CM}(i) + 2) * \text{if}(\text{CM}(i) > 0). \end{aligned} \quad (6)$$

Definitions and values of all these constants are given in Table 1. Algorithm constants was mostly arrived at trial error at the beginning, but, after extensive trial tests, probability of detection and false alarm rates were used to finalize their values for optimum performance.

3. Algorithm Performance

A preliminary test setup is formed to test the algorithm. In all tests, intruders are following a line where sensor is placed in the middle as illustrated in Figure 3. Data were collected with seismic sensors with 250 samples/second. Each seismic sensor is coupled with a wireless node operating in a WSN. Alarm “1” is defined as rain, “2” is footstep, and “5” is vehicle.

TABLE 1: Definitions of constants in the algorithm.

Constant Name	Value	Definition
M	10000	Memory size of SAT
P	30	Memory size of QAT
Static offset	200	Static difference between SAT and QAT
Dynamic offset	1.3	Proportional difference between SAT and QAT
PF of average (PFA)	3	The standard ratio between the amplitude of a seismic signal and average
Noise_Filter_Constant (NFC)	30	Specific rain vibration duration
Walking_Filter_Constant_Start	35	Minimum duration of a single footstep vibration
Walking_Filter_Constant_Stop	75	Maximum duration of a single footstep vibration
Car filter constant (CFC)	250	Minimum duration of a single vehicle vibration
Rain memory (RM)	10000	Memory, which is used in the classification of rain
Footstep memory (FM)	2000	Memory, which is used in the classification of footstep
Car memory (CM)		Memory, which is used in the classification of vehicle
Rain alarm (RA)	1	Classified alarm value of rain situation
Footstep alarm (FA)	2	Classified alarm value of footstep situation
Car alarm (CA)	5	Classified alarm value of vehicle situation

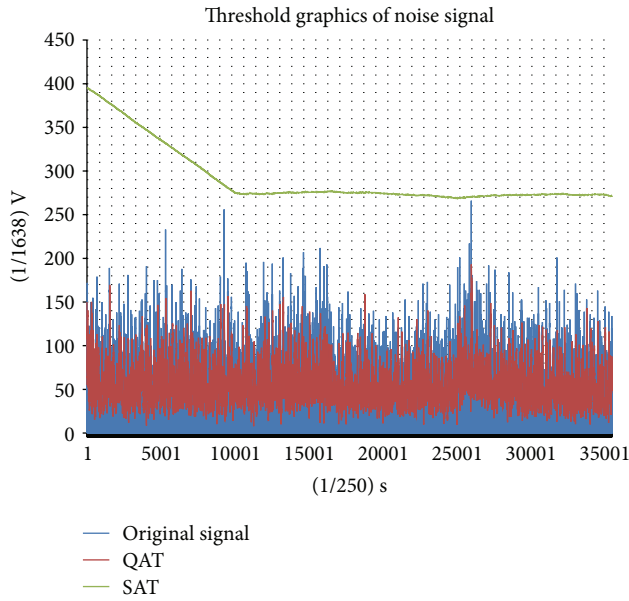


FIGURE 4: Thresholds and original signal for noise only signal.

3.1. Noise Performance. Noise data were collected without moving or making any vibration on the ground to test false alarm rate of the algorithm. Raw data with SAT and QAT are shown in Figure 4, and duration calculators and filters are shown in Figure 5. An alarm was not triggered by the algorithm. Also, QAT did not pass SAT at any point of the original signal as expected.

3.2. Footstep Detection. Footstep detection tests were performed in two different test locations. In Test-1, amplification gain of the seismic signal is chosen as 3000 and in Test-2 as 5000. In footstep tests, 30-meter path walked down and 40 footsteps were generated. Original signal for Test-1, its SAT

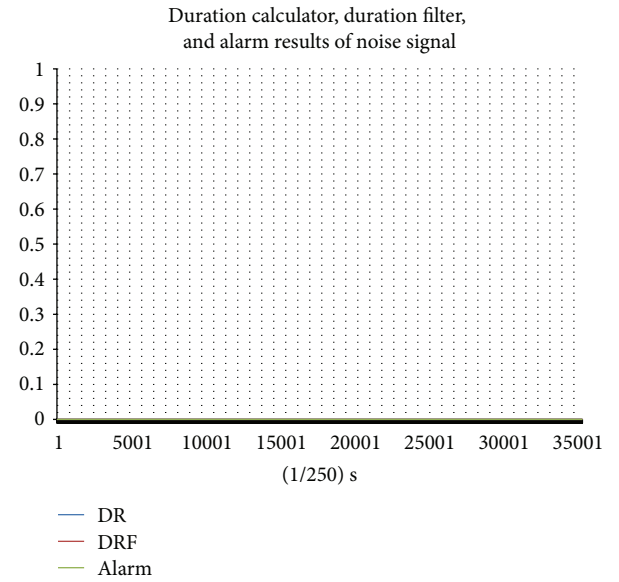


FIGURE 5: Duration, filtered duration, and alarm results for noise only data.

and QAT values, and duration filters with alarm classification are shown in Figures 6, 7, and 8, respectively.

In both tests, 40 steps have been taken and 20 of them have been detected as footsteps. With this, footstep detection range was observed to be close to 8 meters. However, the range can be increased with higher amplification of seismic signals. 32 of 40 footsteps have been detected and 11 of them were classified as a noise. The algorithm produced one false alarm only. Detailed footstep detection test performances are listed in Table 2.

3.3. Vehicle Detection. Vehicle detection tests were executed in two different test locations each having different vehicle

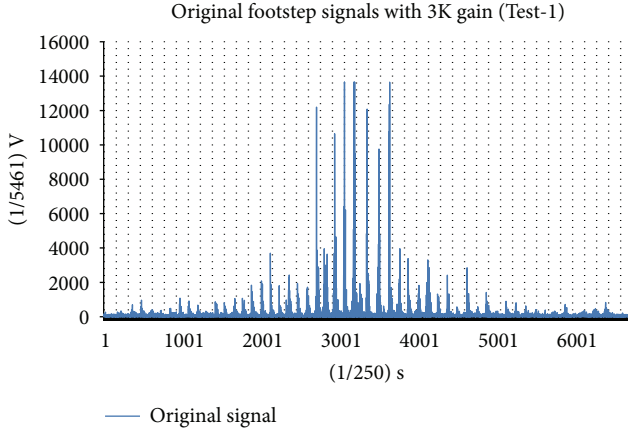


FIGURE 6: Original footstep signal.

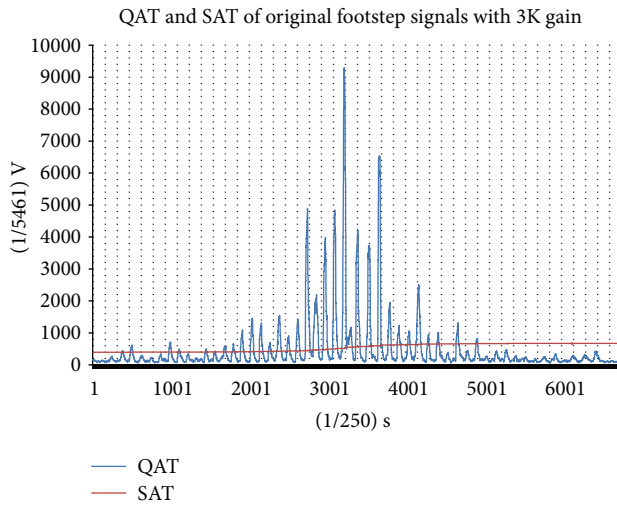


FIGURE 7: QAT and SAT of original footstep signal.

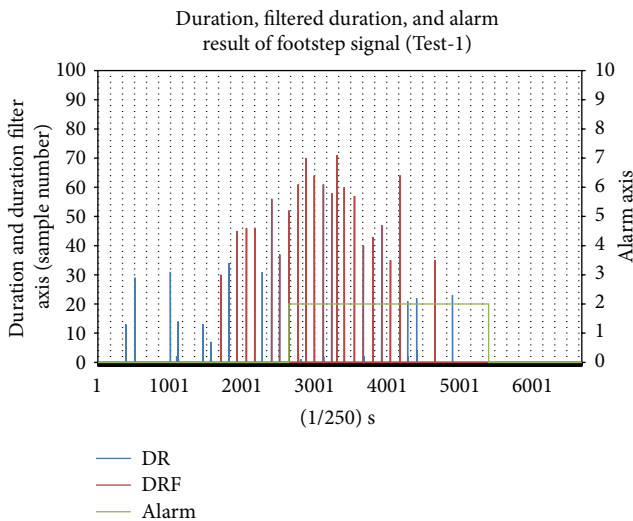


FIGURE 8: Duration, filtered duration, and alarm result of footstep signal.

TABLE 2: Footstep detection tests performance.

Detected Signals	Test-1	Test-2
Detected as noise	11	10
Detected as footstep	20	21
Detected as rain	1	0
Detected as vehicle	0	0
Total	32	32

TABLE 3: Rain test performance.

Detected Signals	Test-1	Test-2
Detected as noise	32	22
Detected as footstep	1	1
Detected as rain	6	3
Detected as vehicle	0	0
Total	39	26

speeds. In Test-1, vehicle speed was 10 Km/hr, and, in Test-2, it was 30 Km/hr. The test setup is illustrated in Figure 9. Original signal for Test-1, corresponding SAT and QAT values, and duration filters with alarm classification are shown in Figures 10, 11, and 12, respectively. In both tests, vehicle presence was detected.

3.4. Rain Detection. Rain detection tests were executed at two different test locations. Original signal for Test-1, corresponding SAT and QAT values, and duration filters with alarm classification are shown in Figures 13, 14, and 15, respectively. In both tests, unwanted signals were detected, but they did not produce any false alarms. Detailed rain detection test performances are listed in Table 3.

4. Detection with Kurtosis

Kurtosis measures the “peakedness” of the real random variable. There are different versions of kurtosis, but we used the most common one for intruder detection:

$$\text{kurtosis} = \frac{(\sum_i^N (X_i - \mu)^4) / (N - 1)}{((\sum_i^N (X_i - \mu)^2) / (N - 1))^2}. \quad (7)$$

Kurtosis values are calculated by dividing the data to extracted intervals. The sample number in these intervals is called “N” whereas “μ” is the mean of this interval. It is easy to observe that kurtosis is more sensitive to sudden changes in the data. Therefore, we expect kurtosis to perform better for rain detection and relatively worse for vehicle detection. Kurtosis for different interval samples was analyzed in Figure 16. Kurtosis values of footsteps were varying between 10 and 65. They intersect with noise only in a small interval. Also, the kurtosis values of footstep are increasing with the interval size. However, if the interval size grows a bit more, they will signal several footsteps despite a single footstep. Therefore, interval should contain a number of samples between 80 and 120. It is observed that kurtosis was successful at detecting footsteps and rain; however, for vehicle

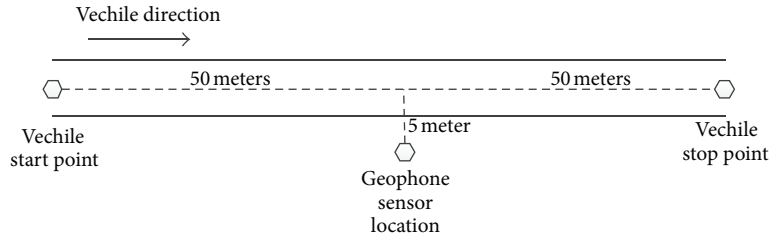


FIGURE 9: Vehicle test description.

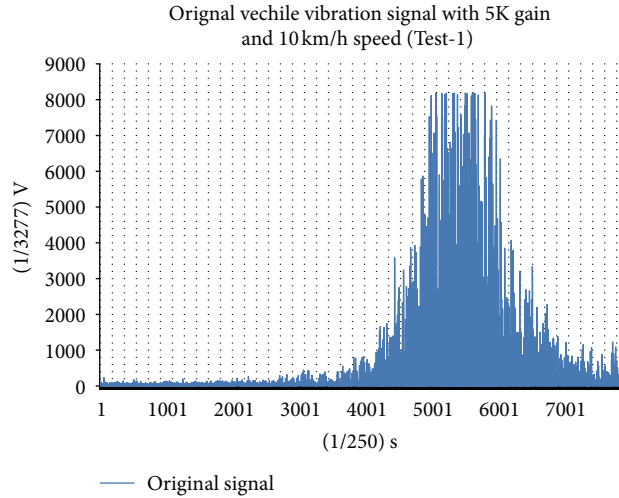


FIGURE 10: Original vehicle vibration signal for 10 Km/hr speed (Test-1).

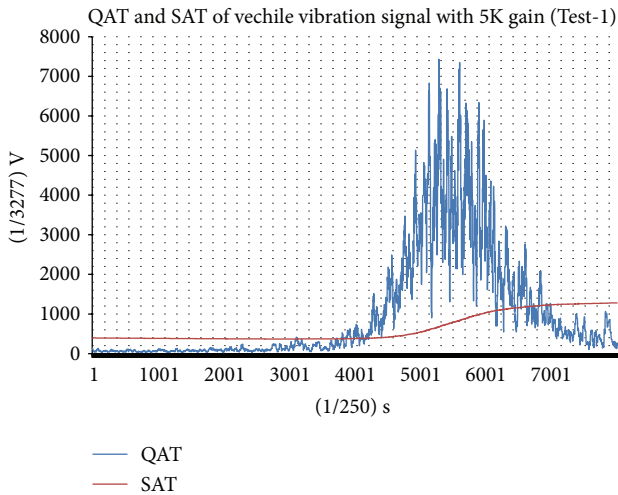


FIGURE 11: QAT and SAT of original vehicle signal (Test-1).

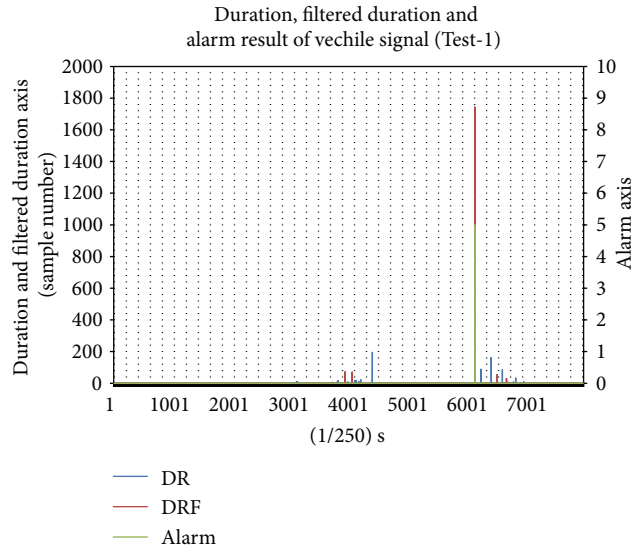


FIGURE 12: Duration, filtered duration, and alarm result of vehicle signal (Test-1).

detection, kurtosis was not a suitable detection algorithm without any modification.

5. Conclusion

Real-time detection using seismic sensor data was developed to identify the presence of footsteps, vehicle, and rain.

Algorithm is based on slow and adaptive quick thresholds with duration calculators and filters. Proposed algorithm was tested on several test scenarios, and its detection and classification success were assessed on several field tests.

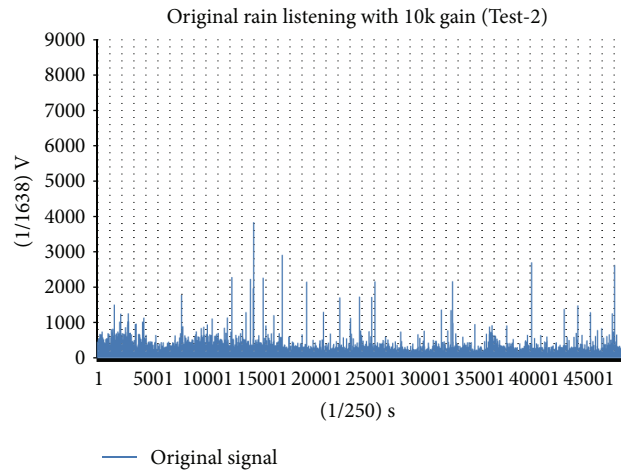


FIGURE 13: Original rain signal (Test-2).

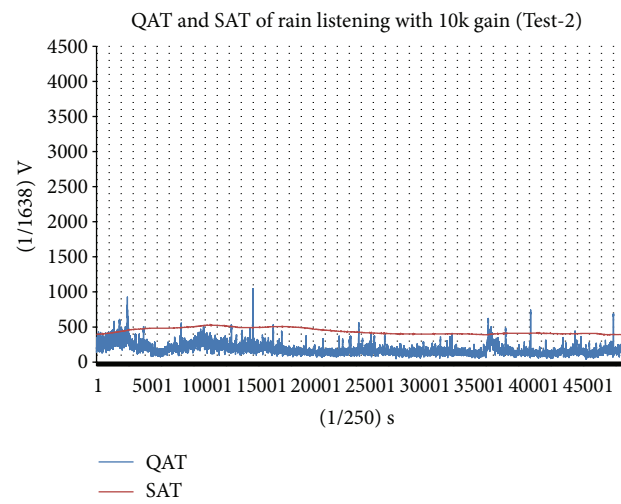


FIGURE 14: QAT and SAT of rain signal (Test-2).

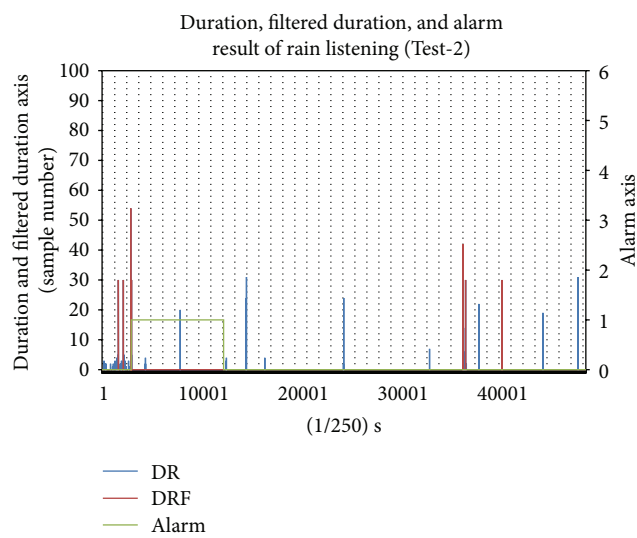


FIGURE 15: Duration, filtered duration, and alarm result of rain signal (Test-2).

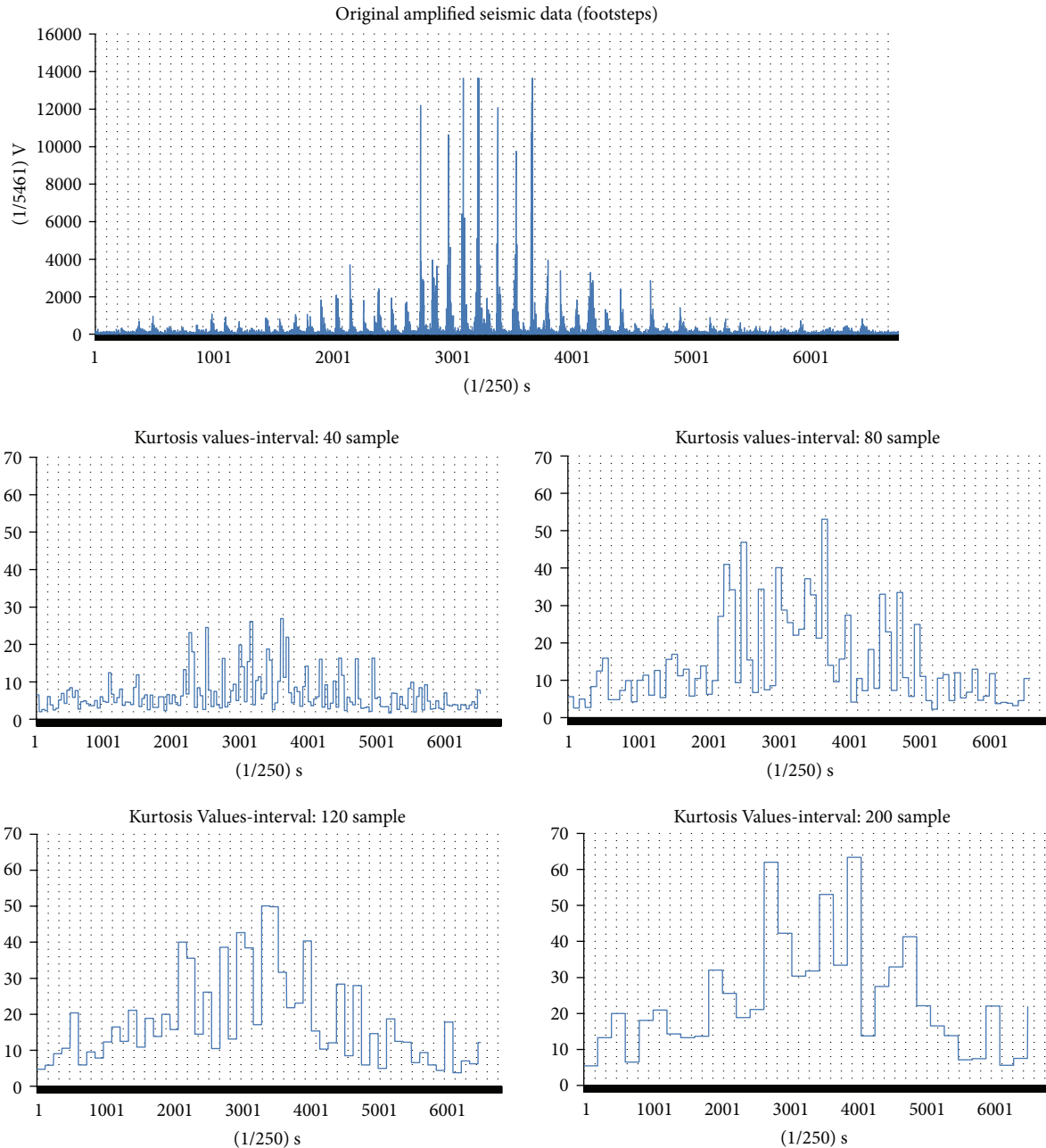


FIGURE 16: Kurtosis of footstep data with different interval sizes.

Footstep detection up to 8 meters and moving vehicle with two different speeds were detected successfully. Kurtosis based algorithm was also developed for comparison, and it was observed that kurtosis was not adequate in classification of all three response types. Although two different test scenarios were implemented, the algorithm needs further verification with extensive field tests.

References

- [1] V. V. Reddy, V. Divya, A. W. H. Khong, and B. P. Ng, "Footstep detection and denoising using a single triaxial geophone," in *Proceedings of the Asia Pacific Conference on Circuit and System (APCCAS '10)*, pp. 1171–1174, December 2010.
- [2] R. Libby, "A simple method for reliable footstep detection on embedded sensor platforms," 2009.
- [3] G. L. Goodman, *Detection and Classification for Unattended Ground Sensors*, Land Operations Division, Salisbury, UK, 1999.
- [4] G. L. Goodman, "Detection and classification for unattended ground sensors," in *Proceedings of the IEEE Conference on Information Decision and Control (IDC '99)*, pp. 419–424, 1999.
- [5] W. E. Audette, D. B. Kynor, J. C. Wilbur, J. R. Gagne, and L. Peck, "Improved intruder detection using seismic sensors and adaptive noise cancellation," in *Human, Light Vehicle, and*

Tunnel Detection Workshop, pp. 1–14, Hanover, Germany, June 2009.

- [6] G. Succi, D. Clapp, R. Gampert, and G. Prado, “Footstep detection and tracking,” in *Unattended Ground Sensor Technologies and Applications III*, vol. 4393 of *Proceedings of SPIE*, pp. 22–29, April 2001.
- [7] P. K. Varshney, “Personnel detection via fusion of heterogeneous sensor data,” Final Report 0704-0188, OMB, Syracuse, NY, USA, 2009.
- [8] K. M. Houston and D. P. McGaffigan, “Spectrum analysis techniques for personnel detection using seismic sensors,” in *Unattended Ground Sensor Technologies and Applications V*, vol. 5090 of *Proceedings of SPIE*, pp. 162–173, April 2003.
- [9] R. S. Blum and S. A. Kassam, “Optimum distributed detection of weak signals in dependent sensors,” *IEEE Transactions on Information Theory*, vol. 38, no. 3, pp. 1066–1079, 1992.
- [10] X. Jin, S. Gupta, A. Ray, and T. Damarla, “Multimodal sensor fusion for personnel detection,” in *Proceedings of the 14th International Conference on Information Fusion (Fusion ’11)*, pp. 437–444, Chicago, Ill, USA, July 2011.

Research Article

Reconfigurable Antenna Assisted Intrusion Detection in Wireless Networks

Prathaban Mookiah,¹ John M. Walsh,¹ Rachel Greenstadt,² and Kapil R. Dandekar¹

¹ Department of Electrical and Computer Engineering, Drexel University, Philadelphia, PA 19104, USA

² Department of Computer Science, Drexel University, Philadelphia, PA 19104, USA

Correspondence should be addressed to Kapil R. Dandekar; dandekar@coe.drexel.edu

Received 7 June 2013; Accepted 20 August 2013

Academic Editor: Korkut Yegin

Copyright © 2013 Prathaban Mookiah et al. This is an open access article distributed under the Creative Commons Attribution License, which permits unrestricted use, distribution, and reproduction in any medium, provided the original work is properly cited.

Intrusion detection is a challenging problem in wireless networks due to the broadcast nature of the wireless medium. Physical layer information is increasingly used to protect these vulnerable networks. Meanwhile, reconfigurable antennas are gradually finding their way into wireless devices due to their ability to improve data throughput. In this paper, the capabilities of reconfigurable antennas are used to devise an intrusion detection scheme that operates at the physical layer. The detection problem is posed as a GLRT problem that operates on the channels corresponding to the different modes of a reconfigurable antenna. The performance of the scheme is quantified through field measurements taken in an indoor environment at the 802.11 frequency band. Based on the measured data, we study the achievable performance and the effect of the different control parameters on the performance of the intrusion detection scheme. The effect of pattern correlation between the different modes on the scheme's performance is also analyzed, based on which general guidelines on how to design the different antenna modes are provided. The results show that the proposed scheme can add an additional layer of security that can significantly alleviate many vulnerabilities and threats in current fixed wireless networks.

1. Introduction

Attacks on wireless networks have become increasingly sophisticated with the increasing pervasiveness of these networks. It is challenging to detect and counteract intrusions in wireless networks due to the inherent broadcast nature of the medium. Among many known security risks, man-in-the-middle attacks and spoofing attacks [1] pose a significant intrusion threat to wireless networks since such attacks allow intruders to hijack a connection already established by a legitimate user. Though advanced wireless intrusion protection and detection systems have been developed and deployed to mitigate such threats, it has been repeatedly demonstrated that each method has its point of failure and no single method guarantees protection against all attacks [2, 3].

Such a hostile landscape requires multiple levels of defense for network protection. This requirement has gradually led to a more cross-layer approach to wireless security in recent times where security mechanisms are being deployed

at different layers of the network. Particularly channel information available at the physical layer is being increasingly used to provide an additional degree of protection against intruders. Schemes that employ channel based security techniques can be categorized into encryption and authentication schemes. The former uses the wireless channel as a source for encryption key generation [4–9], while the latter utilizes a metric derived from the channel information as an identifier for authentication [10–16].

Intrusion detection has traditionally been categorized into misuse detection or anomaly detection techniques. While the former uses patterns characteristic of known attacks to detect known intrusions, the latter relies on detecting deviations from the established behavior patterns in the system [17]. In many usage scenarios, where the physical link remains unchanged over a session, the wireless channel response corresponding to the link can be considered to represent the established behavior pattern for that link. Any changes that violate this pattern abruptly beyond a certain

limit can be then checked for adversarial behavior. In this paper, we follow this approach where the channel is monitored for any abrupt changes in its statistics through repeated applications of the generalized likelihood ratio test (GLRT) [18]. The scheme is based on the idea that the statistics of the link corresponding to an intruder who is physically located at a different location will be different from that of the legitimate user and when the intruder tries to inject packets over the same connection, it will trigger an abrupt change in the GLR value.

Additionally we utilize a pattern reconfigurable antenna to improve the performance of the intrusion detection scheme. The ability of pattern reconfigurable antennas to enhance system throughput has been well demonstrated [19]. By picking antenna modes that are decorrelated in their radiation patterns, decorrelated channel realizations can be obtained to enhance system performance. Hence channels corresponding to different modes of the antenna can be expected to have different statistics, a property which is exploited to the benefit of the proposed detection scheme. However, the use of reconfigurable antennas (pattern diversity) should be differentiated from schemes that use multiple antennas (spatial diversity) with perfect decorrelation between the elements [11, 14, 16]. We relax any assumptions about channel correlation between the different diversity branches and specifically quantify the effect of correlation on detection performance. Moreover, a reconfigurable antenna provides a more practically viable solution to generate multiple channel realizations than spatially separated multiple antenna elements due to cost and space constraints.

In many public open networks (e.g., coffee shops) higher level authentication solutions are usually not implemented. Freely available software tools such as Firesheep can be used to simply execute session hijacking attacks when users visit insecure websites in such networks [20]. A wireless access point equipped with reconfigurable antennas that can implement the proposed method can be used to provide a layer of security that can significantly alleviate such security threats in these networks. In networks with higher level security mechanisms for encryption, authentication, and integrity, the proposed scheme can complement those mechanisms while they continue to play their part in securing the wireless link.

The rest of the paper is organized as follows. The intrusion detection problem and the threat model are described in Section 2. The detection scheme is described and the GLRT for intrusion detection is developed in Section 3. The channel measurement procedure is described in Section 4. We justify our assumption regarding the probability distribution of the channels in Section 5. The performance of the scheme is analyzed and the results are presented in Section 6. Some practical considerations are discussed in Section 7 before we conclude this paper in Section 8.

2. Problem Definition and Threat Model

The problem that is addressed in this paper is one of detecting an intruder who has gained access into the system by means of hijacking a connection already established by a legitimate user. The problem scenario consists of three players:

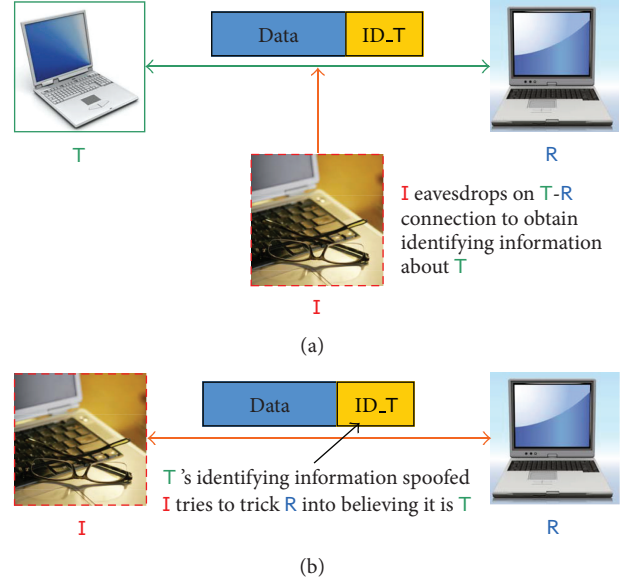


FIGURE 1: Illustration of the problem. (a) T eavesdrops on a data transfer session between R and T to obtain sensitive information about T's identity. (b) After obtaining the information, I tries to masquerade as T to R.

the receiver R, transmitter T, and an intruder I. Transmitter T and receiver R have established a connection and are in the process of exchanging information as shown in Figure 1(a). Intruder I eavesdrops into this connection and waits till he gathers sufficient information to spoof T. A surprisingly large number of vulnerabilities exist in modern wireless access technologies that allow I to obtain this information with relative ease. Once this information is obtained, I launches a spoofing attack by posing as T to R as shown in Figure 1(b).

To gain a practical perspective of the problem, R can be thought of as a wireless access point through which T is connected to the organizational network. I can be an adversarial entity whose objective is to gain entry into the organizational network, hijack T's connection with R, or launch a man-in-the-middle attack on the connection between T and R among other possibilities. The objective of the security scheme is to detect this change in the real transmitter at R in order to initiate counter measures.

To achieve his goal, I can be equipped with a powerful transceiver capable of passively monitoring and capturing all traffic between T and R and sufficient computational resources to analyze the traffic to exploit the vulnerabilities in relatively quick time. I can be an external adversary attempting to launch an attack on the network from outside the organization's premises or an internal entity who is interested in launching an attack on T. In both cases, we note that I cannot be physically colocated with T which forms the basis of our method for intrusion detection.

It should be noted that I's motive is to compromise T's identity in the network and therefore it is imperative for I that T first initiates and establishes a connection with R. Therefore, it is assumed that I will not resort to jamming attacks to prevent T from establishing a successful connection with R.

Additionally, we assume that only R is equipped with a reconfigurable antenna with M modes since it is more likely that an access point is equipped with such an antenna than a user terminal due to cost and space constraints. Therefore, we also assume T and R to be equipped with standard omnidirectional antennas.

As stated earlier, the proposed solution exploits the fact that T and I have to be located in two different physical locations which would be manifested by two different channel distributions sensed by R. Due to the multipath structure of the environment, I cannot methodically manipulate the channel between itself and R in such a way as to imitate the channel between T and R. This is because it does not and cannot know the channel between T and R. Introducing reconfigurable antennas to the solution adds multiple channel distributions corresponding to each mode used in the antenna. This makes the problem of closely matching the channel corresponding to T even more challenging for I which results in enhanced protection. However, it should be noted that our scheme does not attempt to localize T or I. Instead, channel information pertaining to the different antenna modes is used to detect I if it compromises the existing link between T and R.

3. Description of Scheme

With the notable exception of mobile networks, many current and emerging wireless data networks are associated with stationary terminals at both ends of the link. Temporal variations in channels related to such networks arise mainly due to movements of people and objects in the vicinity of the terminals as well as small localized movement of the terminals within a very small area [21–23]. A typical example for such a scenario would be a user seated at a bench in a public place accessing the network from a laptop connected to an access point in the vicinity. This work addresses intrusion problems that pertain to such wireless network usage scenarios and does not address large-scale terminal mobility.

The amplitude of the estimated complex channel coefficient, corresponding to a single frequency carrier g , is denoted by h . The probability distribution of h follows a Ricean or Rayleigh distribution. We choose the latter distribution with parameter σ to describe h for reasons that will be discussed in Section 5:

$$p_{\sigma}(h) = \frac{h}{\sigma^2} e^{-h^2/2\sigma^2}. \quad (1)$$

During the connection establishment process, $\sigma = \sigma_0$ corresponding to T is estimated through a sequence of training packets. At some time instant when I succeeds in spoofing T, it will hijack this connection. However, since I is at a physically different location, $\sigma = \sigma_1$, corresponding to this link, will be different from σ_0 and will be unknown.

Let h_i ($i \in \mathbb{Z}$, $i > 0$) be a sequence of observed i.i.d. channel estimates from the incoming packets after the initial training stage and $\mathbf{h} = [h_j, \dots, h_k]$. i can be taken to denote the packet or time index. $N = k - j + 1$ is the block size. If we denote $\sigma(\mathbf{h})$ as the σ value of the Rayleigh

distribution from which the elements of \mathbf{h} originated, the intrusion detection problem can be now formulated as a hypothesis testing problem as follows:

$$\begin{aligned} H_0 : \sigma(\mathbf{h}) &= \sigma_0, \\ H_1 : \sigma(\mathbf{h}) &\neq \sigma_0. \end{aligned} \quad (2)$$

We employ a Neyman-Pearson detector which decides H_1 if the likelihood ratio exceeds a threshold:

$$L(\mathbf{h}) = \log \left(\frac{p_{\sigma_1}(\mathbf{h}; H_1)}{p_{\sigma_0}(\mathbf{h}; H_0)} \right) > \gamma. \quad (3)$$

However, σ_1 is not known in our case. In this case, it is well known that the GLRT which replaces σ_1 with its maximum likelihood estimate (MLE) is asymptotically the uniformly most powerful among all tests [18]. Hence, we resort to the GLRT that uses the MLE of σ_1 denoted by $\hat{\sigma}_1$. Estimation is done over the elements in block \mathbf{h} . The MLE for σ_1^2 is given by [24]

$$\hat{\sigma}_1^2 = \frac{1}{2N} \sum_{i=j}^k h_i^2. \quad (4)$$

Substituting (4) into (3) and simplifying yields:

$$L(\mathbf{h}) = \left(\frac{2N\sigma_0^2}{\lambda} \right)^N e^{(\lambda/2\sigma_0^2 - N)}, \quad (5)$$

where $\lambda = \sum_{i=j}^k h_i^2$.

The use of multiple antenna modes will result in M different channel realizations at each time instant. The environment “seen” by the different modes of the antennas will be different due to the differences in their radiation patterns and therefore the distribution for each of these M channel realizations will be characterized by different σ 's. Assuming that the channel realizations yielded by the different antenna modes are independent, we can now write

$$L(\mathbf{h}) = \log \left(\prod_{m=1}^M \frac{p_{\sigma_{1m}}(\mathbf{h}_m; H_1)}{p_{\sigma_{0m}}(\mathbf{h}_m; H_0)} \right) > \gamma, \quad (6)$$

where σ_{0m} and σ_{1m} are the distributions' parameters for mode m under the null and alternate hypothesis, respectively, \mathbf{h}_m represents the channel vector for mode m . The decision function and is simplified to:

$$L(\mathbf{h}) = \sum_{m=1}^M \left[\left(\frac{2N\sigma_{0m}^2}{\lambda_m} \right)^N e^{(\lambda/2\sigma_{0m}^2 - N)} \right], \quad (7)$$

where $\lambda_m = \sum_{i=j}^k h_{im}^2$ and h_{im} denotes the channel realization at time instant i for the m th antenna mode.

The control parameters that can be used to tune the performance of this scheme are listed in Table 1.

A graphical depiction of these parameters are shown with respect to a sample evolution of $L(\mathbf{h})$ in Figure 2.

TABLE 1: Control parameters.

Parameter	Description
N	Block size. Number of most recent consecutive channel estimates used in the test including the estimate corresponding to the packet under test.
N_T	Number of training packets used to estimate σ_0 during connection initialization.
γ	Threshold. It can be set based on the values of $L(\mathbf{h})$ observed during the training phase.
N_D	Detection delay. Maximum number of packets from I within which it should be detected. If detection does not happen by this time, it is considered a missed detection.
N_F	Number of packets from T before I takes over. Though this is not a controllable parameter in real time, it has a critical effect on the false alarm rate.
M	Number of antenna modes.

3.1. Steps of the Detection Scheme

- (1) During the outset of the session, R estimates σ_0 through training. The number of packets used for training is denoted by N_T .
- (2) R also computes $L(\mathbf{h})$ for $j = i - N + 1$ and $k = i$ based on these channel estimates at each instant i ($N \leq i \leq N_T$).
- (3) Actual transmissions begin from T and R continues to compute $L(\mathbf{h})$ for each packet transmission. I is assumed to hijack this connection and starts transmitting to R after N_F transmissions from T.
- (4) Based on these computed $L(\mathbf{h})$ during the training phase, a threshold γ is picked such that an alarm is raised whenever $L(\mathbf{h}) > \gamma$.
- (5) In the event of an alarm, a higher layer reauthentication procedure can be evoked to reverify the identity of the transmitter.

3.2. Threshold Selection. The value of γ will be chosen based on the values observed for $L(\mathbf{h})$ during the training period. If the maximum value of $L(\mathbf{h})$ observed during training is $L_M(\mathbf{h})$, we can express γ as $KL_M(\mathbf{h})$ where K is the scaling factor that needs to be controlled in order to achieve the desired detection and false alarm rates. In our scheme, selection of K is performed in an adaptive manner. We start with $K = 1$ and gradually increase its value till an acceptable false alarm rate is achieved.

The connection can be vulnerable to an attack during this threshold selection phase as well. Therefore, higher layer authentication protocols (e.g., 802.11i) should be evoked to verify false alarms during this adaptation process to ensure security until the target value of K is reached though this may cause some processing overhead due to frequent reauthentication. Optionally, depending on the level of threat to which the network is exposed to, this reauthentication process can be relaxed during this adaptive threshold determination

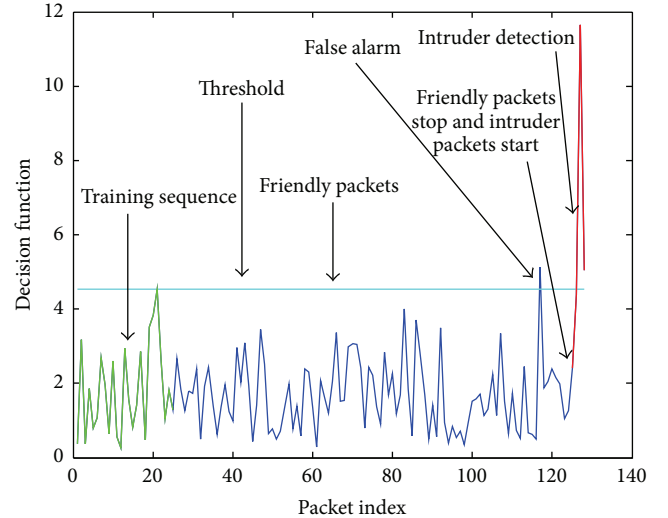


FIGURE 2: Sample evolution of the GLRT. $N_T = 25$, $N_F = 100$, $N = 5$, and $M = 1$. Threshold in this case is chosen to be the maximum of $L(\mathbf{h})$ observed during training.

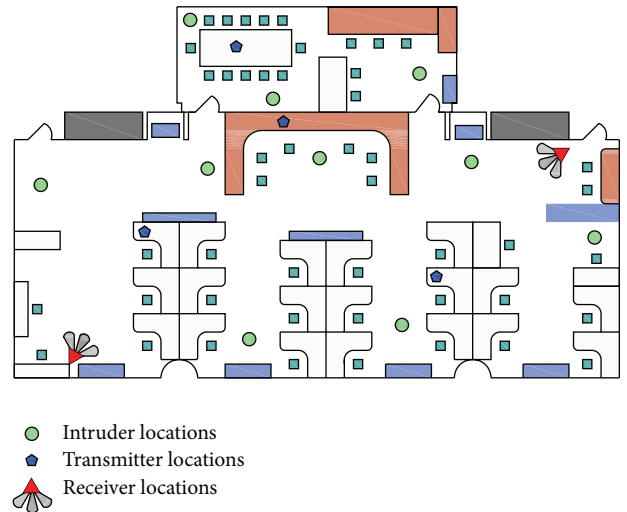


FIGURE 3: Layout of measurement environment. Test locations of R, T, and I are indicated as shown in the figure.

phase for more efficient operation and all alarms may be treated as false alarms.

4. Channel Measurements

Channel measurements were performed on Drexel University campus using a four-port vector network analyzer. The measurement environment and node locations are shown in Figure 3. The environment is a large laboratory which is 20 m long, 8 m wide, and 4 m high with plaster walls. The room has several cubicles partitioned using metallic walls and laboratory equipment and furniture distributed throughout the room.

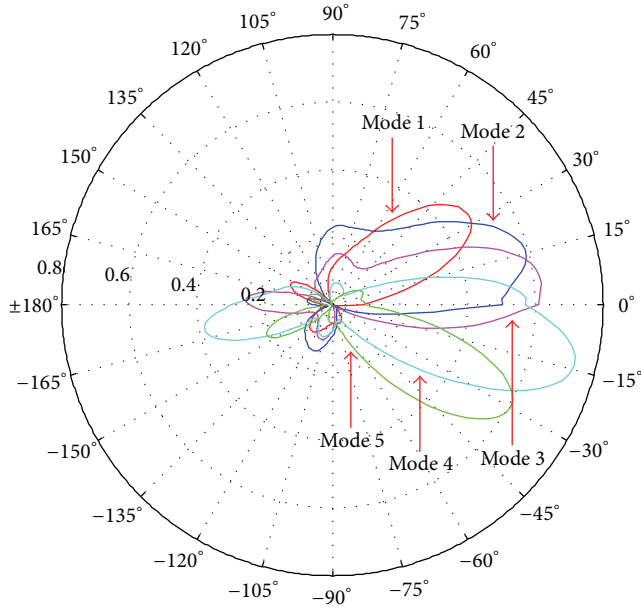


FIGURE 4: Radiation patterns corresponding to the 5 different antenna modes in the elevation plane. The elevation plane corresponds to the measurement environment plane shown in Figure 3. All patterns are vertically polarized.

The measurements were performed with R equipped with a reconfigurable leaky wave antenna (LWA) [25]. The radiation patterns corresponding to the five modes used in the study are shown in Figure 4. T and I were equipped with standard monopoles. Measurements were performed at 2.484 GHz which corresponds to the center frequency of channel 14 of the 802.11 band. Two R, four T, and ten I locations were chosen which yielded a total of eight R – T links each with then corresponding R – I links. For each (R, T, I) combination, 1000 time snapshots were recorded for the R – T and R – I links for the 5 different antenna modes. Measurements were performed during different hours of the day over several days during which there was low to moderate movement in the environment.

5. Why Rayleigh Distribution?

It has been assumed that the channel amplitudes follow a Rayleigh distribution instead of the more general Ricean distribution for the purposes of this study. In order to justify this assumption, the empirical distribution functions obtained for each link from the measured data was compared to a Rayleigh or Ricean distribution whose parameters were estimated from the measurements. The similarity between the empirical distribution (p_e) and standard distribution (p_p) for each link is quantified through two metrics: the total variation distance between the distributions and the Kullback-Leibler (KL) divergence.

The total support S is defined as

$$\min(S_e, S_p) \leq S \leq \max(S_e, S_p), \quad (8)$$

where S_e and S_p are the supports of the empirical and standard distributions, respectively. S is discretized into T evenly spaced discrete points. The total variation distance between the two distributions is defined as

$$e = \frac{1}{2} \sum_{t=1}^T |p_e(h_t) - p_p(h_t)|, \quad (9)$$

where $p_e(h_t)$ and $p_p(h_t)$ denote the values of the distributions evaluated at the t th discrete point in S . The KL divergence between p_e and p_p is defined as

$$D_{\text{KL}}(p_e \parallel p_p) = \sum_{t=1}^T p_e(h_t) \log_2 \frac{p_e(h_t)}{p_p(h_t)}. \quad (10)$$

Table 2 lists the trends in the observed values over all the measured links for the difference between the empirical distribution and the two standard distributions.

As can be observed, though the channel distributions are not “purely” Rayleigh nor Ricean, which is to be expected, they resemble these distributions sufficiently enough which provides us with the ability to develop an analytical framework for the problem. Moreover, as the values indicate, on average, due to the combination of line-of-sight (LOS) and nonline-of-sight (NLOS) links, modeling the channel as Rayleigh does not lead to a large error compared to modeling it as Ricean in the system, though the observed distributions marginally resemble the Ricean distribution more than the Rayleigh. Nevertheless, Rayleigh distribution was picked over Ricean for three reasons. Closed form MLE estimates do not exist for the parameters that characterize Ricean distributions and it requires recursive methods that are computationally intense [26]. The second reason is that when small values of N are used in the scheme, the recursive scheme does not achieve convergence resulting in very poor estimates that will have a significantly negative effect on the scheme’s performance. Finally, a simpler form of GLRT function cannot be formulated due to the Bessel functions that characterize Ricean distributions which will lead to higher computational complexity. Based on these observations and reasons, the channel was modeled as Rayleigh distributed.

6. Analysis and Results

The performance of the intrusion detection scheme was studied in terms of the probability of missed detection (β) and false alarm rates (α) as a function of the different control parameters listed in Section 3. α and β characteristics presented in this section were computed from the measured channels as follows.

- (1) For each (R, T, I) combination, a detection threshold γ was obtained through the first N_T training samples.
- (2) For the N_F subsequent samples from T, the number of instances where $L(\mathbf{h})$ exceeds γ was recorded. A false alarm was recorded when the number of instances was greater than one.
- (3) The friendly samples were followed by samples from I. A detection was recorded if $L(\mathbf{h})$ exceeds γ within

TABLE 2: Difference between empirical and parametric distributions.

Distribution	Mean of e	Standard deviation of e	Mean KL divergence
Rayleigh	0.059	0.014	1.56
Ricean	0.036	0.014	0.32

the first N_I transmissions from I. If not, a miss was recorded.

- (4) This process was repeated for 100 trials with different subsets of friendly and adversary samples and the average α and β were computed.
- (5) The overall α and β were computed as the average obtained over all possible (R, T, I) combinations.

Unless specifically otherwise stated, the presented results also reflect the average over the different antenna combinations possible for a given M ; that is, for a given α , the presented missed detection probabilities are averages obtained over the $\binom{5}{M}$ possible combinations for a given M .

6.1. Single Antenna Mode ($M=1$). Figure 5 shows the average detection error tradeoff (DET) curves for a single antenna mode for different values of block size N . The nonlinear scaling of the axes in a DET curve is designed to yield a straight line when $L(\mathbf{h})$ from the system follows a normal distribution [27]. The diagonal line defined by $\beta = -\alpha$ represents completely random performance and curves that lie on the quadrant left of this line represent positive levels of performance.

It can be observed that the performance improves with block size. This is due to two reasons. A larger block size gives a better estimate for σ_1 and hence when the intruder starts injecting packets, the difference between σ_0 and σ_1 becomes more clear which in turn results in $L(\mathbf{h})$ growing above the threshold rapidly. Moreover, when N is large, the increased contribution from channels corresponding to I in $L(\mathbf{h})$ after the intrusion will result in a rapid increase in its value as well.

Moreover, the values of N used in the computation of $L(\mathbf{h})$ are not sufficiently large enough to yield a Gaussian behavior and therefore the DET curves do not exhibit a linear trend. While such a Gaussian behavior is preferred since it allows us to resort to standard normal distributions to set the threshold γ , it will not be possible to employ a sufficiently large N to yield this behavior since a meaningful minimum detection delay N_D is determined by the block size.

However, with just a single antenna mode, the achievable detection rates are unacceptably low at low α regions. In cases where σ_1 and σ_0 are not well separated, the level of increase in $L(\mathbf{h})$ after intrusion will not be sufficient enough to match the γ that is required to maintain a low α which in turn leads to poor detection rates. To gain insights into this, we define the maximum percentage difference between σ 's among the different antenna modes as

$$P = \max_{m=1, \dots, M} \frac{|\sigma_{1m} - \sigma_{0m}|}{\sigma_{0m}} \times 100\%. \quad (11)$$

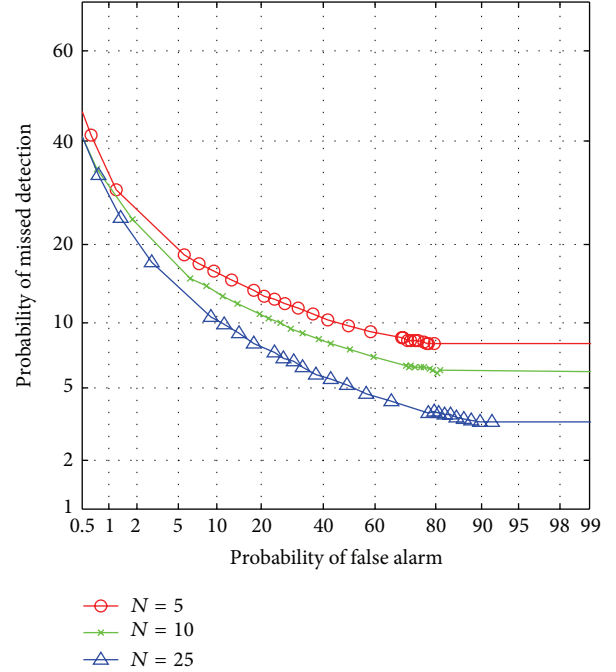


FIGURE 5: Average DET curves for a single antenna ($M = 1$) mode for different values of N . N_D is equal to N for each curve. $N_T = 25$. For a given α , β decreases with the block size. However, at low α levels, the corresponding β levels remain unacceptably high for a single antenna mode even at relatively large block sizes.

TABLE 3: Statistics pertaining to P from measured links.

	$M = 1$	$M = 2$	$M = 3$	$M = 4$	$M = 5$
Mean (P)	75.5	95.8	105.6	111.7	116.1
Median	76.2	86.6	88.9	90.4	91.5
Pr ($P \leq 100$)	0.93	0.89	0.86	0.84	0.82

Figure 6 shows the CDF of P for different values of M . Table 3 lists some of the quantities extracted from these CDFs. When a single antenna mode is employed, the mean maximum percentage difference is 75.5% and the probability of this percentage difference being greater than 100% is as low as 0.07. This observation clearly elucidates the challenge with designing a GLRT based detection scheme using a single antenna. Though the links can be differentiated in terms of σ , the amount of separation in σ_0 and σ_1 may not be sufficient in any given scenario for the GLRT to yield acceptable performance levels with a single antenna mode.

Figure 7 shows the variation of probability of detection as a function of detection delay in terms of number of packets. Understandably, detection rate improves with the allowable detection delay. However, it should be noted that timely detection of the intruder is very critical and therefore N_D cannot be increased to arbitrarily large values to achieve the required detection rates. Again, it can also be observed that the performance improves with block size. However, to be effective, higher values of N require that the detection delay to be at least as long as the block size so that the block will contain samples entirely from the intruder. The effect of

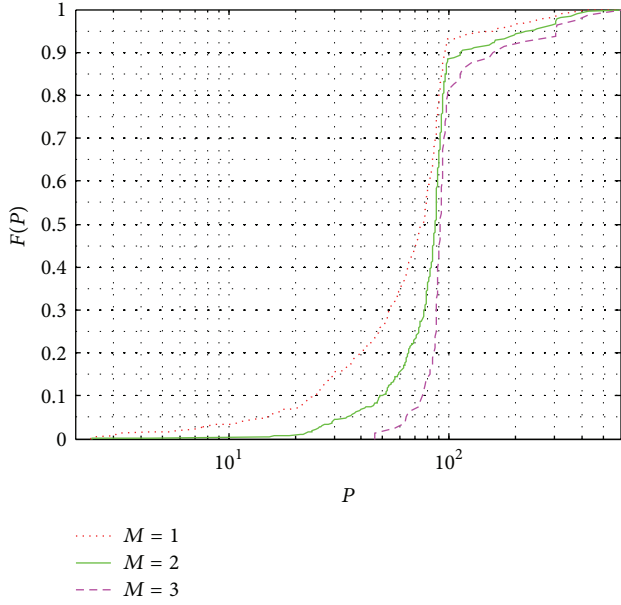


FIGURE 6: CDF of P for different values of M . The support and mean shifts toward higher values with increasing M .

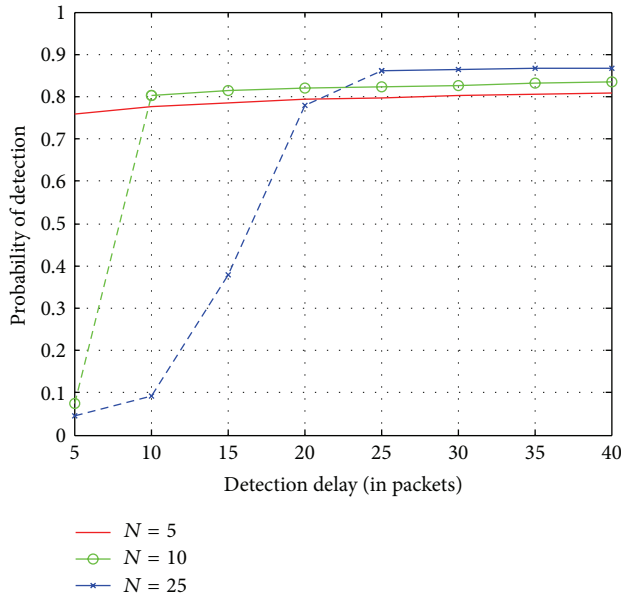


FIGURE 7: Variation of detection probability with N_D for a single antenna ($M = 1$) mode at $\alpha = 0.05$. $N_T = 25$. N_D is equal to N for each curve. The dashed segments correspond to points where $N_D < N$. Longer delays result in only marginal improvements in detection. Larger N improves performance, but the minimum required detection delay is longer for larger N 's.

N being less than the detection delay can be observed by the dotted lines in Figure 7 where the detection performance is significantly deteriorated.

The false alarm rate, as a function of the number of friendly transmissions from T before I takes over, is shown in Figure 8. As one would expect, the chances of raising a false

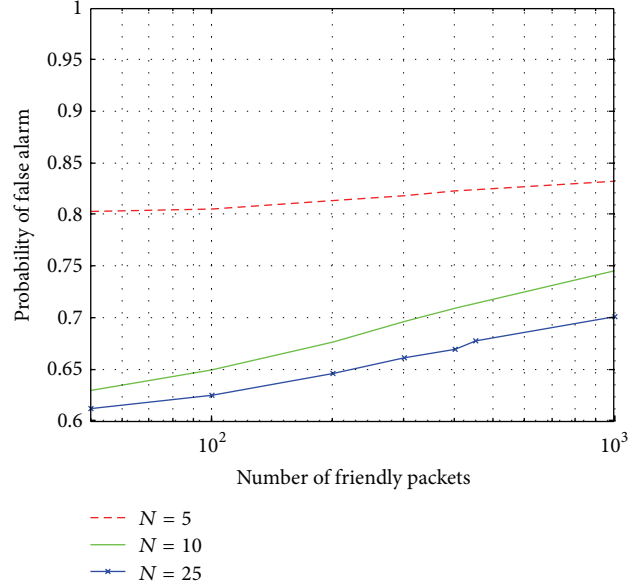


FIGURE 8: Variation of α with N_F for a single antenna ($M = 1$) mode at $\beta = 0.05$. $N_T = 25$. N_D is equal to N for each curve. Longer number of transmissions from T increases the probability of false alarms. Larger N improves performance due to better σ_0 estimates.

alarm rises with more friendly packets. A larger N results in a better estimate for σ_0 during the training phase. Additionally, it will yield a value for $\sigma(\mathbf{h})$ that is closer to the true σ_0 as well. Thus, the probability of $L(\mathbf{h})$ to exceed γ picked based on the estimated σ_0 will be lower and hence α improves with N .

To summarize the preceding trends, higher N lowers α while improving detection rates. Though a longer detection delay can help detection rates, in practice it is undesirable to have such long delays. However, due to the marginal difference between the σ values for the $T - R$ and $T - I$ links, it is challenging to obtain acceptable detection rates while keeping the false alarm rates very low when using a single mode antenna system. Hence, we resort to multimode antenna systems.

6.2. Multiple Antenna Modes. We begin our analysis of the multiple antenna mode case with Figure 9 which shows the DET curves achievable through the combination of channel information corresponding to multiple antenna modes. For each incoming packet, $L(\mathbf{h})$ is computed as in (7) based on the channel information corresponding to the chosen M configurations from which subsequent detection rates and false alarm rates are computed. It can be clearly seen that the detection rate significantly improves with the number of modes for a given α . Referring again to Figure 6 and Table 3, it can be observed that the maximum percentage difference between σ 's among the different antenna modes increases with M . This is by virtue of the fact that different antenna modes will exhibit different σ values and hence the probability that the difference between σ_0 and σ_1 is very small for all the modes will be lower. Thus, modes that exhibit a larger difference in σ will contribute more to the GLRT

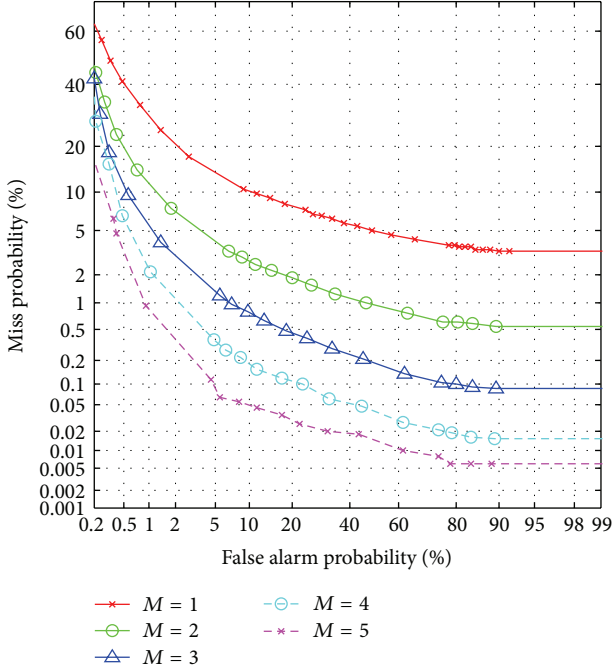


FIGURE 9: Average DET curves for a multiple antenna modes for $N = N_D = 10$, $N_T = 25$. For a given α , β decreases with increasing number of antenna modes. Acceptable levels of β can be achieved at low α levels by using multiple antenna modes.

resulting in better performance. Increasing M increases the probability of finding modes that exhibit a larger difference in σ 's and hence performance significantly improves with M . Again, due to the lower value of N , a non-Gaussian trend is observed in the observed DET curves.

Figure 10 shows the achievable detection rates as function of detection delay for the different M values. Comparing this with Figure 7, it can be seen that the level of improvement achievable in detection rates is quite high with M than N . For example, increasing N from 10 to 25 results in a mere 5% improvement in detection when a single mode is used. Moreover, this improvement comes at the cost of a longer detection delay. By introducing an additional mode, β can be lowered from around 20% to 9% while keeping N and N_D at 10.

Figure 11 shows α as a function of the number of friendly packets. As described in step (2) in Section 6, α is defined as the probability that there will be at least one packet that exceeds the threshold γ during the friendly transmissions. Improvements in α is also observed with increasing M . Naturally false alarms increase with increasing friendly packets regardless of M . For relatively smaller values of N and a single antenna mode, when certain samples in \mathbf{h} come from the tail region of the underlying Rayleigh distribution, the resulting estimate of $\hat{\sigma}_1$ can significantly diverge from σ_0 resulting in excursions of $L(\mathbf{h})$ above the threshold γ . However, when multiple antenna modes are employed, the probability that the channels corresponding to most of the modes belong to the tail region at any given instant is reduced. Therefore, at every time instant, the “well-behaved” modes help dampen

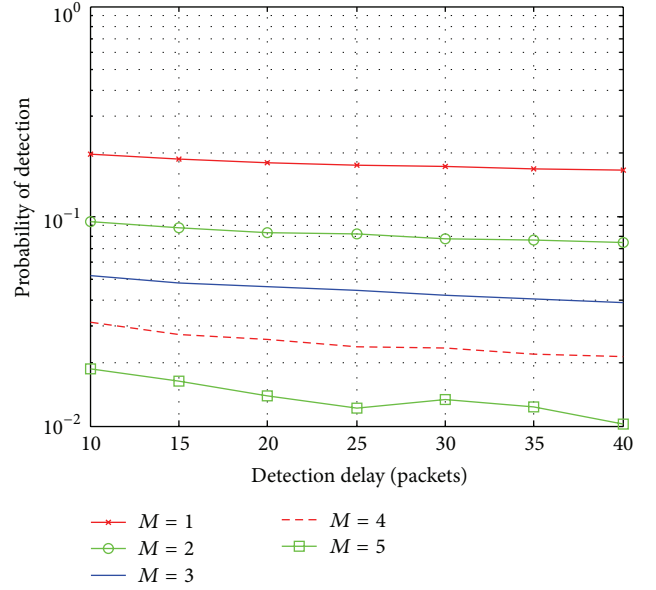


FIGURE 10: Variation of detection probability with N_D for multiple antenna modes at $\alpha = 0.05$, $N = N_D = 10$, $N_T = 25$. As observed in Figure 7, longer delays result in only marginal improvements in detection. More antenna modes however results in better detection rates without requiring longer detection delays.

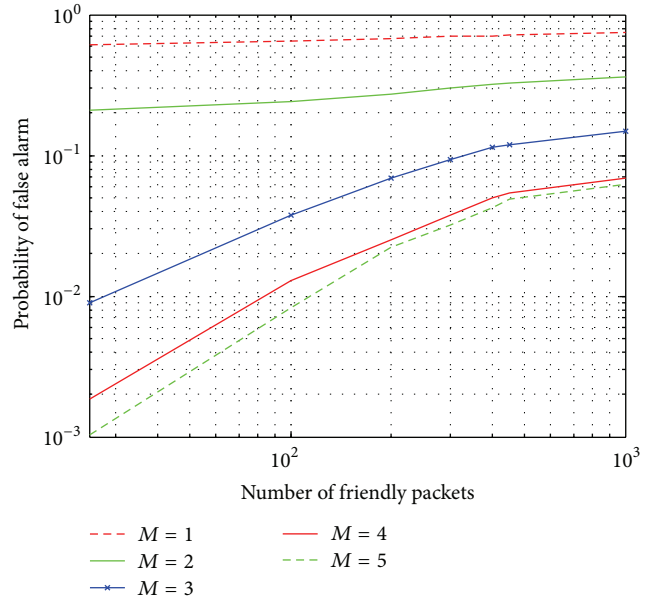


FIGURE 11: Variation of α with N_F for multiple antenna modes at $\beta = 0.05$, $N_T = 25$, N_D is equal to N for each curve. α decreases with M .

the hikes in $\hat{\sigma}_1$ due to the “stray” modes and therefore help keep the excursions of $\hat{\sigma}_1$ above γ low and hence reduce the probability of false alarm.

We conclude this section by providing a list of key statistical measures for α and β that were observed for various values of K in 100 trials. These measures are shown in Table 4. It can be observed that the standard deviation is

TABLE 4: Key statistical measures for α and β observed during 100 trials ($M = 5$, $N = 25$, $N_T = 25$, and $N_D = 1$).

K	α/β	Std. Dev.	Mean	Min	P_{25}	P_{50}	P_{90}	P_{99}	Max
1.00	α	0.00009	0.00005	0.00000	0.00000	0.00000	0.00020	0.00020	0.00020
	β	0.00000	1.00000	1.00000	1.00000	1.00000	1.00000	1.00000	1.00000
1.05	α	0.00010	0.00007	0.00000	0.00000	0.00000	0.00020	0.00020	0.00020
	β	0.01350	0.83669	0.80566	0.82646	0.83809	0.85381	0.85977	0.85977
1.10	α	0.00009	0.00006	0.00000	0.00000	0.00000	0.00020	0.00020	0.00020
	β	0.01593	0.73663	0.70234	0.72422	0.73994	0.75811	0.77676	0.78477
1.20	α	0.00010	0.00009	0.00000	0.00000	0.00000	0.00020	0.00020	0.00020
	β	0.01861	0.61567	0.57227	0.60215	0.61689	0.63965	0.64688	0.64863
1.40	α	0.00010	0.00014	0.00000	0.00000	0.00020	0.00020	0.00039	0.00039
	β	0.01630	0.44315	0.40430	0.43369	0.44453	0.46113	0.48057	0.48418
1.60	α	0.00010	0.00021	0.00000	0.00020	0.00020	0.00039	0.00039	0.00039
	β	0.01592	0.31338	0.27715	0.30293	0.30986	0.33535	0.35586	0.35820
1.80	α	0.00014	0.00026	0.00000	0.00020	0.00020	0.00039	0.00059	0.00059
	β	0.01575	0.22166	0.19629	0.21064	0.21768	0.24863	0.26113	0.26367
2.00	α	0.00015	0.00029	0.00000	0.00020	0.00020	0.00049	0.00059	0.00059
	β	0.01459	0.15741	0.13613	0.14590	0.15273	0.18145	0.19688	0.19707
2.25	α	0.00019	0.00037	0.00000	0.00020	0.00039	0.00059	0.00078	0.00078
	β	0.01265	0.10750	0.09004	0.09893	0.10361	0.12842	0.14385	0.14570
2.50	α	0.00024	0.00051	0.00020	0.00039	0.00059	0.00078	0.00098	0.00098
	β	0.00867	0.07441	0.06211	0.06992	0.07266	0.07998	0.10449	0.10488

TABLE 5: Pattern correlation coefficients between different modes of the LWA.

	Mode 1	Mode 2	Mode 3	Mode 4	Mode 5
Mode 1	1	0.73	0.42	0.10	0.06
Mode 2	0.73	1	0.82	0.27	0.07
Mode 3	0.42	0.82	1	0.55	0.11
Mode 4	0.10	0.27	0.55	1	0.56
Mode 5	0.06	0.07	0.11	0.56	1

limited to 1.5% for false alarm rates and to less than 1% for missed detection rates. The data shows that, for a given set of parameters, false alarm rates and missed detection rates are stable across multiple trials.

6.3. Which Modes to Choose? From the previous results it is clear that introducing multiple antenna modes improves the system's overall performance. However, these results do not provide insights into how to pick the mode combinations and most importantly if there is any benefit in increasing the number of modes beyond a certain level. Some insights into this problem can be found by analyzing Figure 12 and Table 5. Table 5 lists the spatial pattern correlation that exists between the radiation patterns corresponding to the different antenna modes used in the study. The best, worst, and average detection rates achieved by different individual mode combinations for $M = 2$ and $M = 3$ are shown in the figure. For $M = 2$, it is evident that the detection rate is a function of the antenna correlation coefficient. The best performance is achieved by the mode combination (5, 1) which also has the lowest correlation between patterns.

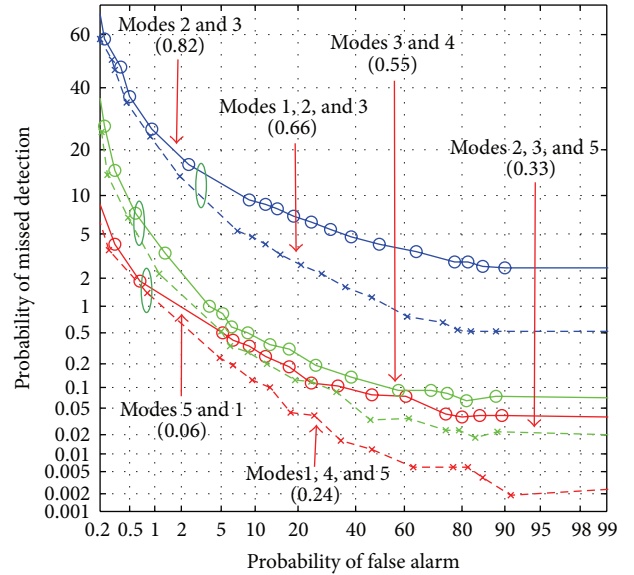


FIGURE 12: Average DET curves for different antenna mode combinations. $N = N_D = 10$. $N_T = 25$. Detection rates have a direct correlation with the correlation coefficient between the patterns of the employed antenna modes. For a given M , lower correlation coefficient between the antenna patterns results in better detection for a given α .

The combination with the highest correlation of 0.82 achieves the worst performance. Similarly, for $M = 3$, detection rates exhibit the same trend with respect to the average correlation between the different pair of modes within the combinations. Moreover, it can be seen that the performance achieved by

the best combination for $M = 3$ outperforms the $M = 5$ case as well.

The preceding behavior can be attributed to the well-known phenomenon of decorrelated antenna patterns resulting in decorrelated channel realizations [28]. The information provided by more decorrelated channel realizations serves to improve the “quality” of $L(\mathbf{h})$ and hence enables the scheme to distinguish between T and I more accurately.

Based on these trends, two guidelines are suggested for picking the different antenna modes. Antenna modes should be picked such that the pattern correlation coefficient between the different modes should be kept as low as possible. Many reconfigurable antenna architectures exist that can generate patterns with a very low correlation coefficient between their modes [19, 29]. The second is that adding new modes will improve detection rates as long as the newly introduced mode does not diminish the average correlation coefficient among the modes. This can be seen by observing the different circled pairs of DET curves in Figure 12, where adding a new mode improves detection when the addition of the mode lowers the average correlation coefficient among the modes.

6.4. Effect of Training. The quality of training will have a significant effect on the performance of the scheme as the estimated σ_0 forms the basis for the likelihood ratio based on which it operates. Figure 13 shows the effect of the amount of training on the DET curves. As evidenced by the figure, longer training leads to better performance at the lower α regions as expected. But interestingly more training has a negative effect on system performance at the larger α regions. Recall that the threshold γ is computed as $KL_M(\mathbf{h})$ where $L_M(\mathbf{h})$ is the maximum of $L(\mathbf{h})$ observed during training. Longer training on average leads to marginally larger values for $L_M(\mathbf{h})$. At high α regions, $K \approx 1$ and hence the threshold γ is more sensitive to $L_M(\mathbf{h})$. Therefore, for a given α , keeping all other parameters constant while increasing only N_T results in an increased estimate of the threshold γ , which in turn deteriorates detection. Although the estimate of σ_0 does improve with N_T , the increase in $L_M(\mathbf{h})$ outweighs its benefit in the high α region leading to performance degradation. Nevertheless, meaningful utilization of this scheme will involve operating in the low false alarm region and therefore longer training will be still preferred.

7. Practical Considerations

Some key practical issues need to be considered in order to make this scheme work in practice. The most critical issue is the problem of obtaining channel estimates over all the antenna modes on a packet-by-packet basis. Figure 14 shows the possible candidate for a frame structure at the physical layer that can be used to achieve this operation. An extended payload is interspersed with the necessary training symbols for each mode along with padded intervals to allow for switching the antenna to a new mode and resynchronization. High-speed switches with switching speeds in the order of picoseconds currently exist that can allow the antenna to

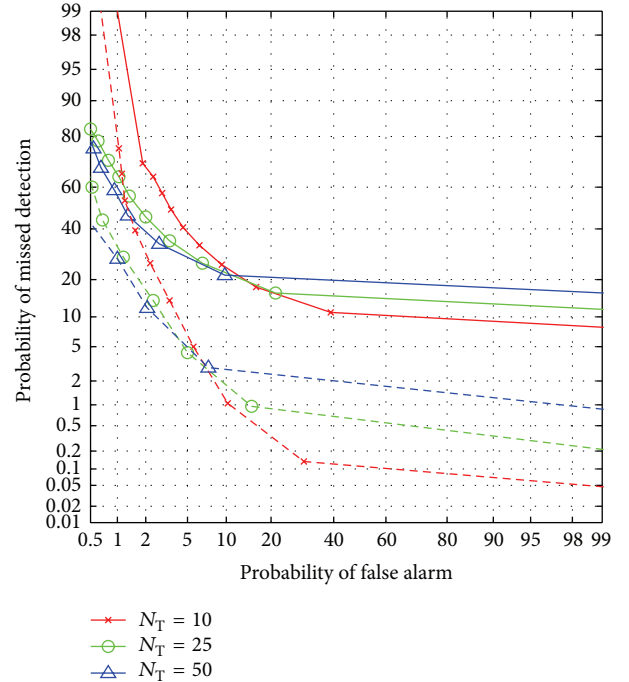


FIGURE 13: Average DET curves for $M = 1$ and $M = 5$ for different number of training samples. $N = N_D = 10$. Solid lines indicate $M = 1$ and dotted lines indicate $M = 5$. Longer training results in better detection at lower α regions. But the gains achieved from more training cannot match the gains achieved by employing more number of antenna modes.

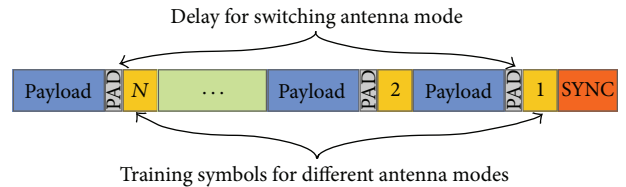


FIGURE 14: Extended transmit frame that can be used to obtain channel estimates for multiple antenna modes using a single packet transmission.

switch modes at a rate compatible with current high data rate applications.

As noted previously, this scheme is proposed to complement existing higher level security protocols. Therefore, such protocols should continue to play their role in protecting the wireless link. An adaptive approach can be pursued when the GLRT triggers an alarm at the physical layer. When an alarm is raised by the physical layer scheme, the system can reconfigure the GLRT to operate in a point on the DET curve that prioritizes low missed detection over false alarms. Subsequent alarms should be handled by the upper layer authentication protocols such as 802.11i till it is ensured that the perceived threat does not exist after which point the GLRT can prioritize over false alarms again. Moreover, successfully adapting the alarm threshold will also rely on these reauthentication protocols.

Channel statistics may also gradually change with time which can lead to arbitrarily high false alarm rates. Periodic retraining can be implemented to keep the system performance within acceptable levels. Therefore, this scheme can benefit from more comprehensive training algorithms that continually update σ_0 based on packets that pass the intrusion detection test at the physical as well as upper layers.

8. Conclusion

An intrusion detection scheme that utilizes physical layer information based on a reconfigurable antenna was proposed. The intrusion detection problem was setup as a generalized likelihood ratio test under the assumption of Rayleigh fading channels for different antenna modes. The assumption was justified based on channel measurements gathered in an indoor environment using a network analyzer. The measurements were then used to study the performance of the scheme as a function of several control parameters available to the user. It was observed that large block sizes lower false alarm rates while yielding high detection rates as well. By utilizing multiple modes in a reconfigurable antenna concurrently in the likelihood function, it was shown that the detection rates can be improved and false alarm rates can be decreased while keeping the block size low. The pattern correlation coefficient that exists between the radiation patterns of the different antenna modes was shown to have a direct correlation with the resulting detection performance, with lower pattern correlation resulting in better performance. In networks with very limited or nonexistent security such as public WiFi spots, the proposed scheme can add a layer of security that can provide improved levels of protection against intrusion. In more secure networks operating in hostile environments, this scheme in conjunction with existing higher layer based security mechanisms can provide a much needed extra layer of security.

Future work to make the scheme more robust includes smart training algorithms that continuously train the system and keep the system up-to-date as well as algorithms that adaptively tweak the different control parameters to keep the system operating at the required performance level.

Acknowledgment

This material is based upon work supported by the National Science Foundation under Grant no. 1028608.

References

- [1] R. K. Nichols and P. C. Lekkas, *Wireless Security: Models, Threats, and Solutions*, McGraw-Hill, New York, NY, USA, 2001.
- [2] W. A. Arbaugh, N. Shankar, Y. C. J. Wan, and K. Zhang, "Your 802.11 wireless network has no clothes," *IEEE Wireless Communications*, vol. 9, no. 6, pp. 44–51, 2002.
- [3] N. Borisov, I. Goldberg, and D. Wagner, "Intercepting mobile communications: the insecurity of 802.11," in *Proceedings of the 7th Annual International Conference on Mobile Computing and Networking (MobiCom '01)*, pp. 180–188, Rome, Italy, July 2001.
- [4] A. Kitaura and H. Sasaoka, "A scheme of private key agreement based on the channel characteristics in OFDM land mobile radio," *Electronics and Communications in Japan, Part III*, vol. 88, no. 9, pp. 1–10, 2005.
- [5] N. Patwari, J. Croft, S. Jana, and S. K. Kasera, "High-rate uncorrelated bit extraction for shared secret key generation from channel measurements," *IEEE Transactions on Mobile Computing*, vol. 9, no. 1, pp. 17–30, 2010.
- [6] S. Yasukawa, H. Iwai, and H. Sasaoka, "Adaptive key generation in secret key agreement scheme based on the channel characteristics in OFDM," in *Proceedings of the International Symposium on Information Theory and its Applications (ISITA '08)*, Auckland, New Zealand, December 2008.
- [7] S. Jana, S. N. Premnath, M. Clark, S. K. Kasera, N. Patwari, and S. V. Krishnamurthy, "On the effectiveness of secret key extraction from wireless signal strength in real environments," in *Proceedings of the 15th Annual ACM International Conference on Mobile Computing and Networking (MobiCom '09)*, pp. 321–332, Beijing, China, September 2009.
- [8] B. Azimi-Sadjadi, A. Kiayias, A. Mercado, and B. Yener, "Robust key generation from signal envelopes in wireless networks," in *Proceedings of the 14th ACM Conference on Computer and Communications Security (CCS '07)*, pp. 401–410, Alexandria, VA, USA, November 2007.
- [9] J. E. Hershey, A. A. Hassan, and R. Yarlagadda, "Unconventional cryptographic keying variable management," *IEEE Transactions on Communications*, vol. 43, no. 1, pp. 3–6, 1995.
- [10] M. Demirbas and Y. Song, "An RSSI-based scheme for sybil attack detection in wireless sensor networks," in *Proceedings of the International Symposium on a World of Wireless, Mobile and Multimedia Networks (WoWMoM '06)*, pp. 564–568, Buffalo-Niagara Falls, NY, USA, June 2006.
- [11] L. Xiao, L. J. Greenstein, N. B. Mandayam, and W. Trappe, "Using the physical layer for wireless authentication in time-variant channels," *IEEE Transactions on Wireless Communications*, vol. 7, no. 7, pp. 2571–2579, 2008.
- [12] L. Xiao, L. Greenstein, N. Mandayam, and W. Trappe, "Fingerprints in the ether: using the physical layer for wireless authentication," in *Proceedings of the IEEE International Conference on Communications (ICC '07)*, pp. 4646–4651, Glasgow, UK, June 2007.
- [13] D. B. Faria and D. R. Cheriton, "Detecting identity-based attacks in wireless networks using signalprints," in *Proceedings of the 5th ACM Workshop on Wireless Security (WiSE '06)*, pp. 43–52, Los Angeles, Calif, USA, September 2006.
- [14] L. Xiao, L. Greenstein, N. Mandayam, and W. Trappe, "MIMO-assisted channel-based authentication in wireless networks," in *Proceedings of the 42nd Annual Conference on Information Sciences and Systems (CISS '08)*, pp. 642–646, Princeton, NJ, USA, March 2008.
- [15] N. Patwari and S. K. Kasera, "Robust location distinction using temporal link signatures," in *Proceedings of the 13th Annual ACM International Conference on Mobile Computing and Networking (MobiCom '07)*, pp. 111–122, Montreal, Canada, September 2007.
- [16] L. Xiao, L. J. Greenstein, N. B. Mandayam, and W. Trappe, "Channel-based spoofing detection in frequency-selective Rayleigh channels," *IEEE Transactions on Wireless Communications*, vol. 8, no. 12, pp. 5948–5956, 2009.
- [17] Y. Zhang and W. Lee, "Intrusion detection in wireless ad-hoc networks," in *Proceedings of the 6th annual international*

- conference on Mobile computing and networking (MobiCom 00), pp. 275–283, 2000.
- [18] S. M. Kay, *Detection Theory*, vol. 2 of *Fundamentals of Statistical Signal Processing*, Prentice Hall, New York, NY, USA, 1998.
- [19] D. Piazza, P. Mookiah, M. D'Amico, and K. R. Dandekar, "Experimental analysis of pattern and polarization reconfigurable circular patch antennas for MIMO systems," *IEEE Transactions on Vehicular Technology*, vol. 59, no. 5, pp. 2352–2362, 2010.
- [20] E. Butler, "Firesheep 2011," <http://codebutler.com/firesheep>.
- [21] C. Oestges, D. Vanhoenacker-Janvier, and B. Clerckx, "Channel characterization of indoor wireless personal area networks," *IEEE Transactions on Antennas and Propagation*, vol. 54, no. 11, pp. 3143–33150, 2006.
- [22] P. Pagani and P. Pajusco, "Characterization and modeling of temporal variations on an ultrawideband radio link," *IEEE Transactions on Antennas and Propagation*, vol. 54, no. 11, pp. 3198–33206, 2006.
- [23] J. Medbo, J.-E. Berg, and F. Harrysson, "Temporal radio channel variations with stationary terminal," in *Proceedings of the IEEE 60th Vehicular Technology Conference, Wireless Technologies for Global Security (VTC '04)*, vol. 1, pp. 91–95, Los Angeles, Calif, USA, September 2004.
- [24] J. Sijbers, A. J. Den Dekker, E. Raman, and D. Van Dyck, "Parameter estimation from magnitude MR Images," *International Journal of Imaging Systems and Technology*, vol. 10, no. 2, pp. 109–114, 1999.
- [25] D. Piazza, M. D'Amico, and K. R. Dandekar, "Performance improvement of a wideband MIMO system by using two-port RLWA," *IEEE Antennas and Wireless Propagation Letters*, vol. 8, pp. 830–834, 2009.
- [26] J. Sijbers, A. J. Den Dekker, P. Scheunders, and D. Van Dyck, "Maximum-likelihood estimation of rician distribution parameters," *IEEE Transactions on Medical Imaging*, vol. 17, no. 3, pp. 357–361, 1998.
- [27] A. Martin, G. Doddington, T. Kamm, M. Ordowski, and M. Przybocki, "The DET curve in assessment of detection task performance," in *Proceedings of the 5th European Conference on Speech Communication and Technology (Eurospeech '97)*, vol. 4, pp. 1895–1898, Rhodes, Greece, 1997.
- [28] A. Forenza and R. W. Heath Jr., "Benefit of pattern diversity via two-element array of circular patch antennas in indoor clustered MIMO channels," *IEEE Transactions on Communications*, vol. 54, no. 5, pp. 943–954, 2006.
- [29] J. Kountouriotis, D. Piazza, K. R. Dandekar, M. D'Amico, and C. Guardiani, "Performance analysis of a reconfigurable antenna system for MIMO communications," in *Proceedings of the 5th European Conference on Antennas and Propagation (EUCAP '11)*, pp. 543–547, Rome, Italy, April 2011.

Research Article

Hardware Design of Seismic Sensors in Wireless Sensor Network

Gokhan Koc¹ and Korkut Yegin²

¹ KoçSistem Information Communication Services Inc., 34700 Istanbul, Turkey

² Department of Electrical and Electronic Engineering, Yeditepe University, 34755 Istanbul, Turkey

Correspondence should be addressed to Gokhan Koc; gokhan.koc@kocsistem.com.tr

Received 15 May 2013; Revised 8 August 2013; Accepted 25 August 2013

Academic Editor: Erdal Cayirci

Copyright © 2013 G. Koc and K. Yegin. This is an open access article distributed under the Creative Commons Attribution License, which permits unrestricted use, distribution, and reproduction in any medium, provided the original work is properly cited.

Seismic sensors are invaluable for intruder detection and perimeter security. In a typical wireless sensor network application of seismic sensors, the units are battery powered and low power consumption becomes critical while fulfilling system requirements. Although many systems utilize 24-bit ADC for seismic signal processing, we employed 12-bit ADC for low power consumption. Because of this relatively low resolution ADC, preamplifier and filters require careful hardware design. We employ bidirectional T-type filtering, noise reduction, and distributed filtering between gain stages before the signal is input to ADC. The proposed design was verified with measurements. Seismic data signals due to footsteps at varying distances were successfully measured.

1. Introduction

Seismic sensors in wireless sensor networks (WSNs) find increasing applications ranging from disturbance detection to critical compound security. Analog design of these sensor boards plays critical role in system performance as geophone sensors generate signal in microvolt's range. When geophone signal is amplified, filtered, and digitized, the data are usually transferred in WSN to a central processing unit. Although the design of wireless nodes has been matured to great extent such that there exist many integrated circuits (ICs) for transceivers, there is little known about the electronic design of the seismic sensor board. This study aims to bridge this gap by analyzing the sensor board requirements and electronic design steps. The design of a wireless node is also presented to fulfill low power requirements but not detailed as this design is relatively straightforward.

Human activities on ground generate vibrations from the point of contact as seismic waves. Seventy percent of those seismic vibrations are transmitted by Rayleigh waves which spread on the surface of the world. The remaining part of that energy is moved by body waves which spread perpendicularly to the Rayleigh waves [2, 3]. In order to detect humans and vehicles, Rayleigh waves can be very useful because of the transmission direction. Those vibrations

also have frequency-dependent attenuation characteristics [4]. In addition, ambient environment plays a crucial role in footstep and vehicle detection. For example, because of the increased seismic noise levels, detection distances are lowered during daytimes [5]. The relationship between the noise level and footstep detection distance is further examined in [6]. Another important parameter of the ambient environment is the vibration transmission filter of the ground. Vibration speed in the ground varies depending on the vibration frequency [7]. Footstep and vehicle vibration vary considerably according to these properties of environment and intruders. According to [8, 9], several important parameters of detection are footstep size and speed, shoes of the intruder, seismic noise at the background, unwanted targets, presence of residential buildings, generators, type of ground surface, air condition, geology, and soil conditions. Geophone sensors have several advantages in detecting footsteps and vehicle vibrations as they are less sensitive to Doppler effects of the environment variations than acoustic sensors, have the ability to work with no power (passive), and possess higher detection ranges relative to other sensors [9]. Generally two types of geophone sensors are used: single-axis and three-axis geophones. High bearing estimation error is usually the bottleneck of three-axis geophones. Also path tracking and bearing estimations in critical areas are more difficult

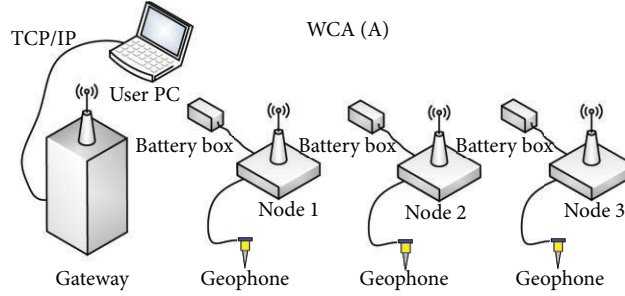


FIGURE 1: Seismic sensors in WSN.

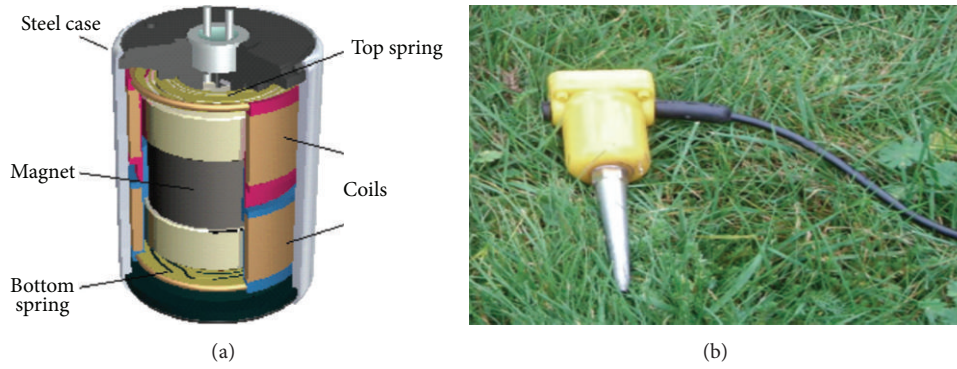


FIGURE 2: SM-24 geophone [1]: (a) representative view, (b) the unit.

by three-axis geophones than triangulation of single-axis geophones because geophone sensitivity is divided along all other axes [10].

Once seismic signal is detected and digitized, wireless sensor node is used to transmit the data for processing or transmitting low-level alarm generation as illustrated in Figure 1. One of the most important aspects of wireless sensor networks (WSN) is its power management. For example, in [11], 7.5 watt NI-PCI-6033E was used to detect footsteps with 16AH-5V battery. Extending systems lifetime without battery replacement is one of the key targets of any WSN. Several researches in WSN focusing on power efficiency were reported in [12–16]. Sensor board with wireless unit was described in [16] but the design lacks details on the amount of amplification, filtering, and noise reduction in the electronics. In this study, we present these details and provide board design with critical circuit components. Our design differs from earlier studies in terms of T-type filtering, noise reduction, and distributed filtering between gain stages before the signal is input to ADC. Low power consumption at every level is the key goal in our design.

2. Seismic Sensor Hardware Design

Most part of footstep vibration energy is distributed in the band from 10 to 100 Hz [3]. Thus, filters for the amplification of the signal must be of low pass filter type. Geophone sensor generates ultralow amplitude response (in microvolts) to human steps and vehicle movements. For signal processing

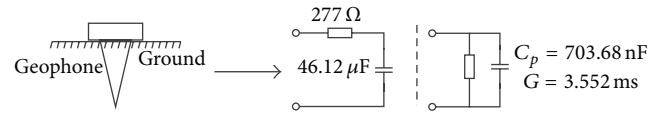


FIGURE 3: Equivalent circuit of SM-24 (measured using LCR-meter).

hardware, the amplitude of geophone sensor signal should be amplified with gain in excess of 1000. Low-level amplifications require high resolution ADC which also induces more noise. A typical geophone sensor is illustrated in Figure 2. Measurements of this sensor using LCR-meter have been carried out and an equivalent circuit as shown in Figure 3 has been formed for the design. The seismic sensor used in our study is SM-24, and its technical specifications are given in Table 1.

If we take 12-bit ADC at 3 V full-scale range, then ADC sensitivity is

$$\text{sensitivity}_{\text{ADC}} = \frac{3 \text{ V}}{2^{12} - 1} = 732.6 \mu\text{V}. \quad (1)$$

If amplification of 3000 is used, then 1-bit equivalent voltage at the input of the amplifier is

$$\text{sensitivity}_{\text{AMP}} = \frac{732.6 \mu\text{V}}{3000} = 244.2 \text{ nV}. \quad (2)$$

TABLE 1: Geophone SM-24 technical specifications [1].

	Values
Frequency	
Natural frequency	10 Hz
Tolerance	±2.5%
Maximum tilt angle for specified Fn	10°
Typical spurious frequency	>240 Hz
Distortion	
Distortion coil to case velocity with 17.78 mm/s (0.7 in/s) p.p.	<0.1%
Distortion measurement frequency	12 Hz
Damping	
Open circuit (typical)	0.25
Damping calibration-shunt resistance	1.339 ohm
Tolerance with calibration shunt	5%
Sensitivity	
Sensitivity	28.8 V/m/s (0.73 V/in/s)
Tolerance	±2.5%

Hence, the system sensitivity which is the particle velocity that corresponds to one bit of the ADC output is

$$\begin{aligned} \text{sensitivity}_{\text{System}} &= \frac{\text{sensitivity}_{\text{AMP}}}{\text{sensitivity}_{\text{GEOPHONE}}} \\ &= \frac{244.2 \text{ nV}}{28.8 \text{ V/(m/s)}} = 8.48 \text{ nm/s.} \end{aligned} \quad (3)$$

Therefore, in the absence of noise, a very slight movement in the ground with 8.48 nm/s can be resolved with this amplifier. The maximum value of velocity that puts ADC in its full scale is simply

$$\text{Max}_{\text{velocity}} = (2^{12} - 1) 8.48 \text{ nm/s} = 34.7 \text{ } \mu\text{m/s.} \quad (4)$$

Seismic sensor noise is mainly thermal noise that produces random voltage fluctuations. The noise voltage is given as

$$V_{\text{noise}} = \sqrt{4kTBR}, \quad (5)$$

where k is the Boltzman constant, T is temperature (K), B is the bandwidth, and R is the equivalent resistance of the sensor. Using measured equivalent circuit of the geophone with its cable and taking bandwidth 10 Hz as stated in the datasheet, the noise voltage becomes 66.4 μV . Component noise in the amplifiers, Op-amp noise, ADC noise, and power supply noise are all additives to total noise power. Thus, high level common-mode rejection ratio (at least 100 dB) Op-amps should be chosen and input of the amplifier should be noise matched with proper components. Board layout and component choices also play a critical role in the system noise. Power lines are usually the most common source of external noise induced at the sensor input.

System block diagram of the proposed seismic sensor is shown in Figure 4. First, the signal obtained from the

sensor is filtered (filter-1) and amplified by 10. Two-stage amplification has the advantage that the same total gain can be obtained with low-value resistors. Thus, noise from resistors is decreased, and signal-noise ratio is increased with filters placed between the amplifiers. The electronic design is detailed in Figure 5. In this design, C_5 capacitor removes unwanted offset value due to Op-amps. Another important point of this design is its dual-supply compatibility with wireless unit. ADC input can be easily corrupted due to dual power supply, and to prevent this, D_1 diode is used before the buffer block. So, the negative side of the amplified seismic signal is not transmitted to ADC input.

In high gain amplifier circuits, sometimes sensor signals leak to offset voltage which is generated by voltage reference integrated circuits or voltage dividers. If supply voltage has a DC bouncing or high frequency noises, all offsets would be affected. Because of this, signal from the sensor can be corrupted as well. This is a problem not only for signal processing but also for digital and analog circuits where DC voltage bouncing deteriorates circuit performance. However, it is not easy to eliminate DC bouncing on power lines. Filters on signal lines are used to eliminate high frequency noise only, and careful board layout minimizes the effects of DC bouncing. According to SM-24 geophone sensor, signal frequencies from natural activities would be under 100 Hz. Wireless communication, on the other hand, is implemented at 2.4 GHz. There is a huge frequency difference between signal and the wireless communication frequency. Thus, elimination of high frequency noise is not an issue.

Sharp filtering is also not a requirement for these applications. However, considering other possible noise sources, cut-off frequencies should be selected as close as possible to sensor signal but larger than the Nyquist sampling frequency. By looking at the frequencies, it is obvious that low pass filters must be used on signal lines. These passive components will be critical in general power consumption. Filters are implemented between the Op-amp circuit blocks so that they do not drive any load. However, higher filter input impedance will affect the total gain value indirectly. Directional filters would be more appropriate but difficult to implement. Instead, T-type filters, which have the same cut-off of frequencies in both directions, provide good isolation between the input and the output.

Since filter-1 is the most critical filter in the design, its PSpice simulation is shown in Figure 6. Overall circuit performance is illustrated in Figure 7.

3. Wireless Communication Unit

WSN includes sensor nodes and at least one gateway (gateways can be increased depending on coverage area). There are sensor board, sensor itself, battery box, wireless node, and 2.4 GHz antenna in each sensor node. There is no cable to connect the sensor nodes. They need a battery box for power. They make an alarm decision at the node and send only alarm information to gateway via wireless communication. The signal processing is performed at the node, but signal processing parameters such as duration thresholds, threshold

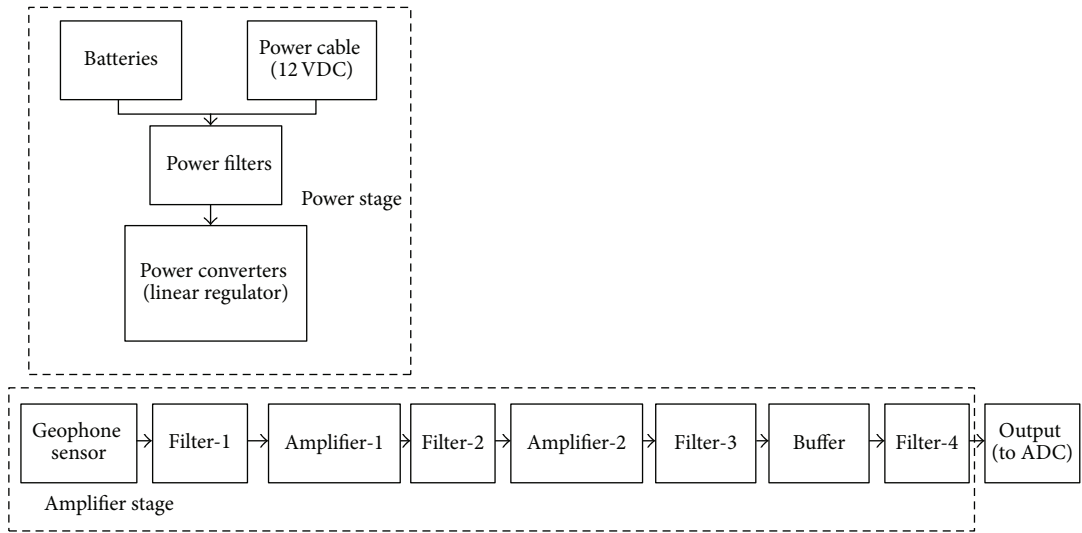


FIGURE 4: Block diagram of seismic sensor node.

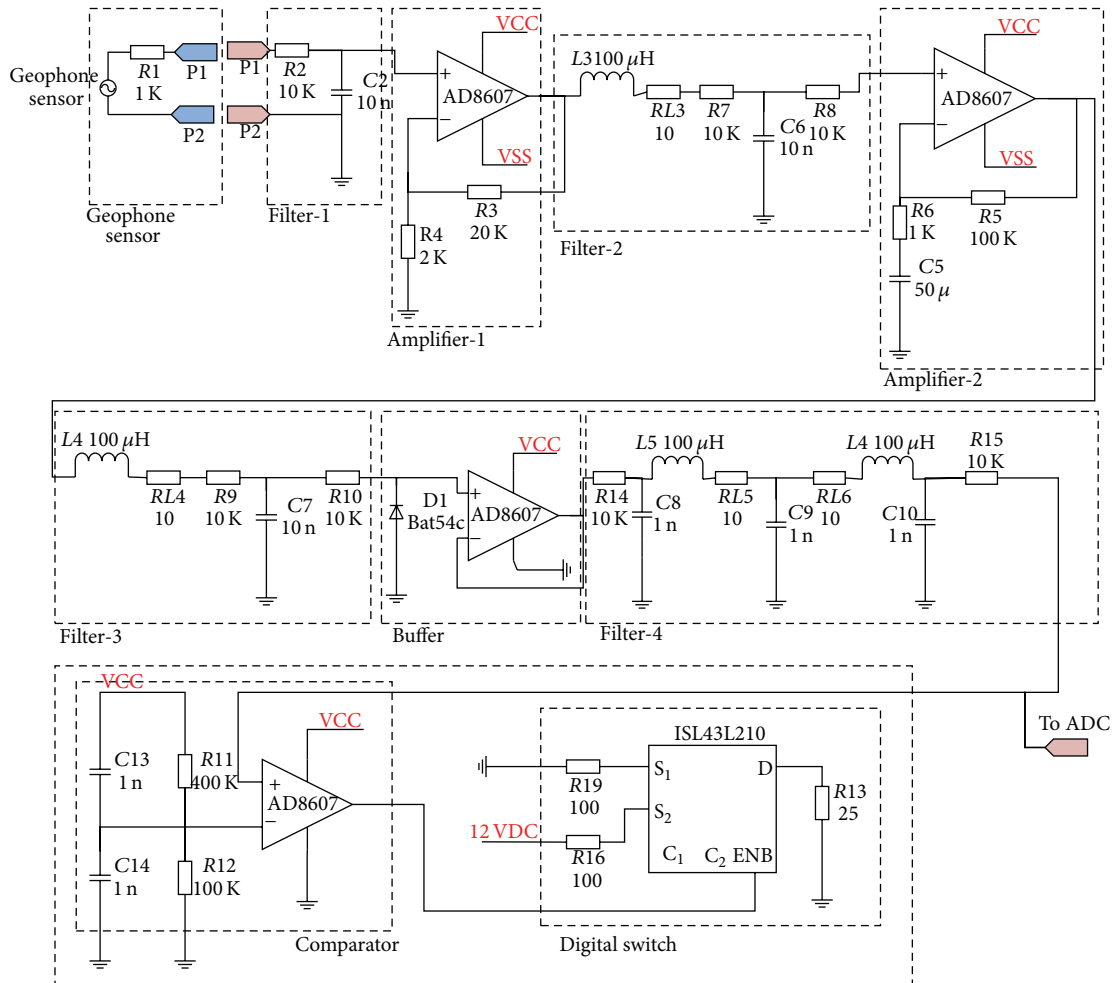


FIGURE 5: Seismic sensor board schematic.

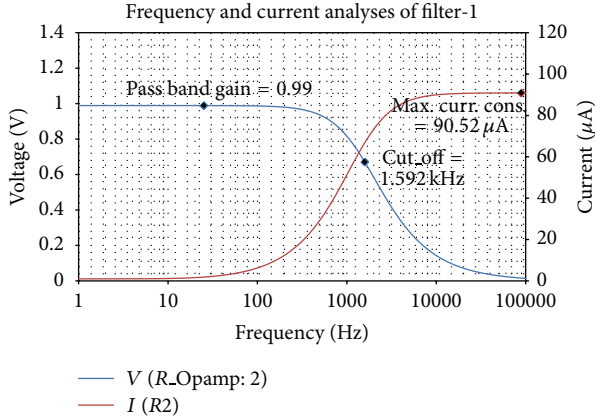


FIGURE 6: Filter-1 response.

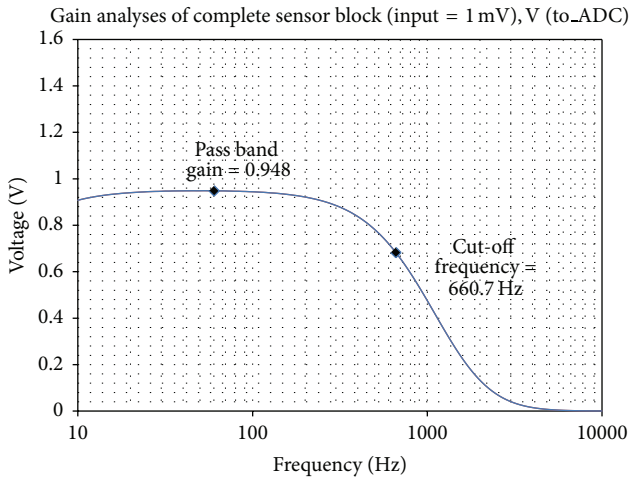


FIGURE 7: Overall circuit response.

memory sizes, and adjustable gain values at the Op-Amps can be modified remotely through wireless communication link. A typical application is shown in Figure 8.

The nodes automatically choose the most suitable and reliable way of communication for themselves through inter-communication with adjacent nodes. The nodes at both ends of each segment receive such data and transmit them to user by using conventional communication channels. Any gateway acts at the same time as the substitute of any other gateway, and, as it is the case for the detecting nodes, they substitute each other in their function in case of breakdown so that the probability of shut-down of the system due to any failure in any one of the gateways is minimized. Thus, this unique feature is an additional measure against any eventual tactical deception attempts.

The main properties of the two-way communication protocol are sleeping cycles, communication paths, and node-alive query. If an alarm condition occurs at a node, the node tries to deliver the corresponding alarm data to the gateway through other nodes. To reduce communication traffic and power consumption, relevant alarm data is transmitted over private path which is determined inside the node. Also,

TABLE 2: Wireless node technical specifications.

Wireless node	
Communication	
RF IC	TI CC2420
RF amplifier IC	TI CC2591
Central frequency	2.4 GHz
Channel number	16
Transmission rate	250 kbps
Maximum output power	16 dBm
Minimum output power	-25 dBm
Receive sensitivity	-98 dBm
MCU	
MCU	TI MSP430F1611
Operating system	Genos
Programmable flash memory	48 kB
Data RAM	10 kB
Serial ports	2x USART
Analogue digital converter	8-channel 12-bit

alternative paths are kept in the node to avoid problems that may arise due to the environment. This hopping technique and keeping backup path also prevent communication breaks against node breakdowns.

Technical specifications of the wireless node based on Texas Instruments (TI) ICs are summarized in Table 2.

Low power operation of the node is mainly due to the ultralow power microcontroller (TI MSP430 F1611) with 10 kB of RAM, 48 kB of flash, and 128 B of information storage. This 16-bit RISC processor features extremely low active and sleep current consumption that permits nodes to run for years on a single pair of AA batteries. The MSP430 has an internal digitally controlled oscillator that can operate up to 8 MHz. Our wireless node also has a second external crystal (8 MHz) for a more stabilized main clock. The MSP430 has 8 external ADC ports and 8 internal ADC ports. A variety of peripherals are available including SPI, UART, digital I/O ports, watchdog timer, and timers with capture and compare functionality. The F1611 also includes a 2-port 12-bit DAC module, supply voltage supervisor, and 3-port DMA controller.

The CC2420 is an IEEE 802.15.4 compliant radio providing the PHY and some MAC functions and can be controlled by MSP430 microcontroller through SPI port, digital I/O lines, and interrupts. The radio can be shut down by the microcontroller for low power duty cycled operation.

Wireless nodes can be powered by two AA batteries from two different input ports. While one of these inputs has direct connection to the system, the other input has a voltage matching circuit with stabilized output of 3.3 V for an input range of 0.6–3.6 VDC. Wireless node power specifications are given in Table 3.

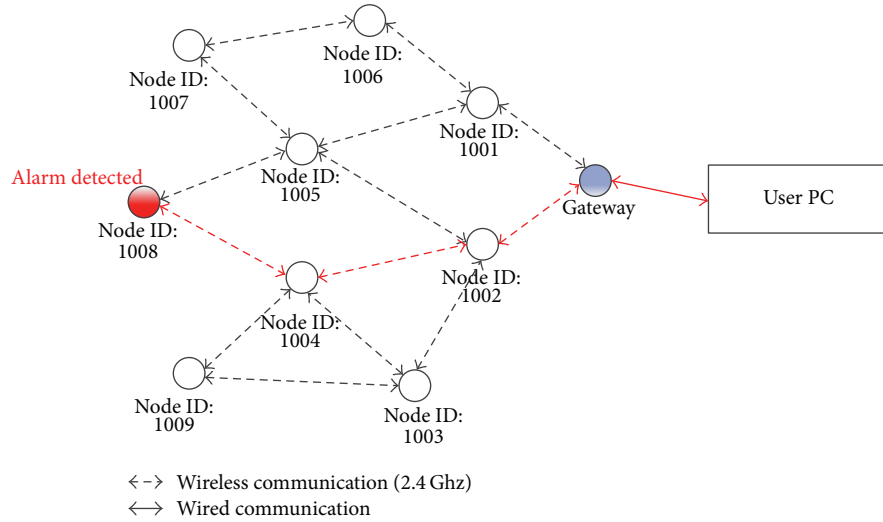


FIGURE 8: Typical WSN application.

TABLE 3: Wireless node power specifications.

	Min	Max	Unit
Supply voltage (J_1)	2.1	3.6	V
Supply voltage (J_2)	0.6	3.6	V
Supply voltage during flash memory programming (J_1)	2.7	3.6	V
Supply voltage during flash memory programming (J_2)	0.6	3.6	V
Operating temperature	-40	85	°C
Current consumption: MCU ON, radio RX	21.8	23	mA
Current consumption: MCU ON, radio TX	100.5	120	mA
Current consumption: MCU ON, radio OFF	1800	2400	μ A
Current consumption: MCU IDLE, radio OFF	54.5	1200	μ A
Current consumption: MCU STANDBY	<1		μ A

4. Realization and Measurements

The seismic sensor and wireless sensor boards are designed and built separately. The seismic sensor board is shown in Figure 9 where all blocks are labeled. This board is called daughter board and it is interfaced to the main board via 24-pin connector. The whole assembly is shown in Figure 10.

Amplifier 1 output and ADC input of the unit are measured via mixed-signal oscilloscope and the results are displayed in Figure 11. Recorded signal as a function of footstep range is shown in Figure 12.

5. Conclusion

Design of seismic sensor board coupled with a wireless node is detailed. The essential part of the design is its low power consumption due to relatively low resolution ADC. While similar designs utilize much higher resolution such as 24-bit, they consume too much power which makes them less preferable in a battery-powered wireless sensor network application. Our 12-bit ADC implementation requires careful preamplifier and filter designs. System sensitivity and maximum disturbance velocity are calculated. PSpice simulations

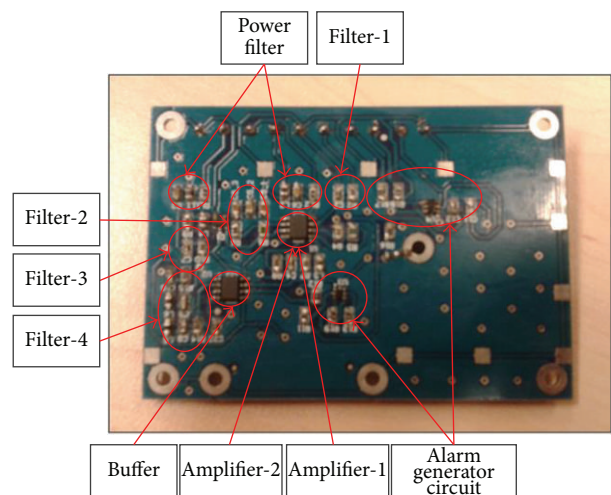


FIGURE 9: Seismic sensor board.

are run on the design to test the performance of the hardware. Prototypes are built and measured to observe the seismic

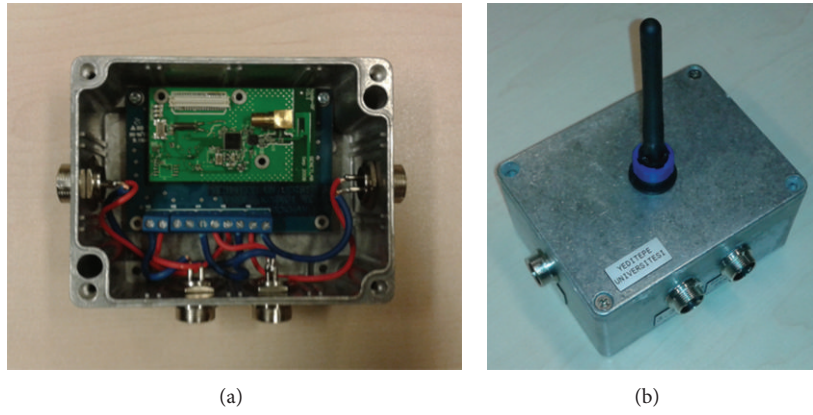


FIGURE 10: Whole unit: (a) interior side of the shielded box and (b) actual prototype.

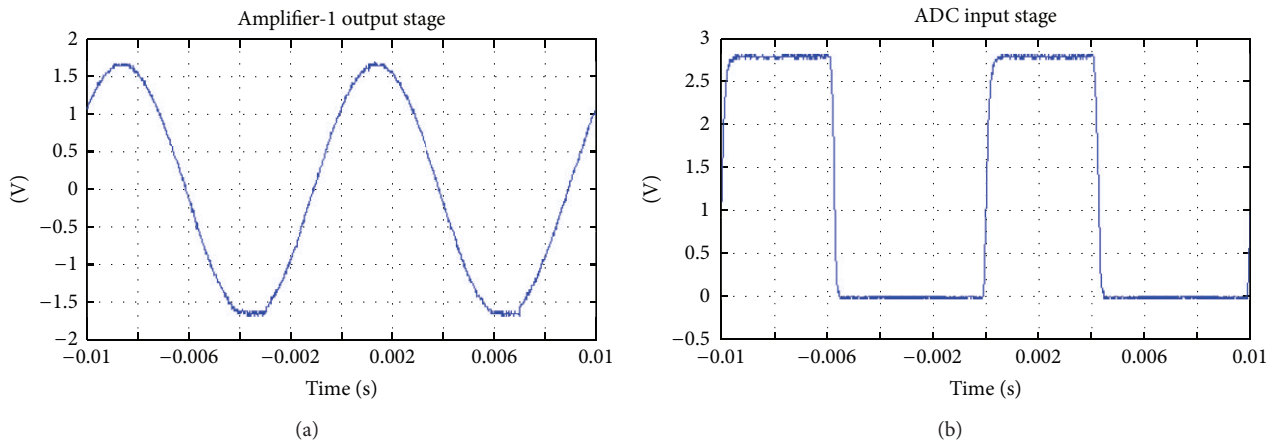


FIGURE 11: Oscilloscope measurements of the assembled unit: (a) amplifier-1 output and (b) ADC input.

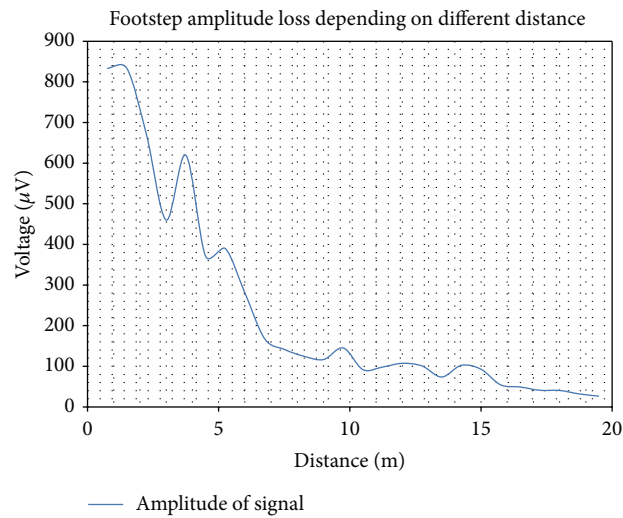


FIGURE 12: Footstep amplitude as a function of distance (normalized after 3 K gain).

signals due to footsteps at varying distances, and with as low as 3000 amplification, seismic signals above noise floor due to footsteps can be observed at 15 m.

References

- [1] Sensor Nederlands BV, "SM-24 geophone element," vol. 1, no. 1, 2006, http://www.globales.com/oem_brochures/SM-24-Brochure.pdf.
- [2] G. Succi, D. Clapp, R. Gampert, and G. Prado, "Footstep detection and tracking," in *Unattended Ground Sensor Technologies and Applications III*, vol. 4393 of *Proceedings of SPIE*, pp. 22–29, Orlando, Fla, USA, April 2001.
- [3] H. Amick, "A frequency-dependent soil propagation model," in *Proceedings of the SPIE Conference on Current Developments in Vibration Control for Optomechanical Systems*, Denver, Colo, USA, July 1999.
- [4] L. Peck, J. Gagnon, and J. Lacombe, "Seismic detection of personnel: field trials with REMBASS-II and Qual-Tron sensors," ERDC/CRREL TR-06-4, 2006.
- [5] H.-F. Xing, F. Li, and Y.-L. Liu, "Wavelet denoising and feature extraction of seismic signal for footstep detection," in *Proceedings of the International Conference on Wavelet Analysis and Pattern Recognition (ICWAPR '07)*, pp. 218–223, Beijing, China, November 2007.
- [6] M. S. Richman, D. S. Deadrick, R. J. Nation, and S. L. Whitney, "Personnel tracking using seismic sensors," in *Unattended Ground Sensor Technologies and Applications III*, vol. 4393 of *Proceedings of SPIE*, pp. 14–21, Orlando, Fla, USA, April 2001.
- [7] J. Lacombe, L. Peck, T. Anderson, and D. Fisk, "Seismic detection algorithm and sensor deployment recommendations for perimeter security," in *Unattended Ground, Sea, and Air Sensor Technologies and Applications VIII*, vol. 6231 of *Proceedings of SPIE*, Orlando, Fla, USA, April 2006.
- [8] A. Pakhomov, A. Sicignano, M. Sandy, and T. Goldburt, "Single and three axis geophone: footstep detection with bearing estimation, localization and tracking," in *Unattended Ground Sensor Tehnologies and Applications V*, vol. 5090 of *Proceedings of SPIE*, pp. 155–161, Orlando, Fla, USA, April 2003.
- [9] W. E. Audette, D. B. Kynor, J. C. Wilbur, J. R. Gagne, and L. Peck, "Improved intruder detection using seismic sensors and adaptive noise cancellation," in *Proceedings of the Human, Light Vehicle, and Tunnel Detection Workshop*, pp. 1–14, Hanover, Germany, June 2009.
- [10] L. Peck, J. Lacombe, and T. Anderson, *Seismic Detection of Personnel: Field Trials and Signatures Database*, Army Engineer Research and Development Center, Hanover, Germany, 2007.
- [11] R. S. Blum and S. A. Kassam, "Optimum distributed detection of weak signals in dependent sensors," *IEEE Transactions on Information Theory*, vol. 38, no. 3, pp. 1066–1079, 1992.
- [12] S. M. Kay, *Fundamentals of Statistical Signal Processing: Detection Theory*, Prentice-Hall, New York, NY, USA, 1998.
- [13] G. Succi, G. Prado, R. Gampert, T. Pedersen, and H. Dhaliwal, "Problems in seismic detection and tracking," in *Unattended Ground Sensor Technologies and Applications II*, vol. 4040 of *Proceedings of SPIE*, pp. 165–173, Orlando, Fla, USA, April 2000.
- [14] X. Jin, S. Gupta, A. Ray, and T. Damarla, "Multimodal sensor fusion for personnel detection," in *Proceedings of the 14th International Conference on Information Fusion, Fusion 2011*, pp. 437–444, Chicago, Ill, USA, July 2011.
- [15] A. Pakhomov and T. Goldburt, "Zero false alarm seismic detection and identification systems," in *Sensors, and Command, Control, Communications, and Intelligence (C3I) Technologies for Homeland Security and Homeland Defense V*, vol. 6201 of *Proceedings of SPIE*, Orlando, Fla, USA, April 2006.
- [16] A. Pakhomov and T. Goldburt, "New seismic unattended small size module for footstep and light and heavy vehicles detection and identification," in *Unattended Ground, Sea, and Air Sensor Technologies and Applications IX*, vol. 6562 of *Proceedings of SPIE*, Orlando, Fla, USA, April 2007.

Research Article

Circular Collaborative Beamforming for Improved Radiation Beampattern in WSN

N. N. Nik Abd Malik, M. Esa, S. K. Syed Yusof, S. A. Hamzah, and M. K. H. Ismail

UTM MIMOS CoE Telecommunication Technology, Faculty of Electrical Engineering, Universiti Teknologi Malaysia, 81310 Johor Bahru, Johor, Malaysia

Correspondence should be addressed to N. N. Nik Abd Malik; [noordini@fke.utm.my](mailto:oordini@fke.utm.my)

Received 1 March 2013; Revised 28 May 2013; Accepted 11 June 2013

Academic Editor: Adnan Kavak

Copyright © 2013 N. N. Nik Abd Malik et al. This is an open access article distributed under the Creative Commons Attribution License, which permits unrestricted use, distribution, and reproduction in any medium, provided the original work is properly cited.

This paper presents a novel collaborative beamforming (CB) method of wireless sensor network (WSN) by organizing sensor node location in a circular arrangement. Appropriate selection of active CB nodes and cluster is needed each time to perform CB. The nodes are modeled in circular array location in order to consider it as a circular antenna array (CAA). This newly proposed circular collaborative beamforming (CCB) is further presented to solve two different objectives, that is, sidelobe level (SLL) suppression and first null beamwidth (FNBW). Analyses obtained are compared to those from previous work. The findings demonstrate a better CB performance of intelligent capability, and the difference is shown in normalized power characteristic.

1. Introduction

Inside WSN environment, collaborative beamforming (CB) can be beneficial in increasing signal to noise ratio (SNR), thus boosting the energy efficiency of the system. In contrast with direct transmission transmitter-receiver or hop-by-hop transmission, CB spreads the energy consumption over multiple transmitters and improves the signal strength at the receiver [1]. Therefore, the CB nodes need less energy for data transmission, thus balance the energy consumptions, and desirably extend the network lifetime.

Works supporting sensor network in the literature, which utilizes wireless array, including [2–4] investigated usefulness of method and implementation schemes of a transmission array. Gaussian probability density function (pdf) is utilized to model the spatial distribution of sensor nodes in a cluster of WSNs [2] by proposing node selection algorithm [5]. The impact of Gaussian pdf as the spatial distribution is explored on the beampattern characteristic and compared with similar case when uniform pdf is used in [6]. The algorithm is developed to control the sidelobes by searching over different node combinations [7]. Ahmed and Vorobyov consider the

random nodes deployed in Gaussian pdf, while the proposed work considers the uniform random nodes distribution.

In spite of the significant contributions from previous literatures on CB, none of the works offer a CB by implementing circular antenna array (CAA). To the best of the authors' knowledge, this is the first work dealing with this problem. In this paper, the circular array technique is specially designed for WSNs with intelligent capability. The conventional uniform circular antenna array (UCA) may not be directly applied in WSN as it requires the exact location of elements in circular arrangement, a requirement that does not conform with random distribution nature of sensor nodes. Therefore, this is the main challenge of adapting this CAA into the context of WSN environment.

This paper presents a novel method of optimizing sensor node location in a circular arrangement. In this problem, the appropriate selection of active CB nodes and cluster is needed at each time to perform CB in WSN. The nodes are modeled in circular array location in order to consider it as a CAA. In the preliminary version of this work [8], it is shown that the linear sensor nodes array (LSNA) is able to achieve a desirable adaptive beampattern with

narrow main lobe and acceptable sidelobes level (SLL). Novel concept is offered with regard to intelligently optimizing and locating the selected sensor nodes to participate and form an array of sensor nodes. The concept is extended here through an alternate approach which employs hybrid least-square speedy particle swarm optimization-based circular collaborative beamforming (HLPSO-based CCB). The earlier work is reported in [9]. The biologically-inspired algorithm of particle swarm optimization (PSO) algorithm is improved and utilized to select the optimum nodes to participate in CB. The objective is to keep the main advantages of the standard PSO, such as simple implementation, low algorithmic complexity, and few control parameters, while maintaining the performance. Therefore, the proposed HLPSO characteristics are particularly attractive for WSNs since the computational resources such as memory and energy are limited.

The main idea in the proposed method is the desired objectives of radiation beampattern with minimum SLL and controllable size of FNBW. The proposed intelligent method of HLPSO-based CCB for determining optimum location of sensor node is proved superior to alternate techniques in terms of the normalized power gain with desired objectives. Up to date, an intelligent approach to determine optimum sensor nodes location to participate in wireless array network by employing bioinspired algorithm has not been reported or published so far by other authors.

2. The Network and Geometrical Array Model

2.1. The Network Model. WSN consists of a large number of sensor nodes in random deployment, which are wirelessly connected. The nodes are self-organized and are in connection with a controlling station as described in [10]. Each sensor node's location is determined using location discovery techniques [11] and is reported back to the controller. The central processor in a controlling station has detailed knowledge of each sensor node's location. It is also capable of selecting the appropriate manager node (MN), thus active cluster (AC) as per user requirement. Each sensing node, S_z is able to sense the environment and collect its own data. The selected MN gathers the data from the sensing nodes and then multicasts a final data packet to all the selected collaborative sensor nodes, that is, active CB nodes. The data from these sensing nodes are aggregated at the MN and only the needed information will be multicast. The active CB nodes will collaboratively transmit the same data in a synchronous manner. These active CB nodes, which perform as a CAA, have the possibility to form a narrow highly directive beam to the intended target point, where the receivers may be placed in order to collect all the transmitted data sent by collaborative nodes.

2.2. The Geometrical Array Model. The collaborative array antenna radiates power in all directions; hence, the simulation work should be in 3-dimensional scope. It is assumed that all sensor nodes are located on a 3-dimensional x - y - z plane. Consider a 3-dimensional characteristic of N -element CAA placed at the x - y plane. Assume $z = 0$; therefore the

plane is visualized to run parallel to the earth's surface. The array factor (AF) of the CAA [12] is given by

$$\begin{aligned} \text{AF}(\theta, \phi) &= \sum_{n=1}^N e^{j[\kappa r_n \sin \theta \cos(\phi - \phi_n) + \alpha_n]}, \\ \alpha_n &= -\kappa r_n \sin \theta_0 \cos(\phi_0 - \phi_n), \\ r_n &= \sqrt{(x_n)^2 + (y_n)^2}, \\ \phi_n &= \tan^{-1} \left(\frac{y_n}{x_n} \right), \end{aligned} \quad (1)$$

where N , κ , θ , ϕ , x_n , and y_n are the number of elements, wavenumber $\kappa = 2\pi/\lambda$, elevation angle, azimuth angle, x -coordinate, and y -coordinate (x_n , y_n) of the n th element, respectively. θ_0 and ϕ_0 are the maximum radiation angles. The normalized power gain, G_{norm} , in decibel is as stated in

$$G_{\text{norm}}(\theta, \phi)_{\text{dB}} = 10 \log_{10} \left[\frac{|\text{AF}(\theta, \phi)|^2}{\max |\text{AF}(\theta, \phi)|^2} \right]. \quad (2)$$

3. Hybrid Least-Square Speedy Particle Swarm Optimization (HLPSO)

PSO is applied to determine the optimum distance location of the nodes, which performs the highest performance as refer to objective scopes. Some improvements have been adopted in original PSO [13] in order to overcome the weaknesses and to adapt the algorithm inside WSNs environment. The novel HLPSO is proposed by integrating two novel mechanisms, that is, constraint boundaries variables and particle's position and velocity reinitialization. Moreover, the least-square approximation algorithm (LS) is integrated into it to improve the effectiveness and the capabilities of PSO in CCB application.

3.1. Global Constraint Boundaries Variables. Two sets of global constraint boundaries variables for lower boundary L and upper boundary U for different position particles, d_{s1} and d_{sn} ($n = 2, 3, \dots, N$), are adopted and represented as

$$\begin{aligned} L_1 &\leq d_{s1} < U_1, \\ L_N &\leq d_{sn} < U_N. \end{aligned} \quad (3)$$

These two boundaries are applied to restrict d_{s1} and d_{sn} to stay inside the solution space. Additionally, maximum upper limit and minimum lower limit are also assimilated inside this proposed HLPSO, that is, U_{max} and L_{min} , respectively. These two limits are determined before the computation of the objective function, of , in order to enhance the diversity

of the particle's searching abilities to be more global and freedom. Thus, it is expressed as

$$d_{s1} = \begin{cases} d_{s1} = L_1 \xrightarrow{\text{yields}} of(L_1), & \text{if } d_{s1} > U_{\max}, \\ d_{s1} = d_{s1} \xrightarrow{\text{yields}} of(d_{s1}), & \text{if } L_{\min} \leq d_{s1} < U_{\max}, \\ d_{s1} = L_1 \xrightarrow{\text{yields}} of(L_1), & \text{if } d_{s1} \leq L_{\min}, \end{cases}$$

$$d_{sn} = \begin{cases} d_{sn} = L_N \xrightarrow{\text{yields}} of(L_N), & \text{if } d_{sn} > U_{\max}, \\ d_{sn} = d_{sn} \xrightarrow{\text{yields}} of(d_{sn}), & \text{if } L_{\min} \leq d_{sn} < U_{\max}, \\ d_{sn} = L_N \xrightarrow{\text{yields}} of(L_N), & \text{if } d_{sn} \leq L_{\min}. \end{cases} \quad (4)$$

3.2. Particle's Position and Velocity Reinitialization. The random numbers of particle position d_{sn} can be a factor of the particle's tendency to leave the initially defined search space. Therefore, a modification based on the absorbing wall conditions by [14] is implemented in this algorithm. In order to control the movement of particle from flying outside the border of the search space, the velocity v_{sn} is zeroed whenever the particle d_{sn} goes over the boundaries U_N and L_N . However, the particle d_{sn} is then pulled back inside the search space by reinitializing it as random numbers r generated from the values of $[L_{\min}, U_{\max}]$. The objective of this reinitialization of d_{sn} is to prevent the particle from being stuck in local optima scenario where the particle is trapped and inhibited to search for a better solution. By introducing the reinitialization, a more flexible and comprehensive searching can be done by the particle with noted limitations, as expressed by

$$v_{sn} = \begin{cases} v_{sn} = 0 \longrightarrow d_{sn} = r [L_{\min}, U_{\max}], & \text{if } d_{sn} > U_N, \\ v_{sn} = v_{sn}, & \text{if } L_N \leq d_{sn} < U_N, \\ v_{sn} = 0 \longrightarrow d_{sn} = r [L_{\min}, U_{\max}], & \text{if } d_{sn} \leq L_N. \end{cases} \quad (5)$$

By using (5), the particle movement may be triggered again so that it has the highest probability to search for the optimum global best. In addition, the particle position is also forced to stay inside the upper boundary U and lower boundary L as denoted by following equations:

$$d_{s1} = \begin{cases} d_{s1} = U_1, & \text{if } d_{s1} > U_1, \\ d_{s1} = d_{s1}, & \text{if } L_1 \leq d_{s1} < U_1, \\ d_{s1} = L_1, & \text{if } d_{s1} \leq L_1, \end{cases}$$

$$d_{sn} = \begin{cases} d_{sn} = U_N, & \text{if } d_{sn} > U_N, \\ d_{sn} = d_{sn}, & \text{if } L_N \leq d_{sn} < U_N, \\ d_{sn} = L_N, & \text{if } d_{sn} \leq L_N. \end{cases} \quad (6)$$

The integration of the LS approximation algorithm in this HLPSON is required so that the desired radiation beampattern performance can be closely approximated to the desired beampattern results. Due to the random spatial positioning of

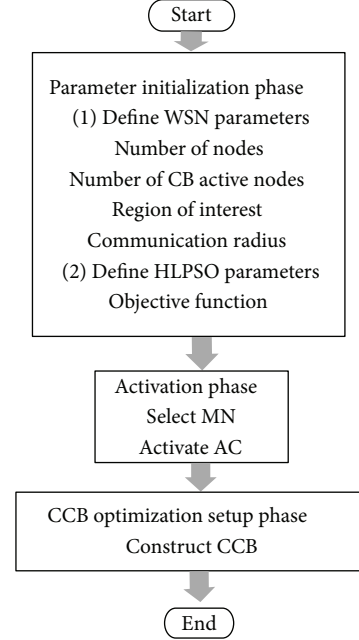


FIGURE 1: Flow chart for HLPSON-based CCB.

nodes, LS algorithm provides the ability to alter and create a radiation beampattern by introducing weights on each node. The determination of the weights allows elimination of the effect of random nodes position errors in WSNs. The effect of weights can be removed through equalization.

3.3. Hybrid Least-Square Particle Swarm Optimization-Based Circular Collaborative Beamforming (HLPSON-Based CCB). The proposed network model of HLPSON-based CCB consists of a random deployment of Z stationary sensor nodes inside the region of interest of $\Lambda \text{ m}^2$, which are organized in a different cluster. Each node is denoted in Cartesian coordinates of (x_k, y_k) with k representing the number of nodes. Each cluster has an MN designated as the leader, which manages in searching and selecting only the participating CB active nodes to form the HLPSON-based CCB in circular arrangement. The MN also acts as the centre of the CCB, but it is not participating in the CAA construction. Therefore, MN organizes a subset of its cluster nodes into a distributed CCB, $M_n = (m_1, m_2, \dots, m_N)$ coordinating their transmissions to direct the main beam towards the receivers.

There are three phases in HLPSON-based CCB: parameter initialization, activation, and optimization setup phases. The flow chart for the three phases of HLPSON-based CCB has been shown in Figure 1. A description of each follows.

3.3.1. Parameter Initialization Phase. The initial parameters for WSNs environment are listed in Table 1.

The proposed HLPSON manages to search for the optimum element distance of CCB and deal with the desired objectives. The desired parameters for HLPSON are illustrated in Table 2. These parameters are initialized by referring to the desired objectives of the organization scheme.

TABLE 1: Parameters and values of 8-node CCB.

Parameters	Symbol	Values
Number of all nodes	Z	900 nodes
Area of interest	Λ	900 m ²
Density	ρ	1 node/m ²
Manager node	MN (x_{MN}, y_{MN})	(14.51, 20.91)
Area of active cluster	X	123 m ²
Nodes inside active cluster	Z_S	119
UCA radius	r^{UCA}	2.5464 m
CCB radius	r^{CCB}	2.9421 m

TABLE 2: List of parameters used in HLPSON implementation.

Parameters	Symbol	Value
Number of particles	S	30
Dimension of particles	N	8
Iterations	It	500–1000
Range of particles	D	0 to $2\lambda_O$
Upper boundary for d_n	U_N	$2.2\lambda_O$
Lower boundary for d_n	L_N	$0.1\lambda_O$
Maximum upper limit	U_{max}	$0.1\lambda_O$
Maximum lower limit	L_{min}	$2.5\lambda_O$
Velocity	V	0 to 0.2
Learning factors	$c_1 = c_2$	2.0
Maximum weight	ω_{max}	0.9
Minimum weight	ω_{min}	0.4

3.3.2. *Activation Phase.* MN with coordinates of (x_{MN}, y_{MN}) is activated which has the most neighbor nodes within its communication radius, C . Then, the AC area, Xm^2 , is determined by referring to the MN as the centre of the X . The total number of nodes, Z_S , within X is activated.

3.3.3. *CCB Optimization Setup Phase.* The procedures needed to formulate this CCB optimization setup scheme are described as follows.

Step 1. Construct the virtual circle with C radius by referring to MN as the center of the circle.

Step 2. Establish HLPSON algorithm to optimize the sensor node location.

Step 2(a). Initialize HLPSON parameters.

Step 2(b). Generate random initial location, d_{sn} , $[d_{sn}] = [d_{s1}, d_{s2}, d_{s3}, \dots, d_{sN}]$ and velocity, v_{sn} , $[v_{sn}] = [v_{s1}, v_{s2}, v_{s3}, \dots, v_{sN}]$ for each particle, where N and s are the dimensional problem and number of particles, respectively.

Step 2(c). Calculate the objective function, that is, of , where of_{SLL} is the objective function of SLL minimization term as defined in

$$of_{SLL}(\theta_{SLL}) = \sum_{SLL_1=1}^{MaxSL} |AF(\theta_{SLL_1})|_{dB} + \sum_{MinSL}^{SLL_2=181} |AF(\theta_{SLL_2})|_{dB}, \quad (7)$$

where θ_{SLL_1} and θ_{SLL_2} are the angles, where the SLL is minimized in the lower band (from $\theta_{SLL_1=1}$ to $\theta_{SLL_1=MaxSL}$) and in the upper band (from $\theta_{SLL_2=MinSL}$ to $\theta_{SLL_2=181}$), respectively. of_{bw} is the objective function FNBW term as defined in

$$of_{bw}(\theta_{bw}) = \sum_{bw=bw1}^{bw2} |AF(\theta_{bw})|_{dB}, \quad (8)$$

where θ_{bw} is the angle of desired FNBW; that is, FNBW = $\theta_{bw2} - \theta_{bw1}$ which is the range of angles of the major lobe.

Step 2(d). Determine the previous best location, $pbest$, $P = [p_s] = [p_1, p_2, p_3, \dots, p_s]$. Set $of(p_s)$ value to be equal to $of(d_{sn})$.

Step 2(e). Determine the global best position, $G = [g_n] = [g_1, g_2, g_3, \dots, g_N]$. Set $g_n = \min(p_s)$ or $g_n = \text{optimum}(p_s)$.

Step 2(f). Update v_{sn} :

$$v_{sn}(\tau + 1) = \omega v_{sn}(\tau) + c_1 r_1 [p_s(\tau + 1) - x_{sn}(\tau)] + c_2 r_2 [g_n(\tau + 1) - x_{sn}(\tau)], \quad (9)$$

where c_1 and c_2 are acceleration constants and r_1 and r_2 are uniformly distributed numbers in $[0, 1]$. $\tau + 1$ and τ refer to the time index of the current and previous iterations. ω is the inertial weight factor. Then, limit V using (5).

Step 2(g). Update d_{sn} :

$$d_{sn}(\tau + 1) = d_{sn}(\tau) + v_{sn}(\tau + 1) \quad (10)$$

and limit D of the particles by using (6).

Step 2(h). Update $pbest$ as follows.

If $of(d_{sn})$ is better than $of(p_s)$, then update p_s and store $d_{sn}(p_s)$.

Step 2(i). Update $gbest$ as follows.

If $of(p_s)$ is better than $of(g_n)$, then update g_n and store $d_{sn}(g_n)$.

Step 2(j). If the maximum iteration number is met, terminate the algorithm, otherwise, proceed to Step 2(c).

Step 3. Construct CAA by using the distance result d_{sn} from the HLPSON algorithm. The constructed CAA is assumed with N -node with spacing distance of d_{sn} . The sensor node location of x - and y -coordinates, $B_n(x_n^B, y_n^B)$, is referring to the values of d_{sn} .

Step 3(a). Calculate the radius, r^d , from d_{sn} by using

$$r^d = \frac{\sum_{n=1}^N d_{sn}}{2\pi}. \quad (11)$$

Step 3(b). Calculate phase ϕ_n for every d_{sn} ($n = 1, 2, \dots, N$). These r^d and ϕ_n values are the polar coordinates of HLPSON optimized location of sensor nodes, $B_n(r^d, \phi_n)$. The ϕ_n is calculated using

$$\phi_n = \frac{(2\pi \sum_{n=1}^N d_{sn})}{\sum_{n=1}^N d_{sn}}. \quad (12)$$

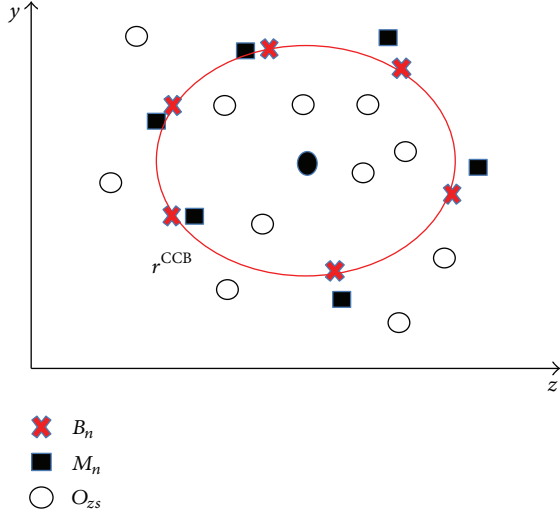


FIGURE 2: Locations of B_n , O_{zs} , and M_n with radius of r^{CCB} .

Step 3(c). Convert the polar coordinates $B_n(r^d, \phi_n)$, to the Cartesian coordinates, $B_n(x_n^B, y_n^B)$ by using

$$\begin{aligned} x_n^B &= (r^d \cos \phi_n) + x_{\text{MN}}, \\ y_n^B &= (r^d \sin \phi_n) + y_{\text{MN}}, \end{aligned} \quad (13)$$

where $(x_{\text{MN}}, y_{\text{MN}})$ are the coordinates of MN.

The construction of this optimum CAA is illustrated in Figure 2. The MN is located at the centre of B_n ; however MN does not participate in this CAA. Virtual circle for B_n is constructed with a radius of r^{CCB} .

Step 3(d). Determine the normalized gain, G_{norm}^B , by using (2).

Step 4. Start searching CCB nodes.

Step 4(a). Select the minimum Euclidean distance, d_n^{min} , between $B_n(x_n^B, y_n^B)$ and the nearest node inside AC, $O_{zs}(x_{zs}^O, y_{zs}^O)$,

$$\min \left\{ \sqrt{[(x_n^B - x_{zs}^O)^2 + (y_n^B - y_{zs}^O)^2]} \right\} = d_n^{\text{min}} \quad (14)$$

with $zs = 1, 2, \dots, ZS$ nodes inside AC.

Step 4(b). Choose the O_{zs} which has d_n^{min} with coordinates (x_{zs}^O, y_{zs}^O)

Step 4(c). Activate O_{zs} and appoint it as an optimum CCB. CCB is represented as $M_n(x_n^M, y_n^M)$, $M_n \in O_{zs}$. The mapping process is illustrated in Figure 2.

Step 4(d). This set of optimal CCB will be performed collaboratively as an N -element distributed CAA.

Step 5. Determine normalized gain, $G_{\text{norm}}^{\text{CCB}}$, of final CCB using (2).

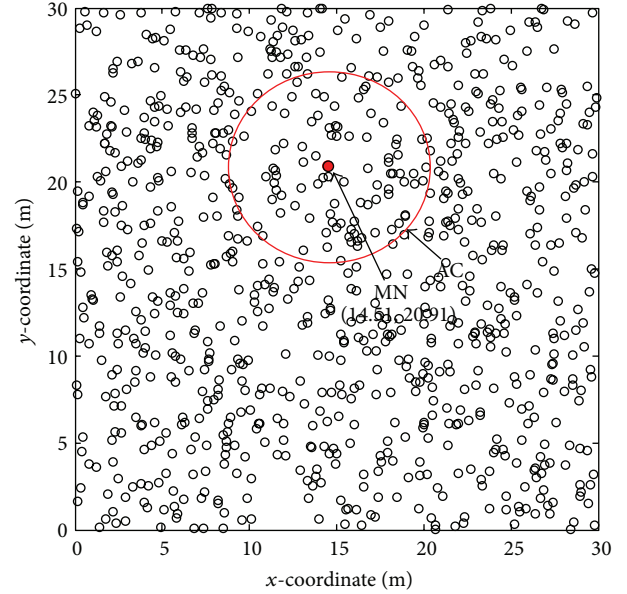


FIGURE 3: Randomly deployed Z nodes with selected MN and AC.

Step 6. Change radius of both r^{UCA} for UCA and r^{CCB} for CCB, with both depending on the desired size of beamwidth.

Step 6(a). Return to Step 1 for different virtual circles.

Step 6(b). Compare the radiation beampattern performance results for different r values.

Step 7. Select the best solution.

The final solution from the proposed CCB is to select the active nodes to perform CB. The intelligent feature in this proposed algorithm is how the algorithm managed to select the best team of active nodes to accomplish CB with user desired requirements. Examples of such requirements are the desired radiation beampattern with minimum SLL and expected size of FNBW. Results are then validated with UCA [12] and circular sensor node array (CSA) as evidence of the effectiveness. Active nodes of CSA are selected based on the UCA, which has the nearest location to nodes of UCA. In CSA optimization setup phase, Step 2 of establishing HLPSON is not included because the distance between nodes d_{sn} of CSA are directly from the distance between nodes of UCA.

4. Results and Analysis

The computed optimization results in radiation beampatterns are analyzed in different cases of N -node CCB with different objectives. The validation performances are demonstrated between CCB and corresponding results obtained from the CSA and conventional UCA [12].

Figure 3 illustrates the simulation scenario for 8-node CCB in MATLAB environment. It shows the random deployment of Z nodes inside the area of interest, that is, Λ , with selected MN. Initially, Z nodes are in a sleep mode. The red

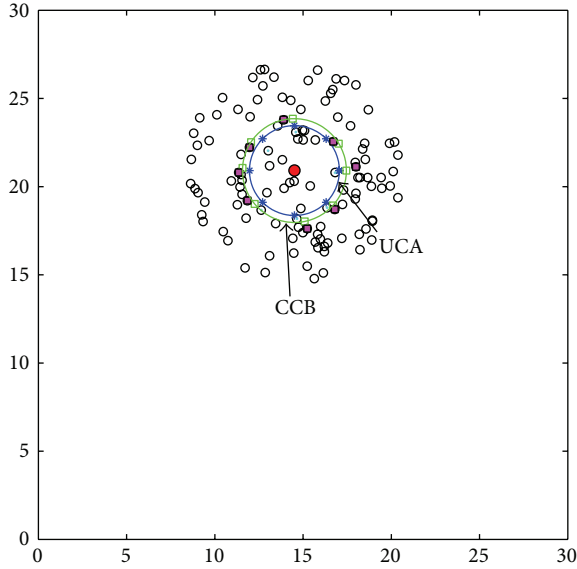


FIGURE 4: Virtual circles (a) blue depicts UCA and (b) green depicts CCB, and nodes (c) blue stars depict A_n , (d) green squares depict B_n , (e) blue circles depict R_n , and (f) square magentas depict M_n .

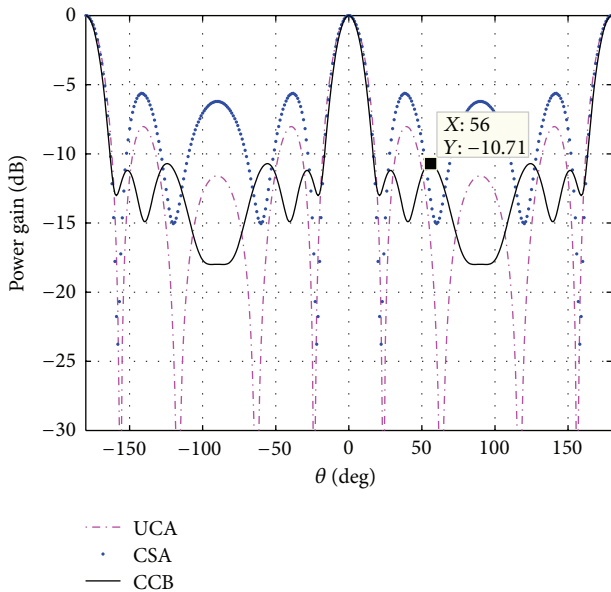


FIGURE 5: Radiation beampattern of 8-node CCB with SLL minimization.

circle marks the AC area, that is, X , with MN at the center of the AC. Figure 4 only highlights the nodes inside the AC. These Z_S nodes are in an idle mode, waiting for any instructions from MN or the center controller. Green circle is a virtual circle with r^{CCB} . Green squares denote coordinates for HLPSo-based nodes, $B_n(x_n^B, y_n^B)$, while square magentas denote CCB active nodes, $M_n(x_n^M, y_n^M)$. The CSA active nodes, R_n , are represented by light blue circles.

Table 3 lists the x - and y -coordinates for B_n and M_n for $n = 1, 2, \dots, 8$ nodes. The Euclidean distance errors

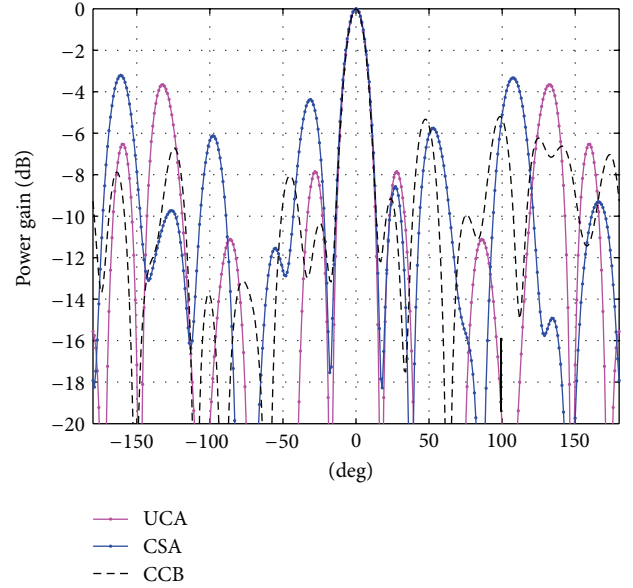


FIGURE 6: Radiation beampattern of 8-node CCB with SLL minimization.

ϵ_n between HLPSo-based nodes B_n and the proposed CCB active nodes M_n are also demonstrated in the same table. The sum average for all distances for 8-node CCB is calculated as 0.4021.

4.1. Sidelobe Level (SLL) Suppression. In the proposed CCB, SLL can be successfully suppressed to increase the received power at the receivers and to avoid interference from other interrupting access points or clusters or prevent these access points or clusters from recovering the transmitted signal. Figure 5 demonstrates the computed normalized gain for 8-node CCB at x - z plane ($\phi = 0^\circ$). It is observed that, for 360° radiation beampattern, the main beam gain exists at two different angles, that is, 0° and 180° . The maximum SLL obtained is low which is only -10.71 dB, while the maximum SLLs of UCA and CSA are approximately -8.03 dB and -5.63 dB, respectively.

The optimization then considers a circular array with FNBW of 38° with the main beam angle pointing towards $\theta_0 = 0^\circ$. Figure 6 shows the computed radiation beampatterns for y - z plane ($\phi = 90^\circ$), magenta curve for UCA with fixed spacing of $\lambda/2$ between elements, and blue curve for CSA, whereas black curve was proposed for CCB by using HLPSo. It can be clearly observed that the SLL suppression of CCB is generally better than that obtained from both UCA and CSA. All the minor lobes have been successfully minimized with the highest peak SLL to be approximately -5.20 dB compared to the maximum SLL of UCA and CSA of -3.66 dB and -3.21 dB, respectively. The two high lobes at -132° and 132° which exist in UCA have been greatly suppressed in this newly proposed CCB by considerable amount of 4 dB and 2 dB, respectively. At y - z plane, only one main beam exists in CCB for 360° radiation beampattern. These showed that the weakness of LSNA [8] which generates two main beams in 360° radiation beampattern is improved with CCB.

TABLE 3: Coordinates of B_n and M_n with difference Euclidean distances, ε_n .

n	x_n^B	y_n^B	x_n^M	y_n^M	$\varepsilon_n = \sqrt{(x_n^M - x_n^B)^2 + (y_n^M - y_n^B)^2}$
1	17.0	22.4	16.7	22.6	0.3374
2	14.4	23.9	13.9	23.8	0.5204
3	12.0	22.5	12.0	22.2	0.3117
4	11.6	21.1	11.4	20.8	0.3362
5	12.3	19.0	11.9	19.2	0.4503
6	15.1	18.0	15.2	17.6	0.4337
7	16.7	18.9	16.8	18.7	0.2445
8	17.5	20.9	18.0	21.1	0.5828

$\sum_{n=1}^8 \varepsilon_n / 8 = 0.4021$

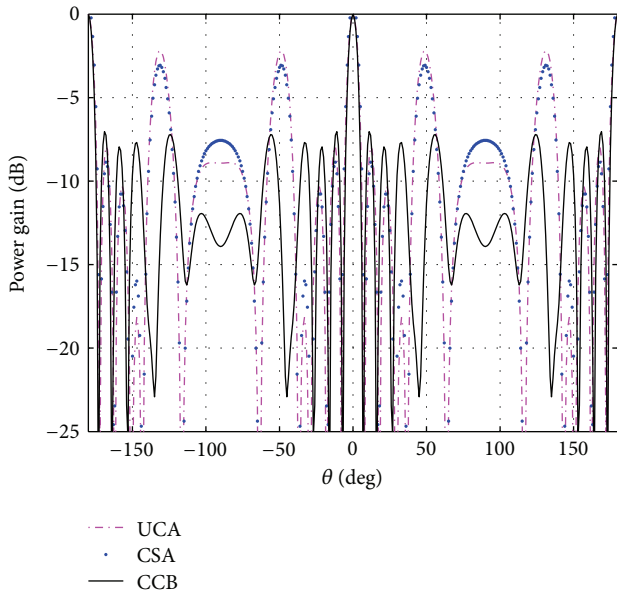


FIGURE 7: Radiation beampattern of 12-node CCB with SLL minimization.

The next case considers 12-node CCB. It demonstrates the different effects on the radiation beampattern performance with different arrangements of the node location. It can be seen from Figure 7 that the conventional UCA exhibits relatively high SLL at -131° , -49° , 49° , and 131° , which is similar to CSA. The maximum SLL of CCB shows degradation, that is, decrease of 5.02 dB, compared to the maximum SLL of UCA (i.e., -2.19 dB at 49°).

16-node CCB is then considered. It can be observed from Figure 8 that the highest peak SLL of approximately -4.32 dB exists at -109° , -71° , 71° , and 109° for both UCA and CSA. However, CCB managed to greatly minimize the SLL until -14.30 dB at the respective angles. As the number of CB active nodes increases, it not only can increase the gain but also narrows the FNBW as desired. In this case of 16-node ICSA, the FNBW is only 14° .

Three cases are analyzed with different numbers of CCB nodes as shown in Table 4. From the results, it is noted that this newly proposed CCB can overcome the undesired

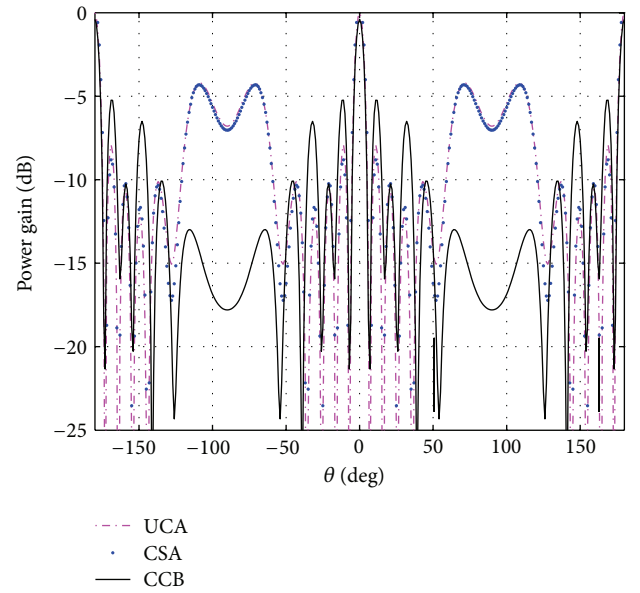


FIGURE 8: Radiation beampattern of 16-node CCB with SLL minimization.

increment of the SLLs in UCA and CSA by intelligently optimizing the participating CB active nodes.

4.2. Controllable First Null Beamwidth (FNBW). An advantage of CCB over UCA and CSA is that the CCB has the capability to adjust the desired amount of FNBW. It is essential to control FNBW in order to decrease the energy consumption. The size of FNBW is needed to be narrower for data transmission to focus the radiation to the attempted destination. In contrast, the size for FNBW is needed to be wider for direction-finding applications.

It reveals the different effects on the size of FNBW performance with the different arrangements of the node location. The radiation patterns of 8-node CCB are plotted in Figure 9. It illustrates a smaller radius of CCB with $r = 1.0312$, resulting in a wider FNBW of approximately 64° compared to Figure 10 with $r = 4.098$. It can be seen that the 8-node CCB intelligently accomplishes any desired size of FNBW, either wider or narrower, by optimizing the active

TABLE 4: Percentage improvement of SLL performance for CCB in different cases.

Case	N	N-node CCB		N-node CSA		N-element UCA		Improvement (%)
		SLL (dB)	FNBW (°)	SLL (dB)	FNBW (°)	SLL (dB)	FNBW (°)	
1	8	-5.2	38	-3.21	38	-3.66	38	61.99
	8	-10.71	46	-5.63	46	-8.03	46	90.23
2	12	-7.04	16	-3.07	16	-2.19	16	129.32
3	16	-14.03	14	-4.32	14	-4.32	14	224.77

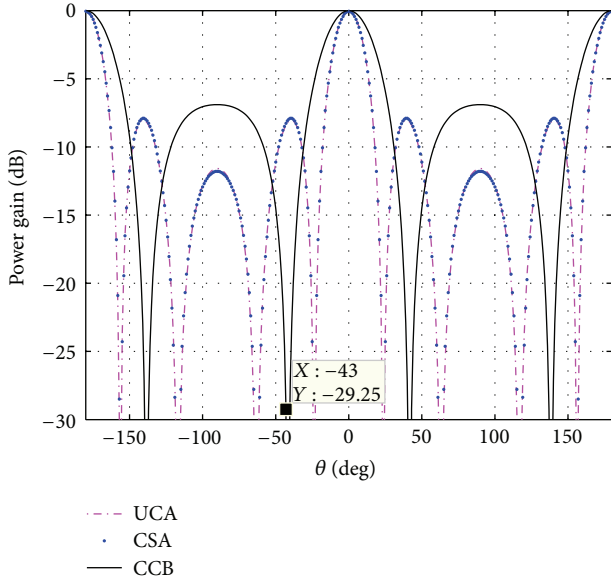


FIGURE 9: Radiation beampattern of 8-node CCB with wider FNBW.

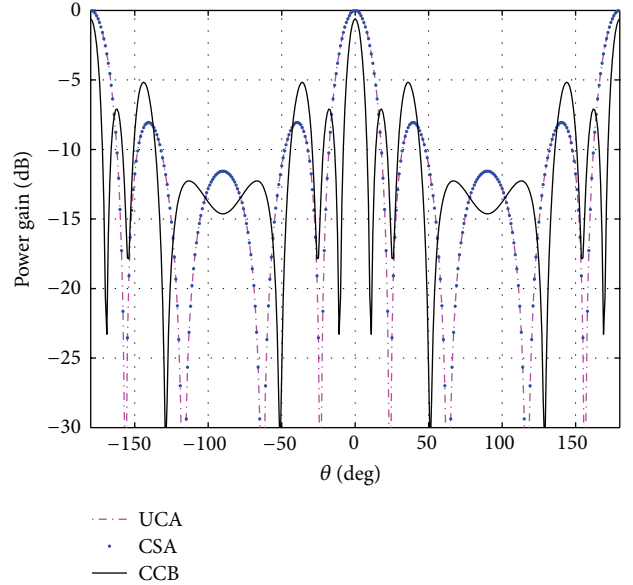


FIGURE 10: Radiation beampattern of 8-node CCB with narrow FNBW.

CB nodes selection. Both CSA and UCA exemplify a similar performance with $r = 1.9098$. The trade-off performance between SLL and FNBW is obviously illustrated. All the minor SLLs have increased throughout the elevation angles. The SLL increases with adaptive FNBW, both CCB and FNBW of 86° and 22° , generate a higher SLL compared to UCA and CSA.

Next case considers 12-node CCB with $r = 5.9761$ to optimize the size of FNBW. The radiation patterns are depicted in Figure 11. It is observed that the FNBW of the optimized 12-node CCB is wider (i.e., 44°) than that of 12-node CSA (i.e., 30°). Additionally, all the minor SLLs have decreased throughout the elevation angles at approximately only -11.51 dB. The subsequent array considered is also a 12-node CCB but with smaller radius of $r = 1.6932$. It shows a larger FNBW (i.e., 50°) as compared to CSA (i.e., 16°) as shown in Figure 12.

It can be observed that a good performance of radiation pattern is obtained from CCB as compared to the previous CSA. It is also shown that different radii contribute to different performances of CCB. In addition, it is noted that the 12-node CCB with FNBW of 50° maintains low SLL throughout the angles that is less than -7.483 dB. Therefore, it is proven that, by implementing the objective function together with CCB, the desired FNBW

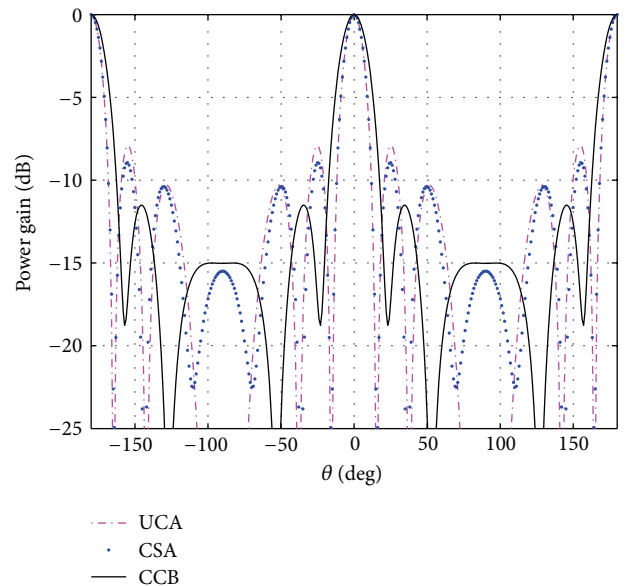


FIGURE 11: Radiation beampattern of 12-node CCB with narrow FNBW.

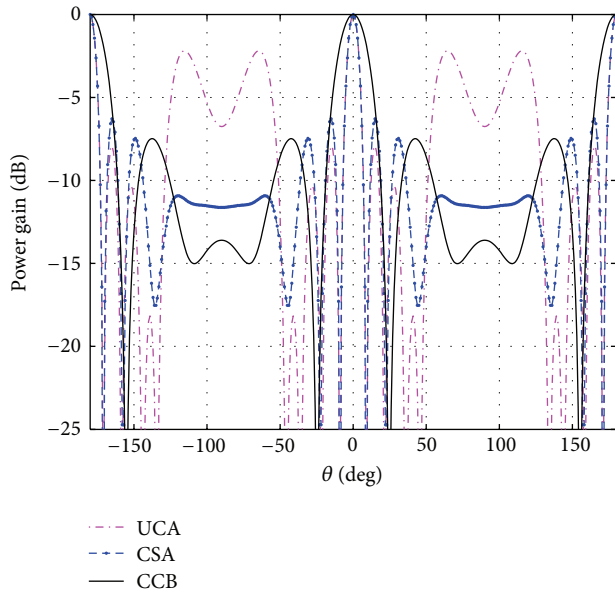


FIGURE 12: Radiation beampattern of 12-node CCB with wide FNBW.

can be controlled that simultaneously improved the SLL suppression.

5. Conclusion

The problem of array beamforming is the presence of error beampattern caused by random sensor position errors. The proposed CCB can effectively improve reliability, capacity, and coverage by intelligently adjusting the shape of the beam patterns under different constraints, either by suppressing the SLL or managing the size of FNBW as per desired usage. The proposed CCB has the ability to select the active CB nodes and dynamically control the radiation beampattern to enhance the reception while minimizing the interferences using the proposed HLPSON-based CCB algorithms. The radiation beampattern expression of the proposed CCB is obtained, and it is further proved. Different properties of the radiation beampattern have been successfully analyzed and proven.

Acknowledgments

The work is supported by Universiti Teknologi Malaysia and Ministry of Education Malaysia, RUG vote PY/2012/01578 and FRGS vote 4F039.

References

- [1] J. Feng, Y. Nimmagadda, Y. H. Lu, B. Jung, D. Peroulis, and Y. C. Hu, "Analysis of energy consumption on data sharing in beamforming for wireless sensor networks," in *Proceedings of the 19th International Conference on Computer Communications and Networks (ICCCN '10)*, pp. 1–6, August 2010.
- [2] K. Yao, R. E. Hudson, C. W. Reed, D. Chen, and F. Lorenzelli, "Blind beamforming on a randomly distributed sensor array system," *IEEE Journal on Selected Areas in Communications*, vol. 16, no. 8, pp. 1555–1566, 1998.
- [3] M. F. A. Ahmed and S. A. Vorobyov, "Beampattern random behavior in wireless sensor networks with Gaussian distributed sensor nodes," in *Proceedings of the IEEE Canadian Conference on Electrical and Computer Engineering (CCECE '08)*, pp. 257–260, May 2008.
- [4] Z. Han and H. V. Poor, "Lifetime improvement of wireless sensor networks by collaborative beamforming and cooperative transmission," in *Proceedings of the IEEE International Conference on Communications (ICC '07)*, pp. 3954–3958, June 2007.
- [5] M. F. A. Ahmed and S. A. Vorobyov, "Node selection for side-lobe control in collaborative beamforming for wireless sensor networks," in *Proceedings of the IEEE 10th Workshop on Signal Processing Advances in Wireless Communications (SPAWC '09)*, pp. 519–523, June 2009.
- [6] H. Ochiai, P. Mitran, H. V. Poor, and V. Tarokh, "Collaborative beamforming for distributed wireless ad hoc sensor networks," *IEEE Transactions on Signal Processing*, vol. 53, no. 11, pp. 4110–4124, 2005.
- [7] M. F. A. Ahmed and S. A. Vorobyov, "Sidelobe control in collaborative beamforming via node selection," *IEEE Transactions on Signal Processing*, vol. 58, no. 12, pp. 6168–6180, 2010.
- [8] N. N. N. A. Malik, M. Esa, S. K. S. Yusof, and S. A. Hamzah, "Optimization of adaptive linear sensor node array in wireless sensor network," in *Proceedings of the Asia-Pacific Microwave Conference (APMC '10)*, pp. 2336–2339, Singapore, December 2009.
- [9] N. N. N. A. Malik, M. Esa, S. K. S. Yusof, and S. A. Hamzah, "Optimization of linear sensor node array for wireless sensor networks using Particle Swarm Optimization," in *Proceedings of the Asia-Pacific Microwave Conference (APMC '10)*, pp. 1316–1319, December 2010.
- [10] P. Vincent, M. Tummala, and J. McEachen, "A new method for distributing power usage across a sensor network," *Ad Hoc Networks*, vol. 6, no. 8, pp. 1258–1280, 2008.
- [11] M. Batson, J. McEachen, and M. Tummala, "Enhanced collection methodology for distributed wireless antenna systems," in *Proceedings of the IEEE International Conference on System of Systems Engineering (SOSE '07)*, April 2007.
- [12] C. A. Balanis, *Antenna Theory: Analysis and Design*, Wiley, New York, NY, USA, 3rd edition, 2005.
- [13] J. Kennedy and R. Eberhart, "Particle swarm optimization," in *Proceedings of the 1995 IEEE International Conference on Neural Networks*, pp. 1942–1948, December 1995.
- [14] Z. Zaharis, D. Kampitaki, A. Papastergiou, A. Hatzigaidas, P. Lazaridis, and M. Spasos, "Optimal design of a linear antenna array using particle swarm optimization," in *Proceedings of the 5th WSEAS International Conference on Data Networks, Communications and Computers*, pp. 69–74, Bucharest, Romania, October 2006.

Research Article

On the Efficiency of Capacitively Loaded Frequency Reconfigurable Antennas

Samantha Caporal Del Barrio and Gert F. Pedersen

Section of Antennas, Propagation and Radio Networking (APNet), Department of Electronic Systems, Faculty of Engineering and Science, Aalborg University, 9220 Aalborg, Denmark

Correspondence should be addressed to Samantha Caporal Del Barrio; scdb@es.aau.dk

Received 27 February 2013; Accepted 10 June 2013

Academic Editor: Korkut Yegin

Copyright © 2013 S. Caporal Del Barrio and G. F. Pedersen. This is an open access article distributed under the Creative Commons Attribution License, which permits unrestricted use, distribution, and reproduction in any medium, provided the original work is properly cited.

The design of a reconfigurable antenna that can be fine tuned to address future communication systems is proposed. The design consists of a capacitively loaded patch antenna for nowadays smartphone platforms. The antenna is narrowband and can be fine tuned over the range (700 MHz–960 MHz). Measurements at 700 MHz with fixed capacitors raise the challenge of the component insertion loss. Distribution of the tuning capacitance is investigated and shows 1 dB improvement in the antenna radiation efficiency.

1. Introduction

The need for bandwidth has been dramatically increased with the standardization of the 4th Generation (4G) of mobile communication systems. Handset devices need to cover an ever-increasing frequency spectrum. Today's specifications fill the spectrum from 700 MHz to 2.6 GHz [1]. The trend shows that further widening of the spectrum towards 600 MHz is likely. Therefore, the need for frequency coverage is urgent and essential to future communication systems. However, electrically small antennas respond to fundamental laws that limit their possibility to increase their bandwidth while simultaneously preserve a small size and a good radiation efficiency. The trade-off between antenna radiation efficiency, size and bandwidth is detailed in [2]. The antenna bandwidth issue is mostly challenging at the low frequencies (below 1 GHz) as the radiating structure is the whole handset, which becomes electrically smaller.

In order to cover the required bandwidth, Frequency Reconfigurable Antennas (FRA) are a promising solution. An FRA is a small and efficient antenna that covers only one band at a time. This element is made reconfigurable in order to choose which band to operate in. In that way, FRA can cover an effectively wide bandwidth—while covering instantaneous narrow bandwidths—and preserve its small

size. Further, one can see that the complexity of the RF chain increases with the number of bands to cover, and an optimal solution is having an antenna pair (separate and flexible transmitting and receiving chains). In that case, one FRA only needs to cover a channel, which decreases even further its bandwidth requirement, highlighting FRA potential for 4G communication systems.

The reconfigurability mechanism can be implemented with various techniques such as switches, p-i-n or varactor diodes [3], or MicroElectroMechanical Systems (MEMS) capacitors. MEMS components are regarded as the best candidates for FRA application as they exhibit a high Quality factor (Q) and excellent linearity. They add little insertion loss in Radio Frequency (RF). For example, RF MEMS tunable capacitors have been successfully implemented in tunable filters, as described in [4–6]. Their implementation on mobile phone antenna designs has been investigated in [7] and in [8] for the UHF band (510 MHz–800 MHz) and in [9] for the PCS and IMT bands. RF MEMS appeared for the first time on the phone market with the release of Samsung Omnia [10].

The first study on the antenna pair front-end design [11] shows the importance of the Q of the tuning capacitor as it severely affects the FRA radiation efficiency. Further studies on FRA confirm that the limiting criteria to achieve highly efficient systems are the tunable component. In [8], MEMS

variable capacitors are used to tune a low-profile antenna in the Digital Terrestrial Broadcasting (DTB) band. The efficiency decreases from -1 dB to -4 dB between 800 MHz and 500 MHz. This study is relevant as the investigated frequencies can be foreseen as the next ones and most challenging ones to be covered with 4G.

The losses in FRA are mainly coming from the tuner and need to be overcome even though better components are not yet available. This paper investigates the loss mechanism of the FRA at the low-band and proposes a distributed tuning mechanism in order to reduce the loss due to the tuner. The paper will be organized in 5 sections. Section 2 presents the problem of high-loss for fine-tuned narrowband antennas. Section 3 details the distributed-tuning design, and Section 4 concludes on the improvements such design brings on the antenna performance. Finally, Section 5 describes the future implementation of the presented findings.

2. Problem Formulation

The FRA must have the ability to be fine-tuned over the bands to cover. This study focuses on the low-band for 4G from 960 MHz to 700 MHz. As detailed in [12], in order to achieve fine-tuning, the capacitance steps of the tuner will determine the position of the tuner on the antenna structure. The total tuning range will then be determined by the maximum capacitance the tuner can provide. Moreover, the position of the tuner will determine the loss it will cause on the total antenna system. It is important to understand that the optimal position of the tuner—that is determined by its capacitance steps—is not the optimal position from an efficiency point of view [13]. The closer to the antenna feed point, the higher the currents delivered to the tuner and the greater the loss. Indeed, the tuner has resistive losses; they are modeled with the Equivalent Series Resistance (ESR) and are proportional to the square of the current delivered to it. As a result, the measured loss becomes greater as the antenna is tuned further away from its original resonance frequency. This loss issue is a specific problem of fine-tuned narrowband antennas and it has been documented in [8, 12, 14–17] with different tuning components. Additionally, the work in [18] uses high-Q discrete components instead of a packaged tuner and shows that the same phenomenon happens. The total loss drops from -2.2 dB to -3.6 dB between 960 MHz and 800 MHz. As documented in the literature, the greatest loss happens at the furthest frequency the antenna is tuned to, compared to its natural resonance frequency. Therefore, the investigation presented in this paper will focus on the lowest frequency of the tuning range, here 700 MHz. This section will present two antenna mock-ups and measure their efficiency. The first mock-up includes a discrete high-Q capacitor and the second mock-up includes a built-in air capacitor. This study will quantify the loss due to the fixed capacitor. The next section will propose a distributed tuning system in order to reduce that loss.

2.1. Antenna Design. The presented antenna design aims at being assembled with an MEMS tunable capacitor to become an FRA. For that reason the design is made to originally

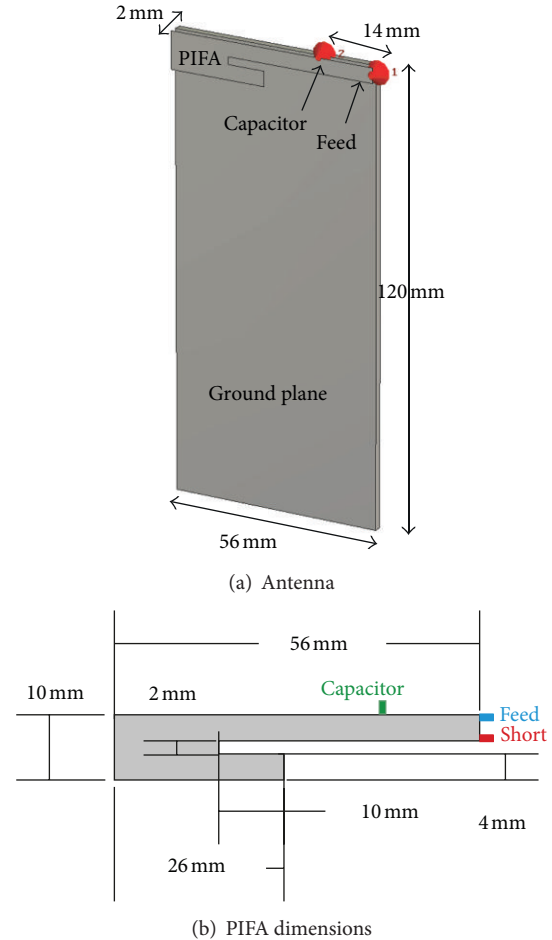


FIGURE 1: Antenna design.

resonate at 960 MHz. Simulations were performed with the transient solver of CST MWS, a Finite-Element-Method (FEM-) based solver [19]. The chosen design is a Planar-Inverted-F Antenna (PIFA) as it is a low-cost and easy to manufacture antenna. The dimensions of the PIFA are shown in Figure 1. The ground plane of the structure has dimensions 120×55 mm in order to represent nowadays smartphones. The PIFA is placed 2 mm above the ground plane. The port 1 represents the feeding point of the antenna and the port 2 represents the tuning capacitor. Port 1 and Port 2 are spaced by 14 mm. The short of the PIFA is placed 2 mm below the feeding point. Simulations can determine the position of the tuner in order to achieve fine tuning with capacitance steps of $1/8$ pF—as provided by the tuner in [20]. Key information in the design of an FRA is that the capacitance steps of the tuner will determine the position of the tuner on the antenna structure in order to achieve fine-tuning. To continuously tune the resonance frequency of the proposed antenna to 700 MHz, a total capacitance of 5.1 pF is needed, at the position 14 mm away from the source. Simulations of the tunability of the antenna design are shown in Figure 2. In lossless simulations the matching of the antenna varies as more capacitance is added to the structure. In measurements,

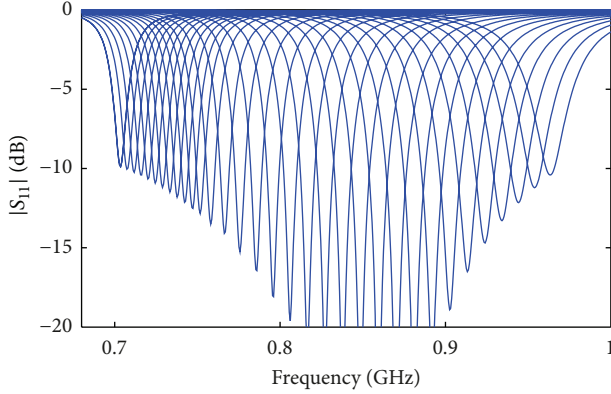


FIGURE 2: Simulated FRA frequency response.

TABLE 1: ESR and Q_c of the discrete capacitor at 700 MHz.

C [pF]	ESR [Ω]	Q_c
5.1	0.258	173

the tuning loss helps preserving the matching [12]. This phenomenon will also be shown in the next subsection.

2.2. Discrete-Capacitor-Based FRA. The design previously described is built with a discrete capacitor for resonating at 700 MHz and it is shown in Figure 3. The mock-up is made out of pure copper and minimum tin is used in order to isolate the loss due to the ESR of the capacitor only. The high- Q Murata [21] fixed capacitor is inserted between the PIFA and the GP. The ESR and Q of the capacitor (Q_c) are summarized in Table 1. Q_c is calculated according to (1) where ω is the angular frequency and C is the capacitance:

$$Q_c = \frac{1}{\omega \times C \times \text{ESR}}. \quad (1)$$

Frequency responses of the mock-up are measured with and without fixed capacitor. Figure 4 shows that the matching is preserved throughout tuning. Additionally, the bandwidth (at -6 dB) is reduced from 25 MHz to 10 MHz. This is a result of the Antenna Q (Q_A) that dramatically increases as the resonance frequency is tuned further away from its natural one, as explained in [22]. The measured Q_A is depicted in Figure 5 and shows an increase from $Q_A = 25$ without tuning capacitor to $Q_A = 90$ with tuning component. The mock-up is further measured in anechoic chamber and its peak efficiency at resonance is computed with 3D pattern integration technique. The measured radiation efficiency (η_r) is -3.4 dB. η_r reflects only the thermal loss and the ESR loss. Mismatch and cable losses have been taken out hereafter.

2.3. Air-Capacitor-Based FRA. Narrowband antennas have a loss mechanism that is more complex than only the loss due to the ESR of the tuning capacitor, as shown in [12]. In order to isolate the thermal loss due to the narrowband antenna design itself, the previous mock-up is rebuilt with an integrated air capacitor made out of the same copper piece as the rest of

the antennas. The efficiency measurement will show the loss exclusively due to the copper. Figure 6 shows the pure copper mock-up. The two relatively small metal plates forming the air capacitor have the dimensions 20×10 mm. The size of the built-in air capacitor is calculated with (2) where ϵ is the permittivity, A is the area, and d is the distance separating the two plates. The capacitor is supported with additional polystyrene in order to have a stable distance d . Expanded polystyrene foam is commonly used in antenna mock-ups because its effect on measured antenna properties is known to be very low. The relative permittivity of the material used in the following is about 1.03 [23, 24]:

$$C = \frac{\epsilon A}{d}. \quad (2)$$

The air capacitor adds radiation surface to the mock-up and raises the question of comparability between the air-capacitor and the fixed capacitor mock-ups. In order to verify whether the air-capacitor alters the radiation characteristics of the antenna, the envelope correlation (ρ) is computed, as defined in [25]. It compares the measured pattern of the mock-up with the fixed capacitor and the measured pattern of the mock-up with the built-in air-capacitor. The anechoic chamber measurement is performed with angular steps of 15 degrees and $\rho = 0.988$. It is concluded that both mock-ups are comparable. The air capacitor acts as the discrete component-storing energy-and not as a radiator. Additionally, it is located at the top of the mock-up, where the fields are minimum according to dipole radiation mode. The measured radiation efficiency of the air-capacitor-based mock-up is $\eta_r = -0.8$ dB.

2.4. Mock-Up Resonating at 700 MHz. In order to confirm the existence of high thermal loss for pure-copper-narrowband antennas, a third mock-up resonating at 700 MHz is built. The modification made to the design shown in Figure 1 is lengthening the bottom arm of the PIFA from 26 mm to 56 mm. The new antenna exhibits similar complex antenna impedance and the radiation efficiency measurement shows $\eta_r = -0.8$ dB.

2.5. Interpretation of the Results. Antenna thermal loss due to the copper conductivity exists and plays a nonnegligible role in narrowband antenna designs. It cannot be easily simulated as shown in [26]. However, it can be isolated and measured. Once this loss is taken out of the FRA radiation efficiency, the loss due to the fixed component only can be evaluated. Comparing the discrete component measurement and the air capacitor measurement leads to the conclusion that the loss due to the ESR of the tuning capacitor is equal to -2.6 dB ($-3.4 - (-0.8)$). This result matches simulated loss due to the ESR. Indeed, the currents delivered to the tuning capacitor (I_C) can be computed in the simulator, and according to (3) it can be calculated that the dissipated Power due to the ESR (P_L) equals -2.3 dB. The estimated loss matches well the measurement as the difference between them is within the chamber accuracy:

$$P_L = \frac{I_C^2 \times \text{ESR}}{2}. \quad (3)$$

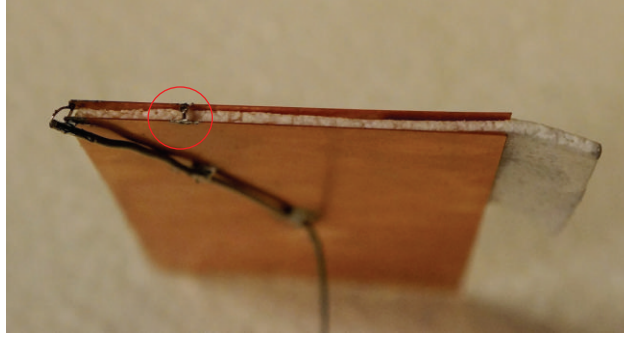


FIGURE 3: FRA mock-up with discrete capacitor.

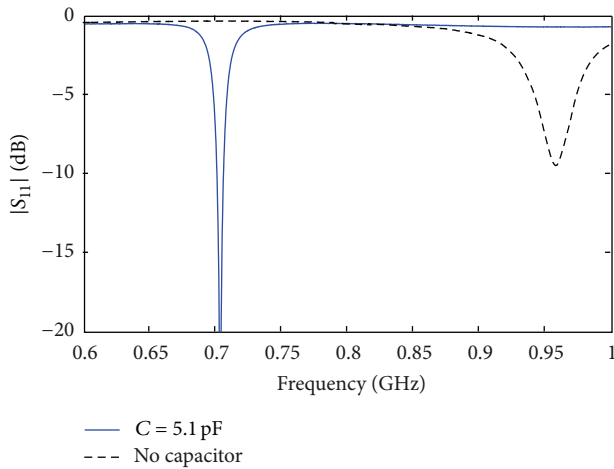
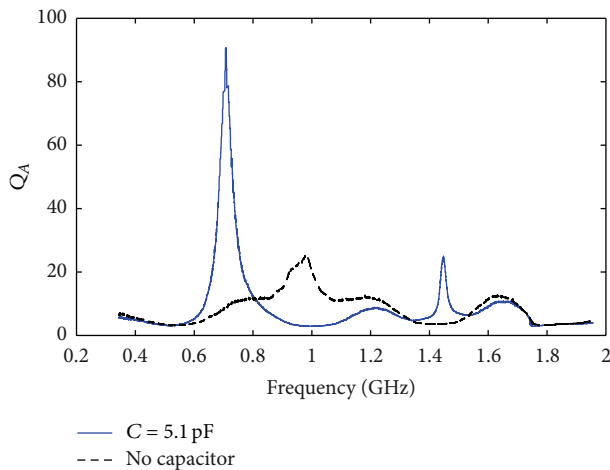


FIGURE 4: Measured FRA frequency response.

FIGURE 5: Measured Q_A of FRA with and without discrete capacitor.

The following section of this paper addresses the possibility of reducing P_L with a distributed capacitance design.

3. Distributed Tuning

It is well understood that by distributing the tuning mechanism along the antenna plate the current delivered to each

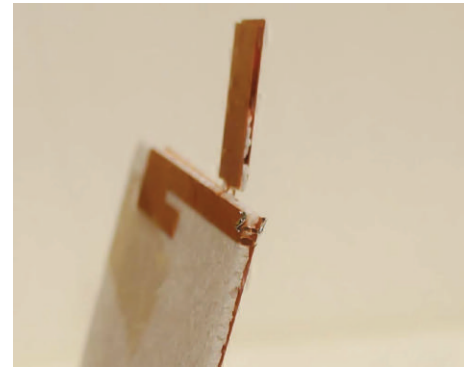


FIGURE 6: FRA mock-up with air capacitor.

capacitor would be reduced, and so the loss. However, how the distribution should be designed is not an obvious choice. This section presents how to place the tuners and investigates the loss reduction with simulations and measurements.

3.1. Design. Two tuning capacitors are used instead of one. They are both placed between the antenna element plate and the GP plate. Their location is chosen according to the capacitance steps the tuners can provide. According to the previous sections, a capacitor providing steps of $1/8$ pF needs to be placed 14 mm away from the source on the investigated PIFA design in order to achieve fine-tuning over the targeted bands. With a distributed design, one of the capacitors also needs to be placed at 14 mm in order to ensure fine-tuning, given that it provides steps of $1/8$ pF as well. The other capacitor can be placed further away from the source. The additional capacitor will then tune with larger frequency shifts. In that way, the first tuner C_1 (placed the closest from the source) will use smaller amounts of capacitance compared to a single tuner design. This will result in less loss due to its ESR. The second tuner C_2 (placed the furthest from the source) will also exhibit low loss, as it is placed far from the high-current concentration.

Figure 7 illustrates the distributed-tuning design that is implemented on the investigated PIFA design. The results obtained with the distributed capacitance design shown in Figure 7(a) will be compared to the case where only one tuning capacitor is used at 14 mm from the source

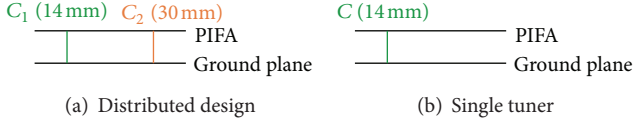


FIGURE 7: Tuning designs.

TABLE 2: Capacitance and ESR for distributed tuning.

	$C_{1\text{pos}} = 14$ pF/ Ω	$C_{2\text{pos}} = 30$ pF/ Ω
900 MHz	0.250/0.863	0.250/0.863
850 MHz	0.375/1.120	0.625/0.282
800 MHz	1.000/0.325	0.875/0.298
750 MHz	1.500/0.230	1.250/0.282
700 MHz	2.000/0.197	1.750/0.244

TABLE 3: Capacitance and ESR for single-capacitor tuning.

	$C_{\text{pos}} = 14$ mm pF/ Ω
900 MHz	1.000/0.336
850 MHz	2.000/0.212
800 MHz	3.000/0.234
750 MHz	4.000/0.243
700 MHz	5.125/0.257

($C_{\text{pos}} = 14$ mm) as shown in Figure 7(b). This comparison will lead to a fair evaluation of the improvement a distributed-tuning mechanism brings to an FRA. From a reflection coefficient point of view, performances are unchanged with a distributed system compared to a single-capacitor tuning system.

3.2. Simulations. The investigation on the distributed capacitance is first conducted with simulations. The ESR of the simulated capacitors is taken according to the bank of Murata 0402 capacitors from the GRM 15 collection [21], values for the MEMS [20] not being available. All the simulations are normalized to 1 W input power.

3.2.1. Capacitance. Tables 2 and 3 summarize the capacitance and ESR data that will be used throughout the simulations, in order to tune the investigated PIFA design from 960 MHz to 700 MHz. For more clarity, the simulated results are only displayed every 50 MHz. Tables 2 and 3 also show that by using the distributed design, the amount of capacitance that is needed per capacitor is considerably smaller than that with using only one tuning capacitor. Indeed, if only one capacitor was used for tuning at the position $C_{\text{pos}} = 14$ mm, the amount of required capacitance at this location would be at least twice larger than that with the proposed distributed design.

3.2.2. Normalized Currents. The surface currents in the case of single-capacitor tuning and of distributed tuning are shown in Figure 8 for 700 MHz. In the case of the distributed

tuning, the currents are spread on a larger section. Figure 9 depicts the magnitude of the peak current at each capacitor. It compares the distributed system to the single-capacitor tuning system. At 700 MHz in the case of the distributed tuning, the currents delivered to C_1 are reduced by 65% compared to the case of the single-capacitor tuning. The additional capacitor C_2 receives currents that are 50% reduced compared to the single-capacitor case. This significant current reduction will lead to a significant loss reduction.

3.2.3. Dissipated Power in the ESR. The amount each capacitor needs to provide to tune the antenna to a certain frequency is minimized with the use of a distributed-tuning system. Consequently, the energy stored in each capacitor is considerably reduced by using a distributed system. This result is plotted in Figure 10. Hence, the dissipated power in the ESR of each capacitor is also reduced using a distributed system, as depicted in Figure 11. At 700 MHz, the power dissipated by the capacitor placed at 14 mm is divided by a factor 4 for the distributed tuning compared to the single-capacitor tuning mechanism. The simulated η_r can be computed with the ESR values from Tables 2 and 3 and the simulated conductive loss. The conductive loss is a difficult task to model, requiring an extremely fine mesh in the transient simulator [26]. It is often under-estimated. The Figure 12 plots the simulation results of η_r over frequency. For the single-capacitor tuning system, an improvement of 1.5 dB happens due to the ESR loss alone, simulated radiation loss being identical for both mock-ups.

3.3. Interpretation of the Results. Distributed tuning has been compared to single-capacitor tuning with simulations. Given a capacitance step of the tuner, there is only one position (measured in distance to the antenna feed point) that will provide fine tuning. The same position must be taken by one of the capacitors used for distributed tuning. The second capacitor can be placed further away from the feed, at an arbitrarily chosen position. The main advantage that distributing the tuning provides to FRA is that the loss reduction increases as the antenna is tuned further away from its natural resonance (here 960 MHz). The further the antenna is tuned, the more relevant the distribution is. At 700 MHz, the dissipated power by the ESR is already reduced by a factor 4, and the radiation efficiency is enhanced by 1.5 dB using distributed tuning. With a trend towards extending the frequency spectrum to even lower frequencies, distributing the tuning will bring significant efficiency improvements. Using more than two capacitors to even further distribute the tuning could be considered. Nevertheless, one must keep in mind that the ESR increases as the capacitance decreases. Therefore, it is a trade-off between the reduction of the current density by distributing the tuning and the increase of the ESR by using smaller amounts of capacitance. Further investigations on the proposed design have shown that distribution with two capacitors is the optimal design.

3.4. Measurement. The mock-up shown in Figure 3 is modified for the distributed-tuning measurement. Instead of one capacitor of 5.1 pF placed at 14 mm from the feed, two

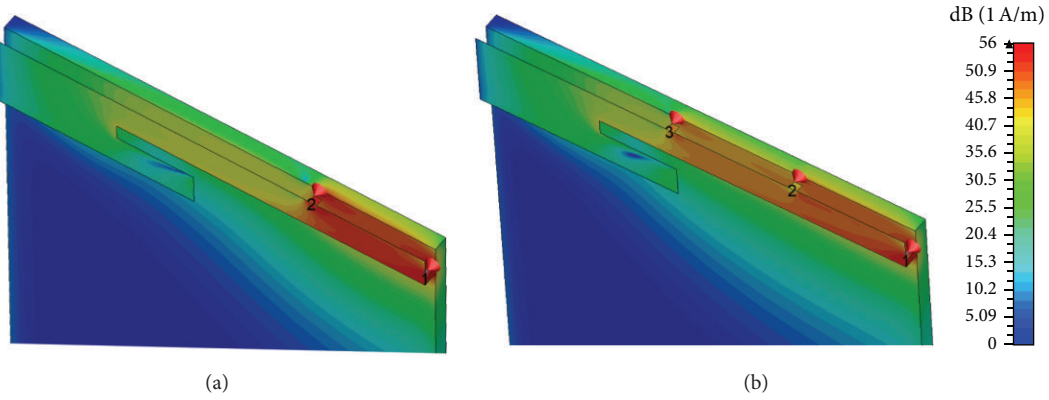


FIGURE 8: Surface currents in a single-capacitor tuning system (a) and a distributed system (b). Port 1 is the feed, port 2 and port 3 represent the capacitors.

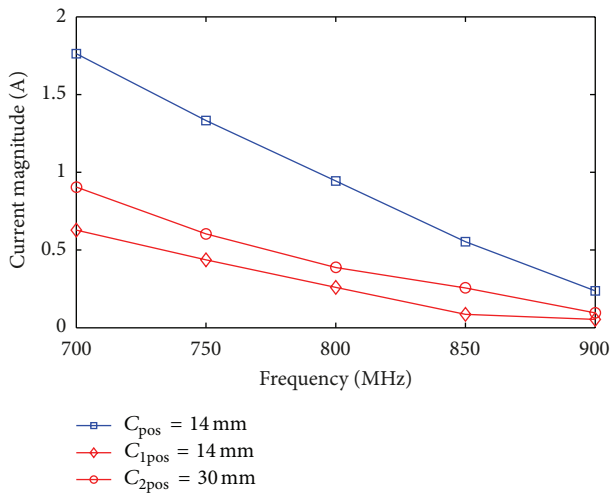


FIGURE 9: Normalized currents in a single-capacitor tuning system and a distributed system.

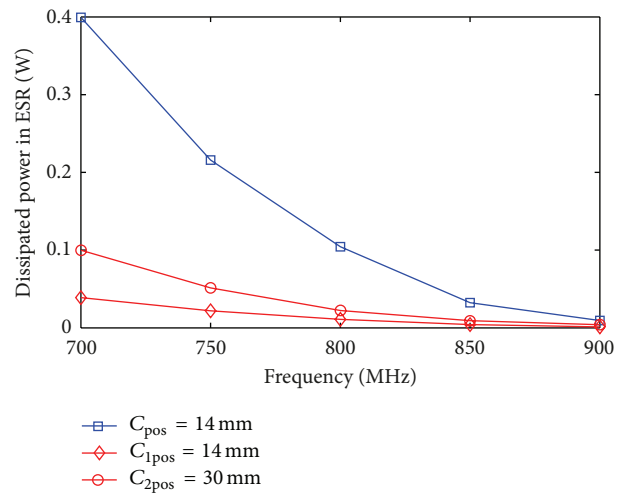


FIGURE 11: Dissipated power per capacitor in a single-capacitor tuning system and a distributed system.

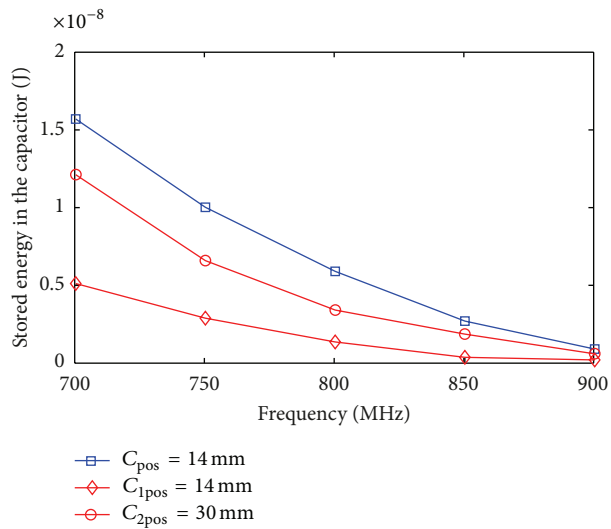


FIGURE 10: Energy stored in each capacitor in a single-capacitor tuning system and a distributed system.

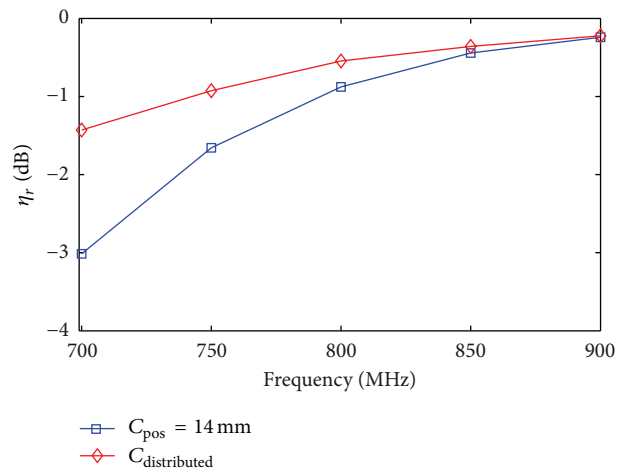


FIGURE 12: Simulated radiation efficiency in a single-capacitor tuning system and a distributed system.



FIGURE 13: FRA mock-up with distributed tuning system.

capacitors are used as shown in Figure 13. According to the Table 2, the capacitor placed at 14 mm takes the value 2.0 pF and the capacitor placed at 30 mm takes the value 1.7 pF. The frequency response of the mock-up is comparable to the one of the single-capacitor mock-up in terms of resonance frequency and bandwidth. The unloaded Q_A is not affected by having one or two capacitors on the mock-up. However, the measured loaded Q_A is increased by 20%, due to ESR adding in parallel. This increase corresponds to a bandwidth reduction of less than 1 MHz; therefore, it is considered negligible. The mock-up is further measured in anechoic chamber and the radiation efficiency equals $\eta_r = -2.1$ dB. With only one capacitor, the measured radiation efficiency is $\eta_r = -3.4$ dB. This measurement shows an improvement of 1.3 dB on the antenna efficiency when two capacitors are used instead of one. This result is consistent with the simulated improvement.

4. Conclusion

This work has highlighted the issue of tuning loss for narrowband FRA. This type of antennas can provide continuous tuning over a large frequency range. They have a great potential for 4G communications as only one small element can cover all frequencies in the low band (700 MHz to 960 MHz), by being tuned to the desired band (or channel if one considers an antenna pair). However, the tuning component cannot be placed in the best location from an efficiency point of view. That is because the position of the tuner ensures the fine tuning. As the loss it causes on the antenna radiation efficiency is significant—due to high fields in narrowband antennas—it is crucial to understand and reduce its impact. This work is specific to fine-tuned narrowband antennas, as for a 2-stage frequency reconfigurability there is more flexibility in the choice of the tuner position. Tuning has been considered to be performed with an MEMS variable capacitor in simulations. For more practicality, measurements have been performed with high-Q fixed components.

The conclusion of this paper is twofold: firstly, it shows the existence of thermal losses for narrowband antennas; secondly the loss due to the ESR of the tuner is quantified and reduced using a distributed-tuning mechanism. The antenna thermal loss (due to conductivity of the copper plate) is nonnegligible for narrowband antennas. This phenomenon happens because narrowband antennas exhibit higher and more confined fields than typical antennas. Additionally, the

higher thermal loss needs to be measured, as its estimation using simulators cannot be achieved in reasonable computational time. This paper compares a built-in air capacitor to a fixed high-Q component in order to quantify the loss due to the ESR of the capacitor and the thermal loss. In this way, the measured loss due to the ESR matches the simulated one. The ESR loss was estimated to be 2.6 dB when the antenna was tuned from 960 MHz to 700 MHz. In order to reduce this loss, a distributed-tuning design is proposed. It uses two capacitors placed at two different locations on the antenna. At 700 MHz, the distributed tuning shows 1.3 dB improvement on the total loss compared to the single-tuning mechanism. The loss due to the tuner increases as the operating frequency is tuned towards lower values. Similarly, the loss reduction improves as the frequency is tuned further away from the natural resonance frequency of the design. The wider the tuning range is, the greater the improvement by distributing the tuning.

5. Future Work

Distributing the capacitance reduces the current in each tuner. The voltage will be increased and one needs to ensure that it remains below the breakdown voltage of the tuner. However, with MEMS technology the breakdown voltage and the maximum capacitance are a trade-off. As distributing the tuning involves lowering the maximum capacitance, simultaneously increasing the maximum handled voltage should not be an issue. Moreover, designing a distributed-tuning mechanism increases the degree of complexity of the antenna, as two tuners are needed instead of one. Therefore, the authors suggest to co-design the antenna and the tuner so that only one tuner with two parallel and independent tracks can be used, instead of two tuners. Cost and complexity reduction can then be achieved and an efficient FRA can be manufactured for 4G. In the future work, the authors will build an FRA with a specifically designed tuner in order to efficiently cover the low band of the 4G spectrum with a single and small antenna.

Acknowledgment

The work is supported by the Smart Antenna Front End (SAFE) Project within the Danish National Advanced Technology Foundation, High Technology Platform.

References

- [1] "Feasibility study for further advancements for E-UTRA (LTE-Advanced)—Specification 36. 912—Release 11," 3GPP Technical Report, 2012.
- [2] R. F. Harrington, "Effect of antenna size on gain, bandwidth, and efficiency," *Journal of Research of the National Bureau of Standards D*, vol. 64, no. 1, pp. 1–12, 1960.
- [3] S.-K. Oh, H.-S. Yoon, and S.-O. Park, "A PIFA-Type varactor-tunable slim antenna with a PIL patch feed for multiband applications," *IEEE Antennas and Wireless Propagation Letters*, vol. 6, pp. 103–105, 2007.
- [4] A. Abbaspour-Tamijani, L. Dussopt, and G. M. Rebeiz, "Miniature and tunable filters using MEMS capacitors," *IEEE Transactions on Microwave Theory and Techniques*, vol. 51, no. 7, pp. 1878–1885, 2003.
- [5] D. Peroulis, S. Pacheco, K. Sarabandi, and L. P. B. Katehi, "Tunable lumped components with applications to reconfigurable MEMS filters," in *Proceedings of the International Microwave Symposium Digest IEEE-MTT-S*, pp. 341–344, May 2001.
- [6] Y. Liu, A. Borgioli, A. S. Nagra, and R. A. York, "Distributed MEMS transmission lines for tunable filter applications," *International Journal of RF and Microwave Computer-Aided Engineering*, vol. 11, no. 5, pp. 254–260, 2001.
- [7] M. Nishigaki, T. Nagano, T. Miyazaki et al., "Piezoelectric MEMS variable capacitor for a UHF band tunable built- In antenna," in *Proceedings of the IEEE MTT-S International Microwave Symposium (IMS '07)*, pp. 2079–2082, June 2007.
- [8] Y. Tsutsumi, M. Nishio, S. Obayashi et al., "Low profile double resonance frequency tunable antenna using RF MEMS variable capacitor for digital terrestrial broadcasting reception," in *Proceedings of the IEEE Asian Solid-State Circuits Conference (ASSCC '09)*, pp. 125–128, November 2009.
- [9] J. R. De Luis, A. Morris, Q. Gu, and F. de Flaviis, "Tunable duplexing antenna system for wireless transceivers," *IEEE Transactions on Antennas and Propagation*, vol. 60, pp. 5484–5487, 2012.
- [10] "Teardown: Samsung Focus Flash," <http://evertiq.com/news/21198?utm%20source=feedburner&utm%20medium=feed%20&utm%20campaign=Feed%253A+EvertiqCom%252Ffall+28evertiq.com+%253A%253A%20+Latest+news%2529&utm%20content=Google+Reader>.
- [11] J. T. Aberle, S.-H. Oh, D. T. Auckland, and S. D. Rogers, "Reconfigurable Antennas for Portable Wireless Devices," *IEEE Antennas and Propagation Magazine*, vol. 45, no. 6, pp. 148–154, 2003.
- [12] S. Caporal, D. Barrio, M. Pelosi, G. F. Pedersen, and A. Morris, "Challenges for frequency-reconfigurable antennas in small terminals," in *Proceedings of the IEEE Vehicular Technology Conference (VTC Fall '12)*, pp. 1–5, 2012.
- [13] S. C. Del Barrio, M. Pelosi, O. Franek, and G. F. Pedersen, "On the currents magnitude of a tunable Planar-Inverted-F Antenna for lowband frequencies," in *Proceedings of the 6th European Conference on Antennas and Propagation (EUCAP '12)*, pp. 3173–3176, March 2012.
- [14] M. G. S. Hossain and T. Yamagajo, "Reconfigurable printed antenna for a wideband tuning," in *Proceedings of the 4th European Conference on Antennas and Propagation (EuCAP '10)*, vol. 1, pp. 1–4, April 2010.
- [15] A. Suyama and H. Arai, "Meander line antenna built in folder-type mobile," in *Proceedings of the International Symposium on Antennas and Propagation (ISAP '07)*, pp. 294–297, 2007.
- [16] V.-A. Nguyen, R.-A. Bhatti, and S.-O. Park, "A simple PIFA-based tunable internal antenna for personal communication handsets," *IEEE Antennas and Wireless Propagation Letters*, vol. 7, pp. 130–133, 2008.
- [17] N. Behdad and K. Sarabandi, "A varactor-tuned dual-band slot antenna," *IEEE Transactions on Antennas and Propagation*, vol. 54, no. 2, pp. 401–408, 2006.
- [18] S. C. D. Barrio, M. Pelosi, and G. F. Pedersen, "On the efficiency of frequency reconfigurable high-Q-antennas for 4G standards," *Electronics Letters*, vol. 48, no. 16, pp. 982–983, 2012.
- [19] Computer Simulation Technology (CST), "CST Microwave Studio," 2012, <http://www.cst.com>.
- [20] WiSpry, "Tunable Digital Capacitor Arrays (TDCA)".
- [21] Murata, "Chip Monolithic Ceramic Capacitors," 2012.
- [22] O. Kivekäs, J. Ollikainen, and P. Vainikainen, "Frequency-tunable internal antenna for mobile phones," in *Proceedings of the 12th International Symposium on Antennas (JINA)*, vol. 2, pp. 53–56, 2002.
- [23] M. A. Plonus, "Theoretical investigations of scattering from plastic foams," *IEEE Transactions on Antennas and Propagation*, vol. 13, no. 1, pp. 88–94, 1965.
- [24] E. F. Knott, "Dielectric constant of plastic foams," *IEEE Transactions on Antennas and Propagation*, vol. 41, no. 8, pp. 1167–1171, 1993.
- [25] J. Pierce and S. Stein, "Multiple diversity with nonindependent fading," *Proceedings of the IRE*, vol. 48, pp. 89–104, 1960.
- [26] S. Caporal Del Barrio and G. F. Pedersen, "High-Q antennas: simulator limitations," in *Proceedings of the European Conference on Antennas and Propagation (EuCAP '13)*, vol. 1, 2013.